
Electronic Thesis and Dissertation Repository

11-13-2015 12:00 AM

High Pressure Studies of Nanostructured TiO₂ and Li₄Ti₅O₁₂ Using Raman Spectroscopy and Synchrotron X-ray Radiation

Fengping Xiao
The University of Western Ontario

Supervisor
Dr. Yang Song
The University of Western Ontario

Graduate Program in Chemistry
A thesis submitted in partial fulfillment of the requirements for the degree in Master of Science
© Fengping Xiao 2015

Follow this and additional works at: <https://ir.lib.uwo.ca/etd>

 Part of the [Chemistry Commons](#)

Recommended Citation

Xiao, Fengping, "High Pressure Studies of Nanostructured TiO₂ and Li₄Ti₅O₁₂ Using Raman Spectroscopy and Synchrotron X-ray Radiation" (2015). *Electronic Thesis and Dissertation Repository*. 3356.

<https://ir.lib.uwo.ca/etd/3356>

This Dissertation/Thesis is brought to you for free and open access by Scholarship@Western. It has been accepted for inclusion in Electronic Thesis and Dissertation Repository by an authorized administrator of Scholarship@Western. For more information, please contact wlsadmin@uwo.ca.

**High Pressure Studies of Nanostructured TiO₂ and Li₄Ti₅O₁₂
Using Raman Spectroscopy and Synchrotron X-ray
Radiation**

(Thesis Format: Integrated-Article)

By

Fengping Xiao

Graduate Program in Chemistry

A thesis submitted in partial fulfillment
of the requirements for the degree of
Master of Science

The School of Graduate and Postdoctoral Studies

The University of Western Ontario

London, Ontario, Canada

© Fengping Xiao 2015

Abstract

Nanomaterials have been extensively studied due to their distinctive properties such as surface effect, small-size effect and quantum size effect. In recent year, investigations of the structural and phase transformations of nanomaterials under high pressure are receiving increasing attentions. In addition to composition and synthetic routes, pressure provides a clean way to adjust interatomic distance and hence affect the crystal structure and thus properties of the nanostructured materials. Two nanomaterials (i.e. TiO_2 and $\text{Li}_4\text{Ti}_5\text{O}_{12}$) with different morphologies are studied in this thesis.

In one study, the high-pressure behaviours of four hydrothermal synthesized 1D rutile TiO_2 nanomaterials (i.e. nanowires, nanorods, flower-like nanorods and nanotubes) were studied using Raman spectroscopy and synchrotron X-ray diffraction for the first time. A new morphology of flower-like nanorods was the first time obtained by this synthesis method. The phase transition sequence of these four 1D rutile TiO_2 nanomaterials is consistent with previous study. However, an interesting high-pressure behaviour was observed on nanowires that the reflection of rutile phase was observed in all patterns upon compression and decompression, suggesting a unique phase transition phenomenon unprecedented in TiO_2 nanomaterials. Comparative studies of these 1D rutile TiO_2 nanomaterials show strongly contrasting morphology-dependent compression behaviours: (1) Upon compression, nanotubes show the highest phase transition pressure of 20.8 GPa. (2) A higher compressibility along a -axis was observed compared to c -axis. (3) A relatively low bulk modulus of TiO_2 nanotubes (bulk modulus of 193 GPa) was found indicating that among these 1D rutile TiO_2 nanomaterials, nanotubes has the highest compressibility.

In another study, nanoflower-like spheres $\text{Li}_4\text{Ti}_5\text{O}_{12}$ (LTO-1) and nanoparticles $\text{Li}_4\text{Ti}_5\text{O}_{12}$ (LTO-2) synthesized by microwave-assisted hydrothermal methods were

investigated under high pressure for the first time by Raman spectroscopy and synchrotron X-ray diffraction. In this study, two LTO samples show three special high-pressure behaviours. Firstly, no phase transformations were observed up to 27.1 GPa for LTO-1 and 26.3 GPa for LTO-2, indicating high structural stability of these two nanomaterials. Moreover, LTO-2 (bulk modulus of 167 GPa) has a much higher bulk modulus than LTO-1 (bulk modulus of 123 GPa) which indicates a morphology-induced alteration of bulk modulus. Further more, based on previous study of lattice strain has a positive correlation with bulk modulus, we can infer that LTO-2 has a larger intrinsic lattice strain than that of LTO-1, consistent with the observation of the better performance of LTO-1 in LIB operations. This study indicates that multiple factors including the lattice strain and surface area must be considered together in the design of new nanostructured electrode materials in the future.

Keywords

High pressure, diamond anvil cell, synchrotron radiation, X-ray diffraction, Raman spectroscopy, phase transition, bulk modulus, nanomaterials, morphology, reversibility.

The Co-Authorship Statement

I hereby declare that this thesis is written by Fengping Xiao. Dr. Yang Song played a major role in the editing and revision of the materials presented in all chapters.

TiO₂ nanowires, nanorods, flower-like nanorods and nanotubes in Chapter 2 were synthesised by Fengping Xiao in Dr. Yang Song's laboratory. Li₄Ti₅O₁₂ nanoflower-like sphere and nanoparticles in Chapter 3 were provided by Dr. Andy Sun's group in the University of Western Ontario. Besides, Fengping Xiao is responsible for all data collection and analysis.

I am aware of the University of Western Ontario Policy on Authorship and I certify that I have properly acknowledged the contribution of other researchers to my thesis.

I certify that, with the above qualifications, this thesis, and the research to which it refers, is the product of my own work.

To my loving family

Acknowledgements

First of all, I would like to express my great gratitude to my supervisors Prof. Yang Song. I can not finish my study without his exceptional supervision, encouragement, and unconditional support. It is a great honor for me to have this opportunity to study and work under the guidance of such good supervisor.

Next, I would like to thank my group members: Dr. Yue Hu, Mr. Jiwen Guan, Mr. Pan Wang, Miss. San Jiang, and Mr. Nilesh Shinde. And I really appreciate my former group members, Dr. Zhaohui Dong, Dr. Haiyan Mao, Mr. Ankang Zhao and Mr. Liang Zhou. You have been providing great help to me since the start of my graduate study. And two years company makes them my life-time friends.

I also appreciate all the technical support by the following people: Dr. Robert Gordon from Advanced Photon Source; Mr. Todd Simpson from Nanofabrication Laboratory. Their support made my experiments running more smoothly.

I would like thank my good friends (Dr. Nazhen Liu, Dr. Yoshiko Yabe and Miss Marsi Valmont). It is you who drive my loneliness away and leave me a colorful and joyful Canadian life.

Finally, I would like to give my special thanks to my parents, and especially my elder sister (Dr. Fengyi Xiao). Thanks for your unconditional love, support and understanding in last two years.

Table of Contents

Abstract	ii
Acknowledgements	vi
Table of Contents	vii
List of Tables	xii
List of Figures	xii
List of Appendix Tables	xv
List of Appendix Figures	xv
List of Abbreviations	xvii
Chapter 1 Introduction	1
1.1 Nanomaterials	1
1.1.1 Nanostructured TiO ₂	1
1.1.1.1 Structures and properties	1
1.1.1.2 Applications	3
1.1.1.3 Synthesis of one dimensional TiO ₂ nanomaterials	6
1.1.2 Nanostructured Li ₄ Ti ₅ O ₁₂	7
1.1.2.1 Properties and applications	7
1.1.2.2 Synthesis of Li ₄ Ti ₅ O ₁₂ nanomaterials	8
1.2 High pressure materials science	9
1.2.1 High pressure phenomena	9
1.2.2 High-pressure apparatus	11
1.2.2.1 Diamond anvil cells	11
1.2.2.2 The ruby pressure gauge	12
1.2.2.3 Pressure transmitting medium	13
1.2.3 High-pressure study of nanomaterials	14
1.3 Structural characterization of nanomaterials at high pressures	15
1.3.1 Raman spectroscopy	15

1.3.2 Synchrotron X-ray diffraction.....	17
1.3.2.1 Principle of synchrotron radiation.....	17
1.3.2.2 Synchrotron X-ray diffraction at high pressure	20
1.3.2.3 Synchrotron X-ray diffraction facilities	21
1.3.3 Other characterization techniques	24
1.3.3.1 Scanning electron microscope (SEM).....	24
1.3.3.2 Powder X-ray diffraction.....	24
1.4 Scope of the thesis.....	24
1.5 References	25
Chapter 2 Pressure-induced Structural Transformations of 1D Nanostructured TiO₂ Studied by Raman Spectroscopy and Synchrotron X-ray Diffraction	31
2.1 Introduction	31
2.2 Experimental.....	33
2.2.1 Materials synthesis	33
2.2.2 Sample preparation	34
2.2.3 Characterization.....	34
2.3 Results and discussion.....	35
2.3.1 Morphology.....	35
2.3.1.1 Nanowires	35
2.3.1.2 Nanorods.....	36
2.3.1.3 Flower-like Nanorods.....	37
2.3.1.4 Nanotubes	39
2.3.2 XRD characterization	40
2.3.3 Raman results of 1D nanostructured TiO ₂ upon compression and decompression.....	42
2.3.3.1 Nanowires	42
2.3.3.2 Nanorods.....	44

2.3.3.3 Flower-like nanorods.....	45
2.3.3.4 Nanotubes	46
2.3.4 Synchrotron XRD results of 1D nanostructured TiO ₂ upon compression and decompression.....	48
2.3.4.1 Nanowires	48
2.3.4.2 Flower-like nanorods.....	52
2.3.4.3 Nanotubes	55
2.3.5 Discussion	58
2.4 Conclusions	63
2.5 References	65
Chapter 3 High-pressure Studies of Nanostructured Li₄Ti₅O₁₂ by Raman Spectroscopy and Synchrotron X-ray Diffraction	67
3.1 Introduction	67
3.2 Experimental.....	69
3.3 Results and discussion.....	71
3.3.1 Raman results of nanostructured Li ₄ Ti ₅ O ₁₂ upon compression and decompression.....	71
3.3.1.1 Nanoflower-like spheres Li ₄ Ti ₅ O ₁₂ (LTO-1)	71
3.3.1.2 Nanoparticles Li ₄ Ti ₅ O ₁₂ (LTO-2).....	73
3.3.2 Synchrotron XRD results of nanostructured Li ₄ TiO ₁₂ upon compression and decompression.....	76
3.3.2.1 Nanoflower-like spheres Li ₄ TiO ₁₂	76
3.3.2.2 Nanoparticles Li ₄ TiO ₁₂ (LTO-2).....	80
3.3.3 Discussion	83
3.4 Conclusions	87
3.5 References	88
Chapter 4 Summary and Future work.....	91
4.1 Summary.....	91

4.2 Future work.....	92
4.3 References	93
Appendix I Data analysis methods.....	94
A 1.1 FIT2D	94
A 1.2 Rietveld refinement method.....	95
Appendix II Selected Rietveld refinements for 1D rutile TiO ₂ nanomaterials	96
Appendix III Selected Rietveld refinements for nanoparticles Li ₄ Ti ₅ O ₁₂ (LTO-2) ...	107
Curriculum Vitae	108

List of Tables

Table 2-1 Summary of high-pressure studies of rutile TiO_2	64
Table 3-1 Observed Raman active modes of $\text{Li}_4\text{Ti}_5\text{O}_{12}$ nanostructures and their pressure dependence.....	76
Table 3-2 Unit cell parameters and volumes of nanostructured $\text{Li}_4\text{Ti}_5\text{O}_{12}$	81

List of Figures

Figure 1-1 Crystal structures of rutile phase and anatase phase TiO_2	2
Figure 1-2 Reaction schemes for semiconductor photocatalysts.....	5
Figure 1-3 TEM and SEM images of 1D TiO_2 prepared by hydrothermal method. (a) nanorods (b) nanowires.....	6
Figure 1-4 Crystal structure of $\text{Li}_4\text{Ti}_5\text{O}_{12}$	8
Figure 1-5 Examples of high-pressure phenomena.....	10
Figure 1-6 Photo and schematics of a symmetric diamond anvil cell.....	12
Figure 1-7 Three types of Raman scattering: Rayleigh Scattering, Stokes Raman Scattering and Anti-Stokes Raman Scattering.....	15
Figure 1-8 Photo of the customized in-house Raman Microspectroscopy System.....	17
Figure 1-9 Schematic layout of a synchrotron radiation facility.....	18
Figure 1-10 Opening angle and flux (vs. E_{photon}) of (a) bending magnets, (b) wigglers, and (c) undulators.....	19
Figure 1-11 Schematic diagram of angle dispersive XRD.....	21
Figure 1-12 Angle dispersive XRD set up at 16BM-D of APS.....	22
Figure 1-13 The Schematic layout and photo of μ -XRD setup at BL15U1 beamline.....	23
Figure 2-1 Crystal structures of baddeleyite phase and α - PbO_2 phase TiO_2	32
Figure 2-2 SEM images of rutile TiO_2 nanowires.....	36
Figure 2-3 SEM images of rutile TiO_2 nanorods.....	37
Figure 2-4 SEM images of rutile TiO_2 flower-like nanorods.....	38

Figure 2-5 SEM images of rutile TiO ₂ nanotubes.....	39
Figure 2-6 X-ray diffraction patterns from rutile TiO ₂ nanorods, nanowires, flower-like nanorods and nanotubes.....	41
Figure 2-7 Selected Raman spectra of rutile TiO ₂ nanowires collected upon compression and decompression.....	43
Figure 2-8 Selected Raman spectra of rutile TiO ₂ nanorods collected upon compression and decompression.....	44
Figure 2-9 Selected Raman spectra of flower-like TiO ₂ nanorods collected upon compression and decompression.....	45
Figure 2-10 Selected Raman spectra of TiO ₂ nanotubes collected upon compression and decompression.....	46
Figure 2-11 Pressure dependence of Raman active modes (<i>E_g</i> and <i>A_{1g}</i>) of nanowires (NW), nanorods (NR), flower-like nanorods (NF) and nanotubes (NT) TiO ₂ upon compression.....	47
Figure 2-12 Selected X-ray diffraction patterns for TiO ₂ nanowires upon compression and decompression.....	49
Figure 2-13 Rietveld refinement of XRD patterns of TiO ₂ nanowires at 1.0 GPa, 17.6 GPa, 36.3 GPa upon compression, and 0.7 GPa upon decompression.....	52
Figure 2-14 Selected X-ray diffraction patterns for TiO ₂ flower-like nanorods upon compression and decompression.....	53
Figure 2-15 Rietveld refinement of XRD patterns of flower-like nanorods at 18.3 GPa upon compression, at 0.7 GPa upon decompression.....	54
Figure 2-16 Selected X-ray diffraction patterns for TiO ₂ nanotubes upon compression and decompression.....	56
Figure 2-17 Rietveld refinement of XRD patterns at 20.8 GPa upon compression, at 0.3 GPa upon decompression.....	57
Figure 2-18 Relative lattice parameters (<i>a/a₀</i> , <i>c/c₀</i>) of rutile TiO ₂ nanowires (NW), flower-like nanorods (NF) and nanotubes (NT) as a function of compression.....	61
Figure 2-19 Equation of state for rutile TiO ₂ in morphologies of nanowires (NW), flower-like nanorods (NF), and nanotubes (NT) upon compression.....	62

Figure 3-1 SEM images of nanoflower-like spheres $\text{Li}_4\text{Ti}_5\text{O}_{12}$ (LTO-1) and nanoparticles $\text{Li}_4\text{Ti}_5\text{O}_{12}$ (LTO-2)	71
Figure 3-2 Selected Raman spectra of LTO-1 upon compression and decompression.	72
Figure 3-3 Selected Raman spectra of LTO-2 upon compression and decompression	74
Figure 3-4 Pressure dependence of Raman active mode frequencies of LTO-1 (F_{2g} , E_g , A_{1g}) and LTO-2 ($F_{2g(1)}$, $F_{2g(2)}$, E_g , A_{1g}) upon compression.....	75
Figure 3-5 Selected X-ray diffraction patterns for LTO-1 upon compression and decompression.....	78
Figure 3-6 Rietveld refinement of LTO-1 XRD patterns at 0.1 GPa, 27.1 GPa upon compression and 0.2 GPa upon decompression.....	80
Figure 3-7 Selected X-ray diffraction patterns for LTO-2 upon compression and decompression.....	82
Figure 3-8 Cell parameter ratio (a/a_0) as a function of pressure for LTO-1 and LTO-2	84
Figure 3-9 Equation of state for LTO-1 and LTO-2 upon compression.....	85

List of Appendix Tables

Table A1 Unit cell parameters of three phases for rutile TiO ₂ nanowires.....	98
Table A2 Unit cell parameters of three phases for rutile TiO ₂ flower-like nanorods	102
Table A3 Unit cell parameters of three phases for rutile TiO ₂ nanotubes.....	106

List of Appendix Figures

Figure A1 Rietveld refinement of XRD pattern for rutile TiO ₂ nanowires at 5.2 GPa, 19.3 GPa and 25.1 GPa upon compression.....	97
Figure A2 Rietveld refinement of XRD pattern for rutile TiO ₂ flower-like nanorods at 0.9 GPa, 8.3 GPa, 16.6 GPa, 24.8 GPa and (e) 34.9 GPa upon compression.....	101
Figure A3 Rietveld refinement of XRD pattern for rutile TiO ₂ nanotubes at 1.0 GPa, 18.2 GPa, 22.6 GPa, 24.3 GPa, 28.6 GPa and 35.0 GPa upon compression.....	105
Figure A4 Rietveld refinement of XRD pattern for Li ₄ Ti ₅ O ₁₂ nanoparticles at 1.3 GPa upon compression and recovered phase at 0.5 GPa.	107

List of Abbreviations

1D	One dimension
2D	Two dimension
ANL	Argonne National Laboratory
APS	Advanced Photon Source
CB	Conduction band
CCD	Charge-coupled device
DAC	Diamond anvil cell
DSSC	Dye-sensitized solar cell
FTO	Fluoride-dope tin dioxide
HM	Microwave-assisted hydrothermal
LIB	Lithium-ion battery
LTO	$\text{Li}_4\text{Ti}_5\text{O}_{12}$
LTO-1	Nanoflower-like sphere $\text{Li}_4\text{Ti}_5\text{O}_{12}$
LTO-2	Nanoparticles $\text{Li}_4\text{Ti}_5\text{O}_{12}$
NW	Nanowires
NF	Flower-like nanorods
NT	Nanotubes
PTM	Pressure transmitting medium
SEI	Solid-electrolyte interphase
SEM	Scanning electron microscopy
SSRF	Shanghai Synchrotron Radiation Facility
TEM	Transmission electron microscopy
TiO_2	Titanium dioxide

TTIP	Titanium tetraisopropoxide
UV	Ultraviolet
VB	Valence band
XRD	X-ray diffraction

Chapter 1 Introduction

1.1 Nanomaterials

The term “nano” is derived from the Greek word for “dwarf”, “nanos”. This etymology, and its placement on the metric scale ($1\text{ nm}=10^{-9}\text{ m}$), make it clear that tiny dimensions not visible to the naked eye, beyond the normal limits of our observation, are involved.¹ On this length scale, materials with at least one dimension less than 100 nm are typically termed nanomaterials. Nanomaterials mainly have three categories: zero-dimensional nanomaterials with all three dimensions in nanometer scale, such as nanoparticles and quantum dots; one-dimensional nanomaterials with two dimensions in nanometer scale, such as nanotubes, nanowires and nanorods; two dimensional nanomaterials with one dimension in nanometer scale, such as nanofilms.

When the size of particles decreased to nanoscale, the particles will possess many special characteristics²⁻⁴ as quantum size effect, surface effect, small-size effect and macro-quantum tunnel effect can result in the enhanced chemical, mechanical, optical, magnetic and electrical properties of materials. Because of these distinctive properties, nanomaterials have been widely used in various potential applications, such as energy storage,⁵ catalyst support,⁶ sensors,⁷ batteries,⁸ transistors,⁹ field emission¹⁰ and capacitors.¹¹ Nanomaterials are expected to be at the heart of the next technological revolution in solid-state electronics, to emerge as new structural materials, to serve as systems for controlled drug delivery and to have a considerable impact in particularly all domains of materials science.¹²

1.1.1 Nanostructured TiO₂

1.1.1.1 Structures and properties

Titanium dioxide (TiO₂) has been widely used in industrial applications since its commercial production in the early twentieth century. In 1972, two Japanese researchers, Fujishima and Honda discovered the phenomenon of photocatalytic

splitting of water on a TiO_2 electrode under ultraviolet (UV) light.¹³ Since then, enormous efforts have been devoted to the research of TiO_2 materials for energy conversions, which has led to many promising applications in areas ranging from photovoltaics and photocatalysis to photo-/electrochromics and sensors.¹⁴⁻¹⁸ There are three commonly known crystal structure TiO_2 , i.e., anatase, rutile and brookite in nature. Each crystalline form of TiO_2 is associated with a specific class of applications. For example, anatase TiO_2 is found to be more active than rutile in photocatalysis applications, but rutile possesses better photo-absorption property in the visible light range. In particular, the lattice structural differences among the polymorphs usually lead to multifaceted physico-chemical and opto-electronic properties that control the electronic structure and bulk diffusion ability of charge carriers.¹⁹ Among these crystalline structures, anatase and rutile phases are two most commonly studied crystal phases because of their high stabilities and rich natural abundance. The crystal structures of rutile and anatase phases are shown in Figure 1-1 (a) and (b), respectively.

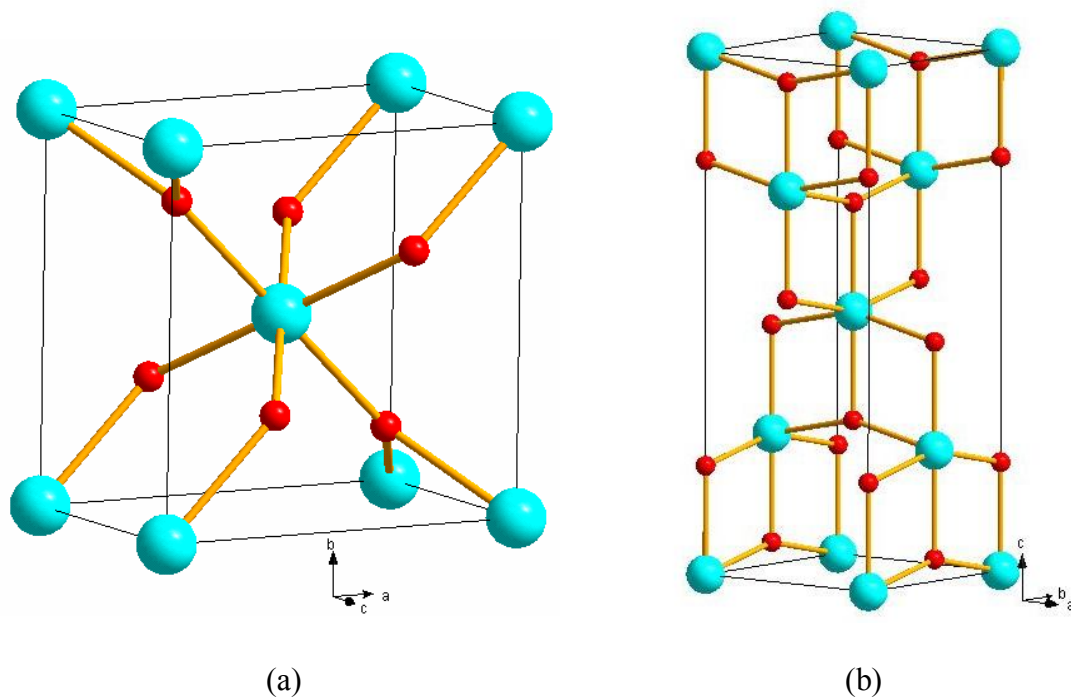


Figure 1-1 Crystal structures of TiO_2 (a): rutile phase (space group $P4_2/mnm$); (b): anatase phase (space group $I4_1/amd$). Green spheres, Ti; Red spheres, O.

New physical and chemical properties emerge when the size of the material is reduced down to the nanometer scale. For example, the surface area and surface-to-volume ratio increase dramatically as the size of material decreases.²⁰ Many TiO₂-based devices are used to facilitate reaction/interaction between the devices and the interacting media, which mainly occurs on the surface or at the interface and strongly depends on the surface area of the material. Thus, the performance of TiO₂-based devices is largely influenced by the sizes of the TiO₂ building units, apparently at the nanometer scale.²¹

In addition to size factor, the functional properties of nanomaterials are influenced by morphology. Since Iijima first time reported the needle-like carbon nanotube in 1991,²² studies of 1D nanomaterials has received increasing attention and become a research focus in recent years. It is well accepted that 1D nanostructure provides a good system to investigate the mechanical properties on dimensionality and size reduction.²³ Specifically, 1D TiO₂ nanomaterials have two quantum confined directions and one unconfined direction for electrical conduction which allows 1D TiO₂ nanomaterials to be used in applications where electrical conduction is required.²⁴

1.1.1.2 Applications

TiO₂ nanomaterials have many conventional applications such as for pigment, paint, toothpaste and sunscreens as they are very stable, nontoxic, and cheap.²⁵ Due to its electronic properties as a semiconductor and high absorption in the UV region, TiO₂ nanomaterials also have many promising applications in UV protection, photocatalysis, photovoltaics, sensing, electrochromics and so on.²⁶ Amongst all uses of TiO₂ nanomaterials, two major applications are in dye-sensitized solar cells and photocatalytic water splitting as out lined briefly below.

Dye-sensitized solar cells (DSSC): Dye-sensitized solar cells are based on dye-sensitization of a wide band gap semiconductor.²⁷ The working principle of DSSC is convert light energy into electrical energy through effective light absorption

and electricity charge separation, which is similar to photosynthesis in nature. DSSC normally contains four primary parts. On the top is a transparent anode made of fluoride-doped tin dioxide (FTO) glass. Connected to this conductive plate is a thin layer of nanostructured TiO₂ with a monolayer of the charge transfer dye attached to its surface to absorb light. Then, a separate plate is made with a thin layer of the iodide electrolyte spread over a conductive sheet (e.g. platinum metal) as cathode. The two plates are sealed together to prevent the electrolyte from leaking. When light is shined on the DSSC, the dye molecules interact with the photons and electrons are excited to a higher energy state than the conduction band edge of TiO₂, thus, electrons are injected into the conduction band of TiO₂. Then, electrons travel through the semiconductor to the electrode, the external load and finally to the counter electrode to make electric power. The holes in dye are rapidly reduced by electrolyte to prevent recombination of the electrons and holes. Overall, the device generates electric power from light without suffering any permanent chemical transformation.²⁶

Nanostructured TiO₂ is important based on the following key properties: (a) suitable band gap for electron injection from most successful commercial dyes, (b) high surface area for higher dye loading, and (c) high electronic mobility for photogenerated electron collection.²⁸

Photocatalytic water splitting: Hydrogen has been identified as a potential energy carrier due to its high energy capacity and environmental friendliness.²⁹ Many materials can be the potential sources of hydrogen such as coal,³⁰ pyrolysis oil,³¹ glucose³² and supercritical water.³³ However, in the process of hydrogen generation by using these hydrogen-containing materials, either CO₂ is produced³⁴ or energy from an external resource is required.³⁵ To pursue a friendly way of hydrogen generation, TiO₂ came onto the stage as an important component of photocatalytic splitting of water into H₂ and O₂ because of its favorable band-gap and its high stability in aqueous solution under UV irradiation.³⁶

Figure 1-2 shows the principle of water splitting using a TiO_2 photocatalyst.³⁷ When TiO_2 absorbs light with energy larger than the band gap (~ 3.2 eV), electrons in valance band will excited into conduction band, leaving holes in valance band. Then, the photogenerated electrons act as reducing agent and holes act as oxidizing agent. Water molecules are reduced by the electrons to form H_2 and oxidized by the holes to form O_2 , leading to overall water splitting.³⁸

However, TiO_2 has two main problems in this application. Firstly, the band gap of TiO_2 is about 3.2 eV and only UV light can be utilized for hydrogen production. But UV light just accounts for $\sim 4\%$ of the solar radiation energy while the visible light contributes $\sim 50\%$. This drawback limits the efficiency of solar photocatalytica H_2 production. Secondly, conduction band electrons can recombine with valance band holes quickly and release energy in the form of unproductive heat or photons. Photocatalytic splitting of water into H_2 and O_2 using TiO_2 nanomaterials continues to be a dream for clean & sustainable energy sources and there still a long way to go.

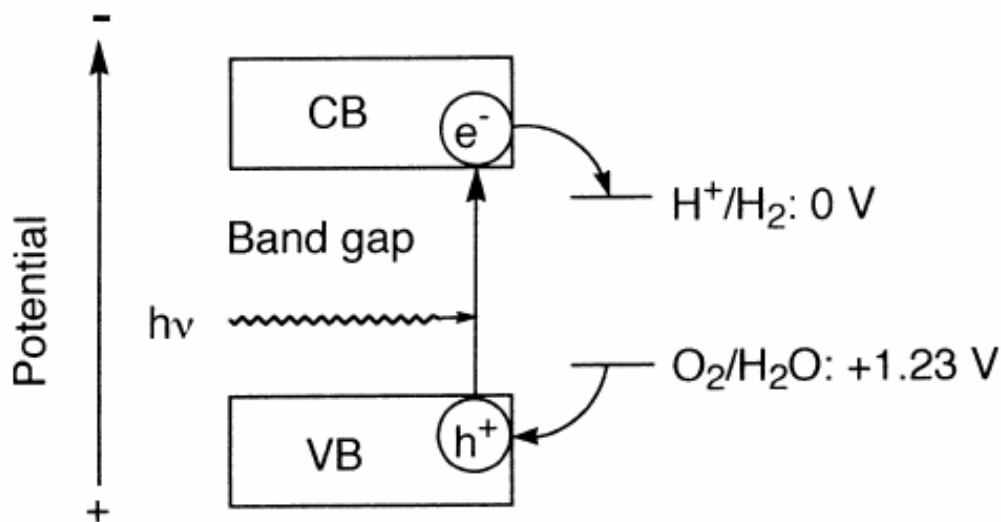


Figure 1-2 Reaction schemes for semiconductor photocatalysts.³⁷

1.1.1.3 Synthesis of one dimensional TiO₂ nanomaterials

Various techniques have been developed to synthesize nanomaterials of desired morphologies and chemical compositions, such as membrane-template methods,³⁹ sol-gel process,⁴⁰ chemical vapor deposition,⁴¹ flame or arc-discharge methods,⁴² etc. Among these methods, in particular, the hydrothermal method has been widely used to prepare one dimensional TiO₂ nanomaterials since Kasuga *et al.*⁴³ successfully synthesized TiO₂ nanotube from TiO₂-SiO₂ powder in 1998. The major advantage of hydrothermal method is that it is a simple and environmentally friendly approach.

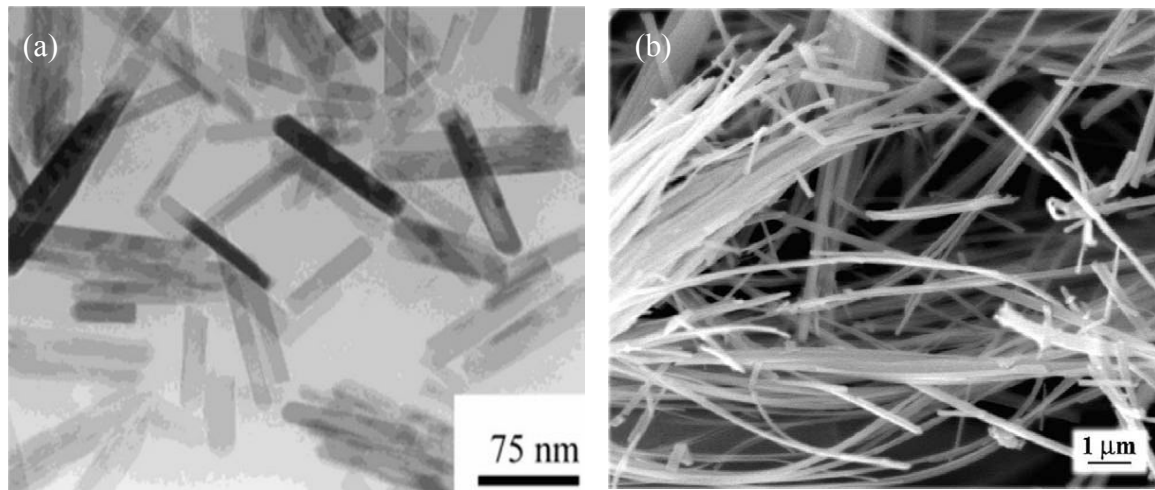


Figure 1-3 TEM and SEM images of 1D TiO₂ prepared by hydrothermal method. (a) nanorods⁴⁴ (b) nanowires.⁴⁵

Hydrothermal synthesis involves crystallization and growth of a material in the high-temperature aqueous solution at controlled temperature and/or pressure. The widely used apparatus for hydrothermal synthesis is steel pressure vessels called autoclaves with or without Teflon liners.²⁷ Many groups have successfully synthesized one dimensional TiO₂ nanomaterials by hydrothermal method. For example, Zhang *et al.*,⁴⁴ obtained TiO₂ nanorods by treating a dilute TiCl₄ solution in the presence of acid or inorganic salts. Figure 1-3 (a) shows a typical TEM image of the TiO₂ nanorods prepared with the hydrothermal method. Besides TiO₂ nanorods, TiO₂ nanowires were also synthesized with this method. For instance, Zhang *et al.*⁴⁵

obtained TiO₂ nanowires with diameter of 30 to 45 nm and a length in several micrometers (SEM images are shown in Figure 1-3 (b)). 1D TiO₂ nanomaterials investigated in Chapter 2 were also synthesised by hydrothermal method.

1.1.2 Nanostructured Li₄Ti₅O₁₂

1.1.2.1 Properties and applications

Lithium-ion batteries (LIBs) are regarded as promising new power source for hybrid electric vehicles or pure electric vehicles due to its long cycle-life and high energy density.⁴⁶ However, current technologies of LIBs are still facing some challenges in safety, cost, and service-life.⁴⁷ For instance, one of the key safety issues in LIBs for electric vehicles is the growth of dendritic lithium on the anode surface at high charging current because the conventional carbonous materials approach almost 0 V versus Li/Li⁺ at the end of Li insertion.⁴⁸ A fundamental solution is to use an electrochemical redox couple with higher equilibrium potentials, which makes Li dendrite formation thermodynamically less favorable. As such, better alternative anode materials have been sought in the past decade. Among the potential candidates, a titania based anode material, i.e., lithium titanium oxide (Li₄Ti₅O₁₂) is attractive, as its Ti⁴⁺/Ti³⁺ redox couple has an working votage of approximately 1.55 V versus lithium, which avoids the reduction of the electrolyte on the electrode surface and the formation of the solid-electrolyte interphase (SEI) layer.⁴⁹

Li₄Ti₅O₁₂ (LTO) has a spinel structure with space group of $Fd\bar{3}m$ (Figure 1-4). In Li₄Ti₅O₁₂, all the tetrahedral 16d sites are shared by lithium and titanium with an atomic ratio of 1:5 in the cubic oxyn array. Li₄Ti₅O₁₂ can be denoted as [Li₃]_{8a}[Ti₅Li]_{16d}[O₁₂]_{32e},⁵⁰ indicating that Li ions adopt both tetrahedral (occupying the 8a sites) and octahedral (occupying the 16d sites) oxygen coordination. Another interesting obervation is that Li cycling involves very little change in the cubic lattice parameter, namely, $a = 8.3595 \text{ \AA}$ for Li₄Ti₅O₁₂ and $a = 8.3538 \text{ \AA}$ for Li₇Ti₅O₁₂.⁵¹ Thus, it is a “zero-strain” material and ideally suited as an anode for LIBs. In comparison

with bulk LTO, nano-LTO showed vastly improved reversible capacities and rate capability. Such improved properties are due to the reduction of Li ion diffusion pathway and better accessibility of the electrolyte to the nanoparticles.⁵²

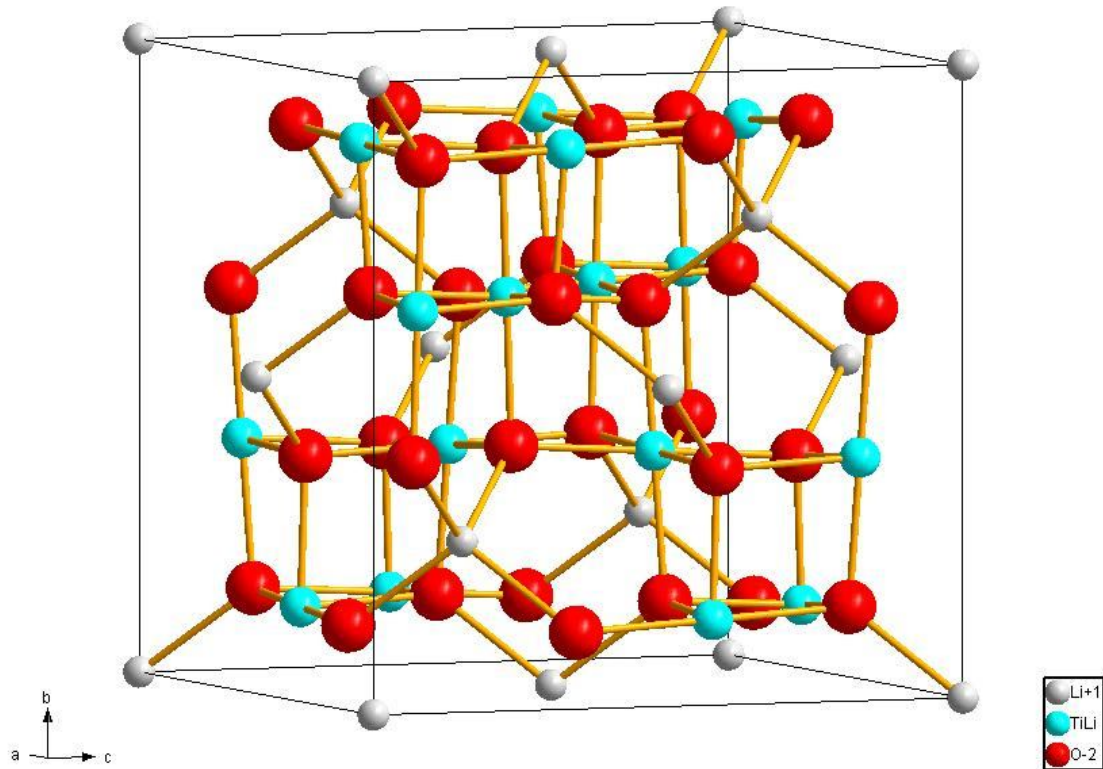


Figure 1-4 Crystal structure of $\text{Li}_4\text{Ti}_5\text{O}_{12}$. Grey spheres, Li; Green spheres, Ti / Li; Red spheres, O.

1.1.2.2 Synthesis of $\text{Li}_4\text{Ti}_5\text{O}_{12}$ nanomaterials

Due to the aforementioned advantages, many methods have been used to synthesize nanostructured LTO, such as sol-gel,⁵³ solid-state,⁵⁴ solvothermal,⁵⁵ hydrothermal⁵⁶ and spray pyrolysis.⁵⁷ Recently, microwave-assisted hydrothermal (MH) methods were found to be efficient for the synthesis of nanomaterials. Microwave-enhanced chemistry is based on the interactions of dielectric materials, liquids, or solid with microwave radiation that causes dielectric heating.⁵⁸ Specifically, for the microwave-assisted hydrothermal (MH) method, the solution is heated by a microwave irradiation under a pressure of >1 atm. It is an inexpensive one step

synthesis process in terms of energy consumption. Microwave heating is very rapid due to the direct dielectric heating of liquid relative to conventional indirect heating. For example, it takes 60-100 min to heat water up to 100-150 °C under normal hydrothermal method, while using the MH method, only 1-3 min is needed.⁵⁹ In addition, compared with conventional hydrothermal method, MH method has extremely rapid kinetics of crystallization by 1-2 orders of magnitude,⁶⁰ short reaction time, low-temperature processing and low energy consumption.⁶¹ This method has been used successfully to synthesize many inorganic nanomaterials, such as MnO₂,⁶² WO₃⁵⁹ and LiFePO₄.⁶³ The nanostructured Li₄Ti₅O₁₂ samples used in Chapter 3 are also synthesized by a MH method following heat treatment.

1.2 High pressure materials science

1.2.1 High pressure phenomena

Pressure and temperature influence properties of a chemical system. So far, much effort was focused on the variation of temperature in producing a rich array of structures and compounds. In contrast, the pressure variable in chemistry has remained relatively less explored, especially in the high pressure region. In the universe, pressure spans from 10⁻³² Pa in the intergalactic space to 10³² Pa (1 GPa = 10⁹ Pa = 10,000 atm) at the center of the neutron star. In such a large range of pressure, materials could have various structures with different properties and leave a huge space for producing new materials by adjusting pressure.⁶⁴

When applying pressure to materials, the main effect is to efficiently reduce the volume of the material as pressure can shorten the inter-molecular and intra-molecular distances. The decrease of volume will increase the free energy which causes the system thermodynamically unstable.⁶⁵ To achieve a new free energy minimum, system will result in a lot of possible processes, such as phase transformation, ionization, polymerization, amorphization, dissociation and, even metallization. Therefore, high pressure can offer enhanced opportunities to discover new phases, to

trigger chemical reactions, to force materials into new physical and chemical states. So far, a huge number of striking high-pressure phenomena have been observed experimentally. For example, as shown in Figure 1-5, butadiene can oligomerizes in the absence of a catalyst at 0.7 GPa;⁶⁶ At the pressure of 10 GPa, ice melts at 400 °C; Although no metallization has been observed experimentally for H₂, ‘broken-symmetry’ molecular-ionic solid phase (H₂⁺H₂⁻) was reported formed at a pressure of 150 GPa.⁶⁷ The recent advances in high pressure materials research have been summarized in several excellent review articles, including that by Grochala *et al.*⁶⁸

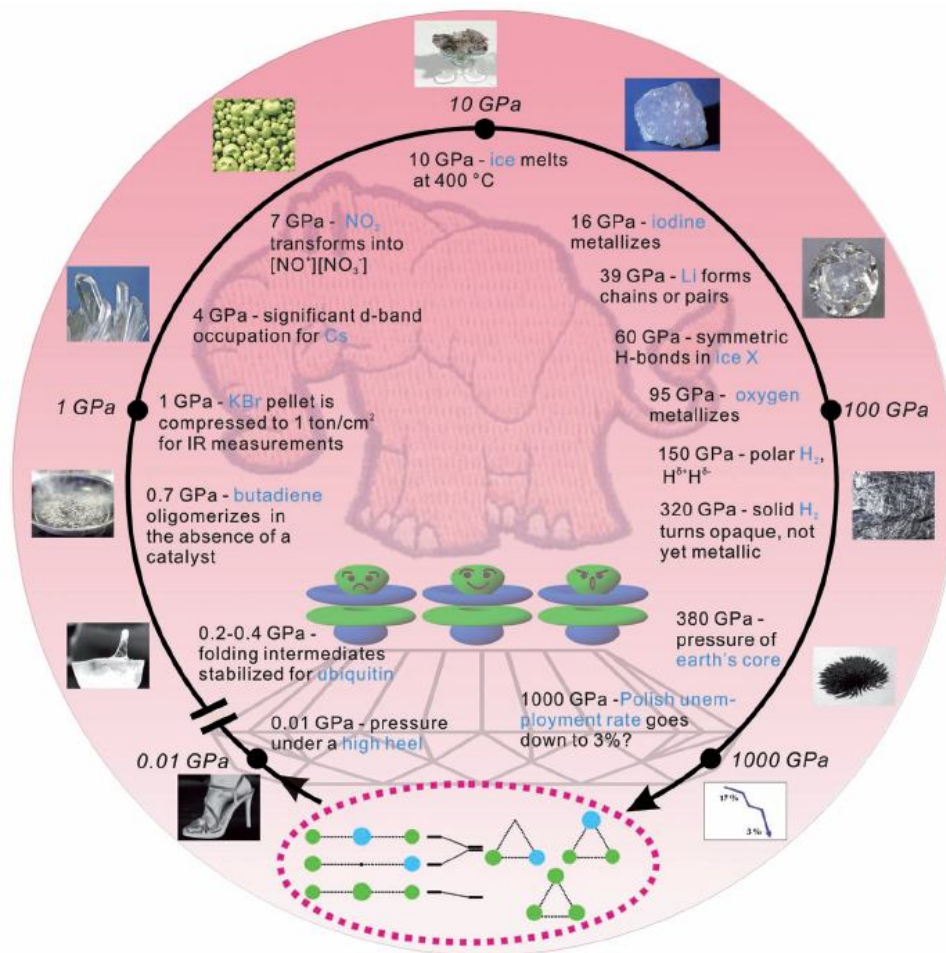


Figure 1-5 Examples of high-pressure phenomena.⁶⁸

1.2.2 High-pressure apparatus

1.2.2.1 Diamond anvil cells

Diamond anvil cell (DAC) is one of the most widely used devices to generate high pressure. It creates high pressure by trapping a sample between tiny flat faces ground on the pointy ends of two diamonds. There are many kinds of DACs, such as membrane cell from EasyLab, UK and P-type DAC from High Pressure Diamond Optics Inc. Among these, a symmetric type DAC manufactured by Princeton University is used in this project, which is shown in Figure 1-6 (a). Normally, this type of DAC is in cylinder shape with diameter of ~ 5 cm and height of ~ 2.5 cm. Pressure is provided by the four screws. The force generated by the screws can be transmitted to the backup seats which further press the two diamonds, and yield a high pressure in the gasket and sample. Symmetric DAC contains two parts: a piston and a cylinder. A pair of brilliant-cut diamonds with same size is mounted on two seats which are aligned to the piston and cylinder. There are two different types of diamonds which are classified by the content of nitrogen impurity. Type I diamonds with higher impurity (e.g. nitrogen) are used for Raman and X-ray diffraction measurement. Type II diamonds that have lower impurity are used for IR measurements. The schematic of the symmetric DAC is shown in Figure 1-6 (b). Between the two diamonds, there is a pre-indented gasket which is made of metal, such as stainless steel, tungsten, beryllium, etc. To be used in the experiment, a hole with the size of one third of the diamond's culet size will be drilled at the center of the pre-indented mark as a sample chamber and it can be perfectly sealed by the two diamonds.

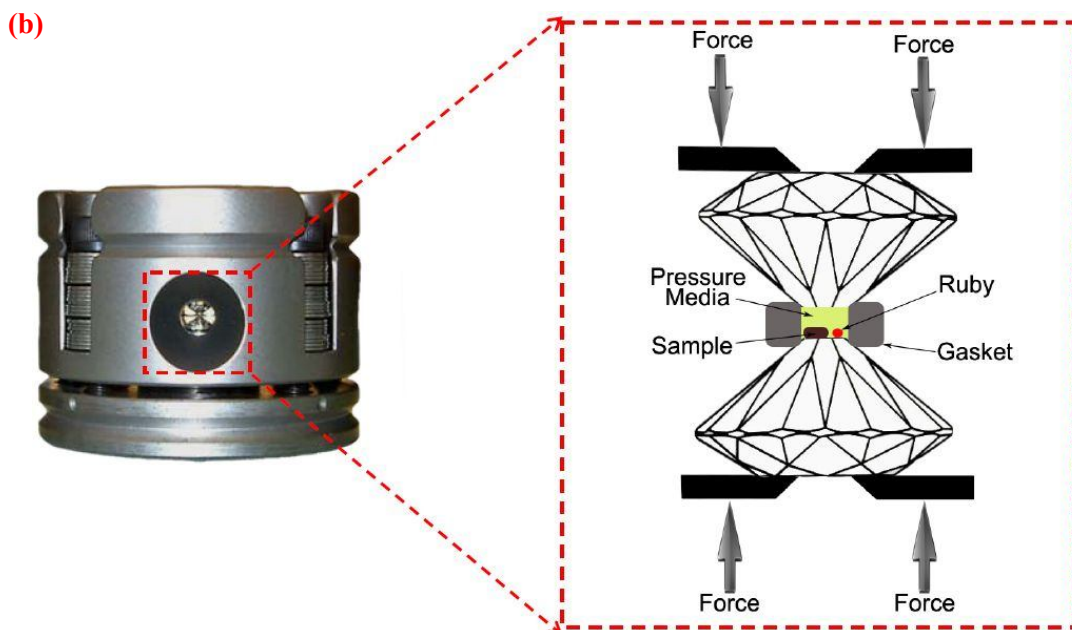
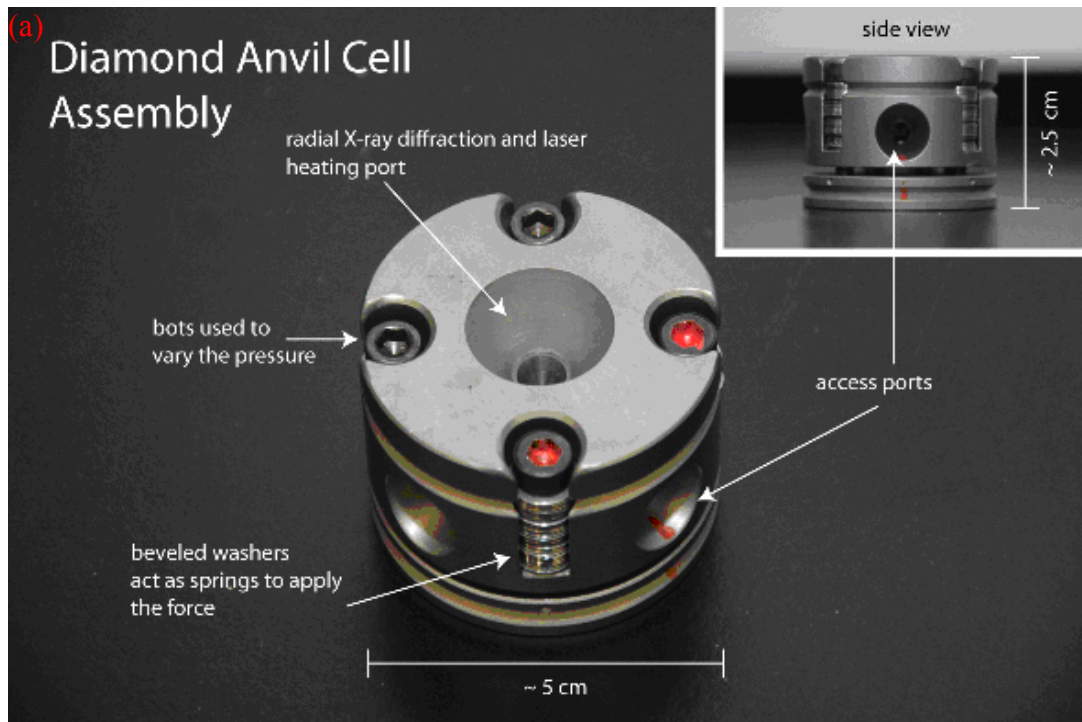


Figure 1-6 Photo (a)⁶⁹ and schematics of a symmetric diamond anvil cell (b).⁷⁰

1.2.2.2 The ruby pressure gauge

For all high pressure experiments, reliable and accurate pressure gauge is extremely important. In this thesis, a ruby gauge which is established by Mao,⁷¹ is adopted for

the *in situ* high-pressure calibration in DAC. In high pressure experiment, ruby (Al_2O_3 doped with Cr^{3+}) together with sample is loaded in the hole. Ruby has two dominant excited luminescence peaks. These two peaks are associated with R_1 and R_2 transitions involving the Cr^{3+} ion. R_1 and R_2 peaks are very sensitive to pressure and the peak position shift to longer wavelength as pressure increases. The peak position shift and pressure can be related by the equation 1.1.

$$P = \frac{1904}{B} \left[\left(1 + \frac{\Delta\lambda}{694.24} \right)^B - 1 \right] \quad (1.1)$$

In this equation, P represents pressure in GPa, $\Delta\lambda$ represents the shift of the R_1 peak. The parameter B is equal to 7.665 for quasi-hydrostatic conditions, and equal to 5 for non-hydrostatic conditions. The accuracy of this method can achieve to ± 0.05 GPa.

1.2.2.3 Pressure transmitting medium

Hydrostatical pressure is preferred for the vast majority of high pressure experiments. The reason is that hydrostatic pressure is a thermodynamic parameter and the results obtained under such conditions are intrinsic material properties which can be compared with theory.⁷² To improve the hydrostatic conditions, a pressure transmitting medium (PTM) is used to load into the sample chamber. There are many types of PTM which can maintain the hydrostatic condition up to different pressures. The first type of PTM are alcohol mixtures, such as 4:1 methanol-ethanol⁷³ and 16:3:1 methanol-ethanol- H_2O ,⁷⁴ which can keep the hydrostatic condition up to ~ 10.5 GPa. The second type of PTM is silicon oil with different viscosity, which can achieve higher pressure to 20 GPa. However, silicon oil is not suitable for pressure range of above 20 GPa, since at this pressure, it undergoes a glass phase transition and lose its pressure transmitting ability. For pressure above 20 GPa, the third class PTM, i.e. noble gases such as Ne, Ar and He, are the best hydrostatic PTM known so far. Ne, for example, can maintain the hydrostatic condition as high as 50 GPa. In general, the

choice of PTM depends on the highest pressure needed to achieve in the high pressure experiment.⁷²

1.2.3 High-pressure study of nanomaterials

Investigations of the structural and phase transformations of nanomaterials under high pressure are receiving increasing attentions. Because in addition to composition and synthetic routes, pressure provides an additional effective driving force to tune the structures and thus properties of the nanostructured materials. For instance, carbon nanotubes at around 35 GPa were found to transform into single crystal diamond or graphite powder.⁷⁵ Before this transformation, many other different nanostructures were obtained such as nanodiamond and nanotube polymers. In addition, nanomaterials behave quite differently than their corresponding bulk counterparts under pressure. For example, the phase transition of ZnO nanowires from wurtzite phase to rocksalt phase takes place at 13.7-24.1 GPa, substantially higher than that in ZnO (9 GPa).⁷⁶

Size of the nanomaterials is an important factor which influences the high-pressure behaviours. For instance, size effect is found to be significant in CdSe nanoparticles, especially for its wurtzite phase to rocksalt phase transition pressure.⁷⁷ A critical size of 10 nm is found. When the particle size of CdSe is less than 10 nm, the transition pressure increases as the particle size increases. And when the size is larger than 10 nm, the transition pressure will remain the same as its corresponding bulk counterparts.

In addition, morphology also plays a significant role in high pressure behaviors of nanomaterials. For example, different morphologies of ZnS were found to have strikingly different phase stabilities under high pressure.⁷⁸ High-pressure synchrotron X-ray diffraction of wurtzite ZnS nanobelts demonstrates a wide field of structural stability up to 6.8 GPa, remarkably different from the bulk and nanoparticles that transform to the sphalerite structure easily with slightly applied compression.

1.3 Structural characterization of nanomaterials at high pressures

Different types of techniques such as Raman, IR and XRD can be used to characterize sample in diamond anvil cell (DAC) under high pressure as diamond being transparent to a wide range of electromagnetic waves. This part will focus on the introduction of Raman spectroscopy and synchrotron X-ray diffraction that used in this project.

1.3.1 Raman spectroscopy

Raman spectroscopy is widely used for high pressure measurements since valuable information about intermolecular interactions, phase transitions, structural changes, and conversions of insulators (semiconductors) to metals is obtainable when matter is subjected to pressure.

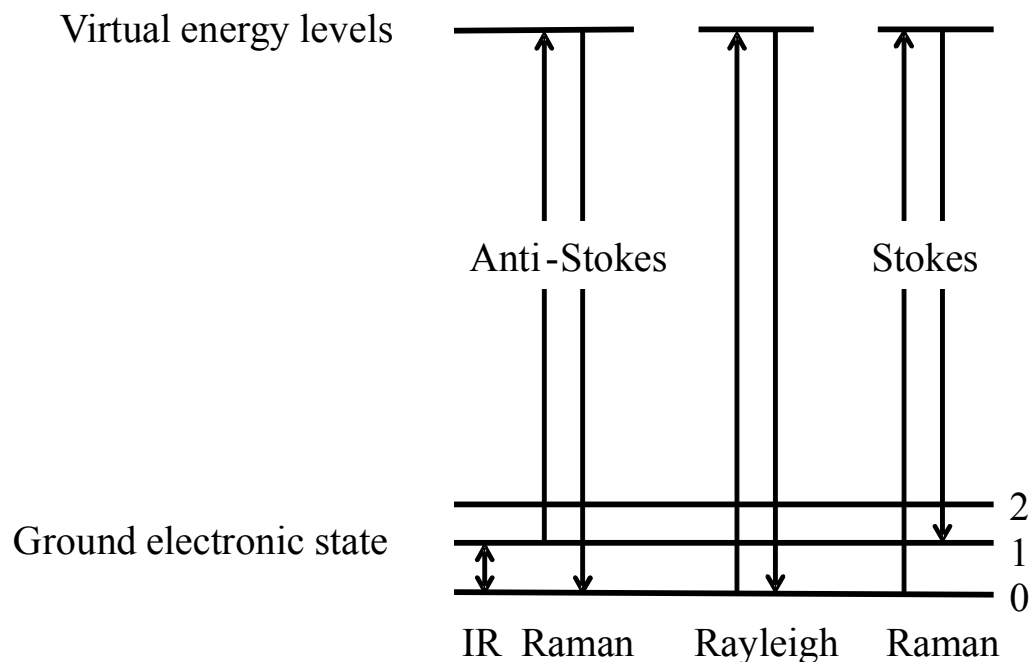


Figure 1-7 Three types of Raman scattering: Rayleigh Scattering, Stokes Raman Scattering and Anti-Stokes Raman Scattering.

When the monochromatic light interacts with gas, liquid or transparent samples, a small part of light will be scattered along different directions and generate scattered light. Scattered light can be distinguished as elastic and inelastic scattering. The major part is elastic scattering that the energy of the incident light is equal to the emitted light. And this phenomenon is referred to as Rayleigh scattering (Figure 1-7). Only a minor part scatters inelastically where a small fraction of energy is transferred between molecule and photon is called Raman scattering. Inelastic scattering can be further distinguished between two different forms, depending on the energy state of the molecule. In one case, the molecule is initially in its ground state. After excitation, the molecule falls back to a vibrational energy state above the ground state. As a result, the emitted photon has less energy than before and the scattered light will shift to a higher wavelength. This effect is called Stokes-Raman scattering. The second type of inelastic scattering assumes that the molecule is already in a higher vibrational state. After excitation, the photon falls back to the molecule's ground state. The emitted photon has a higher energy than before and the wavelength shifts to lower values. This effect is called anti-Stokes Raman scattering. Anti-Stokes-Raman scattering is weaker than Stokes-Raman scattering as most molecules are initially in their ground state. Hence Stokes-Raman scattering is mainly measured in Raman spectroscopy. The energy difference between the incident and scattering photons is called Raman shifts, which can provide valuable spectroscopic information for the vibrational or rotational energy of the sample.⁷⁹

In my project, a customized Raman micro-spectroscopy system in our lab was used to collect the Raman spectra (Figure 1-8). Two laser sources: 782 nm (Micro Laser Systems, Inc.) and 532 nm (DPSS green Laser) are used as the excitation wavelength. The microscope system containing 15× eyepieces and a 20× objective (Olympus Microscope) is used to focus the laser beam $< 5 \mu\text{m}$ onto the samples. Raman spectrum is recorded by an ultrasensitive, liquid nitrogen cooled, back-illuminated, charge-coupled device (CCD) detector (Spec-10 system, Princeton Instrument). Besides, spectrometer is equipped with a triple grating (300 g/mm, 1200 g/mm, and

1800 g/mm) system with different resolutions. For calibration, the system used neon lines with an uncertainty of $\pm 1 \text{ cm}^{-1}$. The Rayleigh scattering is removed by respective wavelength specific edge filters and an imaging spectrograph (SpectroPro-2500i, Acton Research Corporation) is used to analyze the Raman signals.

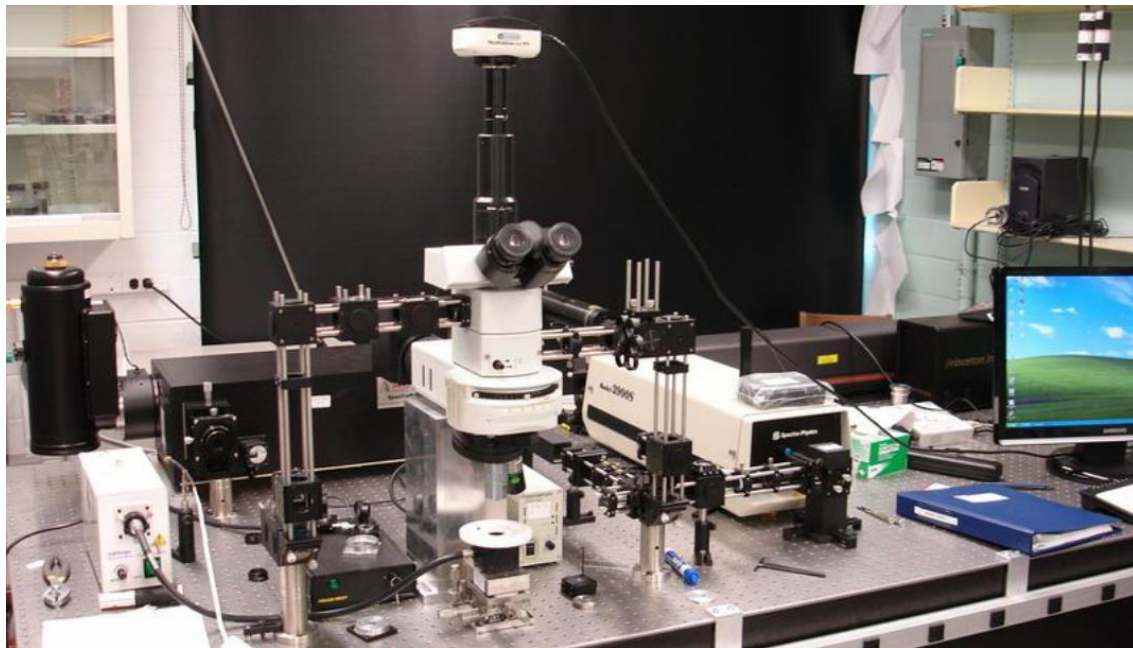


Figure 1-8 Photo of the customized in-house Raman Microspectroscopy System.⁸⁰

1.3.2 Synchrotron X-ray diffraction

1.3.2.1 Principle of synchrotron radiation

Synchrotron radiation is produced by accelerating electrons approaching the speed of light.⁸¹ More specifically, as shown in Figure 1-9, the high energy electrons are first accelerated to the speed of close to light, and next are injected to the storage ring that guided by arrays of magnet, then, electromagnetic radiation is produced tangentially to the curved orbit of accelerated electrons. The storage ring includes an array of several magnets in straight sections and curved sections, which constrain an electron or positron beam to move in a circular path.

In the curved sections, bending magnets are located, which bend the electron beam and effectively generates a sweeping searchlight pattern. In the straight sections, the “insertion devices” are placed which contains wigglers and undulators. As the electron beam bend along the orbit of curved section, a bending magnet produces sharp cone of radiation in the bending plane, shown in Figure 1-10 a. Due to the high magnetic field in wigglers, radiation beam generated in wigglers has a large open angle (Figure 1-10 b). However, compared with wigglers, undulators have a low magnetic field. Therefore, the radiation beam generated in undulators has a small open angle, which leads to a narrower beam of higher brightness (see Figure 1-10 c). As seen in Figure 1-10, radiated energy is continuous for both bending magnet and wigglers, but it is a series of sharp peaks for undulators.⁸²

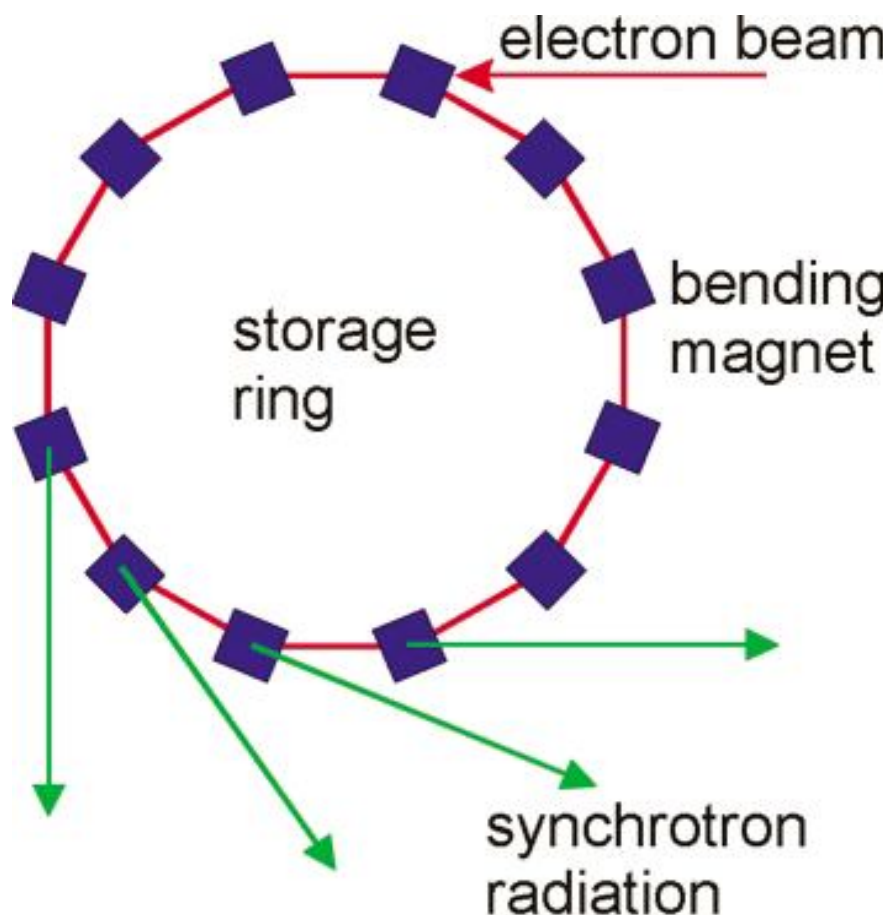


Figure 1-9 Schematic layout of a synchrotron radiation facility.⁸³

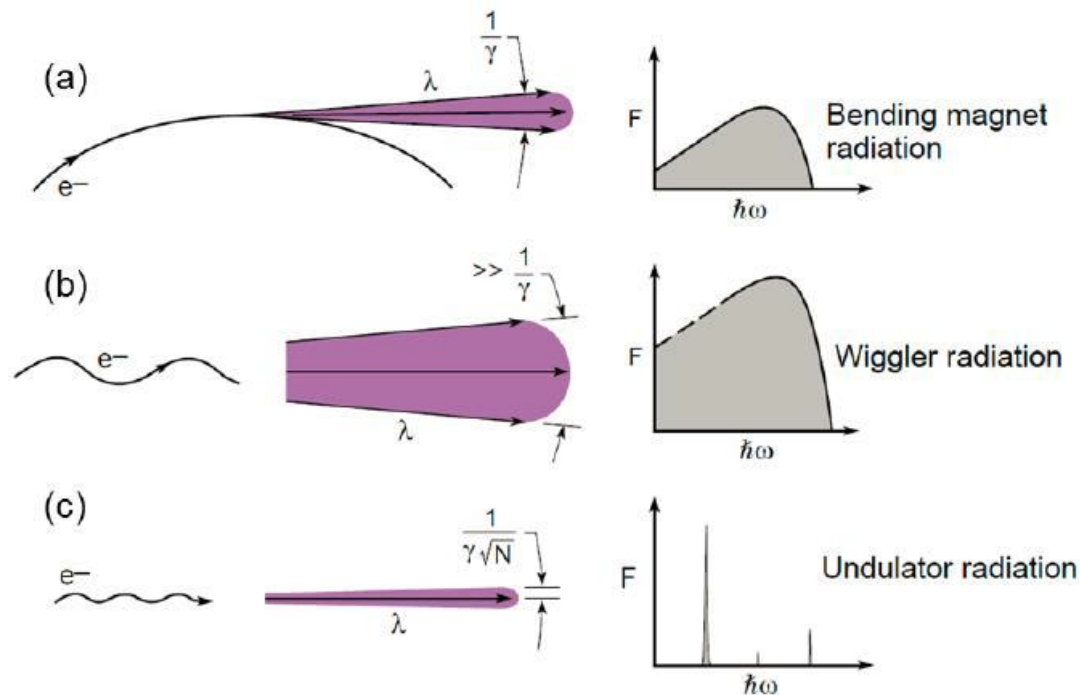


Figure 1-10 Opening angle and flux (vs. E_{photon}) of (a) bending magnets, (b) wigglers, and (c) undulators.⁸⁴

Compared with traditional X-ray sources, synchrotron radiation has many advantages. The brilliance of the X-ray beam that can be achieved in synchrotrons is four (first generation synchrotrons) to twelve (third generation synchrotrons) orders of magnitude higher than that from a conventional X-ray source. Moreover, given the size of the storage ring (hundreds of meters in diameter), the average synchrotron beam consists of weakly divergent beams that may be considered nearly parallel, which increases the instrumental resolution significantly in contrast to laboratory X-ray source. Another important advantage is that energy of the synchrotron radiation is consistency and tunable to desired experimental requirement.⁸⁵ Moreover, synchrotron radiation also possesses other desirable properties such as polarization, laser-like coherence and time-structures which make synchrotron radiation is a versatile tool of studying the chemical and physical properties of materials.

1.3.2.2 Synchrotron X-ray diffraction at high pressure

X-ray diffraction (XRD) has been widely used in the identification and characterization of crystalline solids. Both the position and the relative intensity of a diffraction pattern are providing a “fingerprint” for a particular phase. XRD can also be used to determine the crystallinity by comparing the intensity of the background pattern to that of the sharp peaks. The basic principle for XRD is the Bragg equation shown below which is formulated by W.H.Bragg and W.L.Bragg.⁸⁶ It establishes relationships among the diffraction angle (Bragg angle), wavelength, and interplanar spacing.

$$\lambda = 2d_{hkl} \sin \theta \quad (1.2)$$

Where λ is the wavelength of X-ray; d_{hkl} is the spacing of the lattice planes with the Miller indices h, k, l . θ is the angle of Bragg reflection with respect to these planes. The diffraction angle, defined as the angle between the incident primary beam and the diffracted beam, is therefore equal to 2θ . For ideal polycrystalline samples with all possible orientations of the individual microcrystalline grains are equally probable, the X-ray is scattered symmetrically around the primary beam into discrete diffraction cones, which can be registered photographically as concentric circles on a flat film, or more commonly, as Debye-Scherrer rings on a cylindrical film wrapped around the sample with the primary beam passing through the film on one side, and through the collimator hole on the other side.

In high-pressure studies, due to the bulk anvils and small sample sizes, X-ray diffraction measurements can only be performed with intense high energy X-ray beam and very small beam size (*e.g.*, tens of microns), which can hardly be achieved in local X-ray diffraction facilities using Co, Cu, and Mo as the excitation sources. Therefore, Synchrotron radiation source becomes the best choice for high-pressure research due to its extraordinary properties mentioned above.

1.3.2.3 Synchrotron X-ray diffraction facilities

The XRD patterns in this thesis were collected in angle dispersive X-ray diffraction mode in which Bragg's Law is fulfilled by using a fixed X-ray wavelength λ , and scanning in angle θ , as described in Figure 1-11. The monochromatic synchrotron X-ray beam passing through diamond is focused at the center of the sample. X-ray diffraction patterns are collected on the other side. The XRD experiments in this thesis were carried out using the synchrotron facilities at Advanced Photon Source (APS) in Argonne National Laboratory (ANL) and Shanghai Synchrotron Radiation Facility (SSRF) in China.

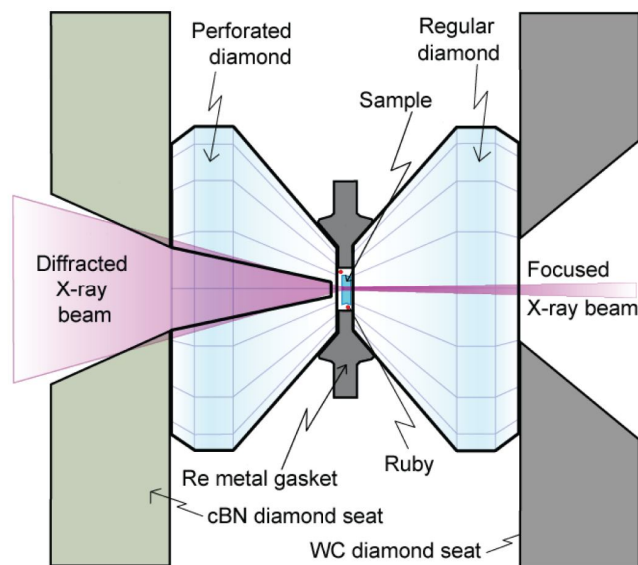


Figure 1-11 Schematic diagram of angle dispersive XRD.⁸⁷

Advanced Photon Source (APS) Advanced Photon Source (APS) is located at Argonne National Laboratory, Argonne, USA. It consists of 34 sectors, and each sector contains one or more beamlines for a variety of researches. The XRD patterns of nanoparticles $\text{Li}_4\text{Ti}_5\text{O}_{12}$ in Chapter 3 were obtained from beamline HPCAT 16BM-D as shown in Figure 1-12. It is a high-pressure beamline for X-ray diffraction measurements. The X-ray energy can be chosen by Si (1 1 1) double crystal monochromator from the APS bending magnet beam and the energy range covers 6-45 keV normally. The monochromatic X-ray beam is focused by KB mirrors both in

vertical and horizontal dimensions, which normally provide a full beam size of 15 μm (H) x 30 μm (V) at the sample. A MAR345 imaging plate detector is used to collect the diffraction patterns of the sample.⁸⁹ In addition to the XRD technique, 16BM-D also provides many excellent technical supports such as the membrane and mechanical pressure control, online ruby and Raman system.

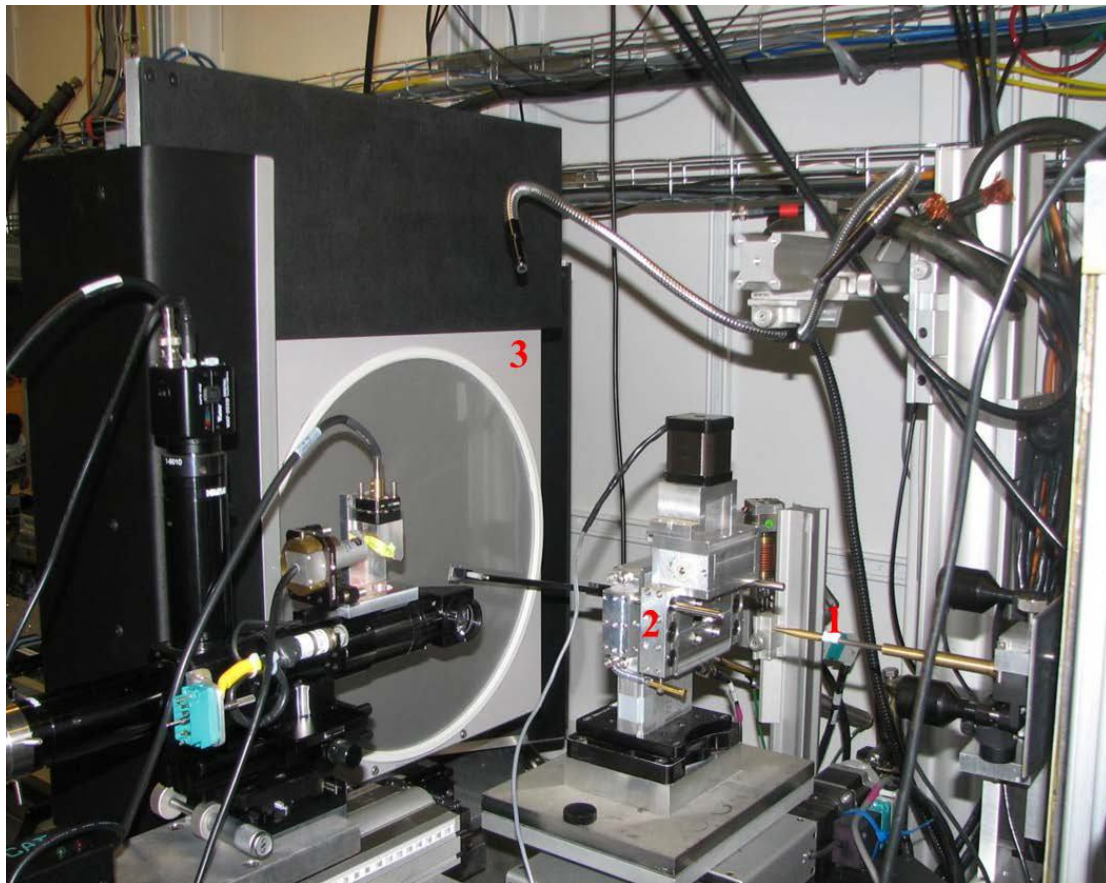


Figure 1-12 Angle dispersive XRD set up at 16BM-D of APS.⁸⁸ 1: X-ray beam; 2: sample stage; 3: MAR3450 image plate.

Another beamline of Sector-20ID in APS was used to obtain XRD patterns for all 1D rutile TiO_2 nanomaterials in Chapter 2. Sector-20 is a partnership beamline between the X-ray Science Division and the Canadian Light Source. The source for Sector-20ID is the undulator Type A. Its energy range covers 4.3-27 keV by monochromator of Si (1 1 1).⁸⁹ Besides XRD, it can also support other techniques, such as X-ray absorption fine structure (XAFS) and X-ray Raman Scattering.

Shanghai Synchrotron Radiation Facility (SSRF) Shanghai Synchrotron Radiation Facility (SSRF) is the third generation synchrotron radiation facility which located in Shanghai, China. Its circumference is 432 m and the operating energy is 3.5 GeV. 7 beamlines are in operation now. BL15U1 is called micro-focusing beamline which is the only one that is suitable for high pressure study so far because of its micron beam size. The XRD patterns of nanoflower-like spheres $\text{Li}_4\text{Ti}_5\text{O}_{12}$ in Chapter 3 were obtained in this beamline. The layout of the beamline is shown in Figure 1-13. A Si (1 1 1) double crystal monochromator is used to monochromize X-rays. The energy range provided is 5-20.5 keV. The flux is more than 10^{11} photons/s· μm^2 @ 10 keV. The micron beam size is achieved by using a K-B mirror system. The setup of μ -XRD at BL15U1 is optimized for high pressure experiment is shown in Figure 1-14, after the K-B focusing system (1), the beam is focused to the sample (4). A pin-hole (3) was placed before the sample in order to get a clean beam profile. A Mar-165 CCD (6) was used for recording the diffraction signal, and a beam stop (5) is also placed in front of the CCD for protection purpose. A movable PIN diode as photon detector was placed between sample and beam-stop in order to help to focus the beam on to the sample, and it can quickly move in and out of the beam path for observation and measurement mode switching.⁹⁰

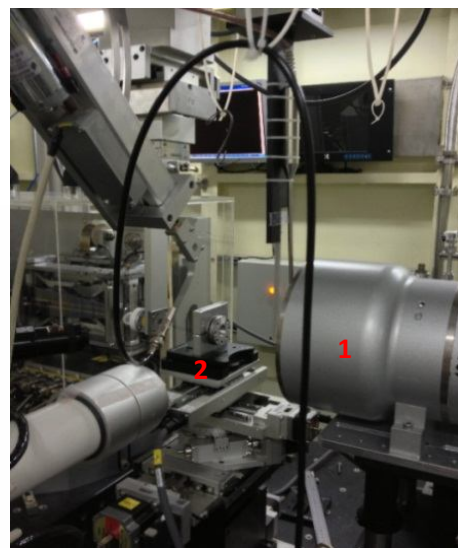
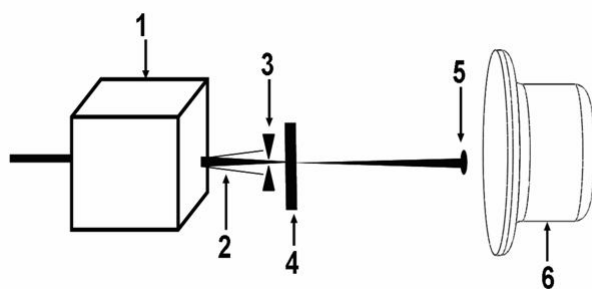


Figure 1-13 The Schematic layout (left) and photo (right) of μ -XRD setup at BL15U1.⁹⁰

1: X-ray beam; 2: sample stage.

1.3.3 Other characterization techniques

1.3.3.1 Scanning electron microscope (SEM)

Scanning electron microscope (SEM) is used to characterize the morphologies of nanomaterials, In this thesis, SEM images were collected by using the LEO 1540 FIB/SEM at Western Nanofabrication Facility, the University of Western Ontario. The LEO 1540 is equipped with a high resolution SEM for imaging. The spatial resolution of the images can focus down to 1 nm depending on the materials.

1.3.3.2 Powder X-ray diffraction

The conventional powder X-ray diffraction facility in Department of Earth Science is also used to check the phase and crystallinity of the products at ambient condition. These experiments were performed on a Rigaku rotating-anode X-ray Diffractometer. The diffractometer employs Co K-radiation ($\lambda = 1.78890 \text{ \AA}$) as X-ray source. The monochromatic condition is achieved using a curved crystal, diffracted beam, graphite monochromator. The instrument is using the normal scan rate of 10 degree two-theta per minute. X-rays were collimated using 1 degree divergent and scatter slits, and a 0.15 mm receiving slit. Bulk sample scans were completed from 2 to 82 degree two-theta, at a rate of 10 degree / minute.

1.4 Scope of the thesis

The properties of nanomaterials are largely determined by the synthetic routes and their compositions. However, high-pressure studies have demonstrated that, in addition to the traditional synthetic approaches, pressure can provide an additional driving force to modify the structures as well as morphology of nanomaterials. One of the benefits of high pressure study is pressure induced phase transformation of producing novel structures which may have new potential applications especially in energy devices. Therefore, high-pressure study of nanomaterials has attracted increasing attentions in recent years.

As mentioned above, the chemical and physical properties of 1D nanostructured TiO₂ have been widely studied since they have a much higher surface to volume ratio, which maximize the dye loading and light harvesting properties while maintaining its high electron transport ability. Until now, basic properties of nanostructured TiO₂ in different crystal phases and morphologies using different synthesis methods, which are closely related to its applications, are not yet fully understood. Comparing with anatase phase, the high-pressure behaviors of rutile nanosized TiO₂ is still lack of understanding. Therefore, high-pressure studies of rutile 1D nanostructured TiO₂ are of fundamental importance.

My second project in Chapter 3 is another titania based energy storage material: nanostructured Li₄Ti₅O₁₂. As a potential anode material for lithium-ion battery, nanostructured Li₄Ti₅O₁₂ shows a number of improved characteristics compared with carbon-based anode materials. However, structural modifications of nanostructured Li₄Ti₅O₁₂ materials under high pressure may lead to better electrochemical properties.

To the best of our knowledge, no experimental high-pressure studies on 1D rutile nanostructured TiO₂ and nanostructured Li₄Ti₅O₁₂ have been undertaken, many outstanding issues, such as phase transition sequence, phase transition pressure, high pressure phases, compressibility, systematic understanding of morphology and size effect, etc, still remain to be addressed. Therefore, *in-situ* Raman spectroscopy and X-ray diffraction high-pressure study of 1D rutile nanostructured TiO₂ (Chapter 2) and two different morphologies of nanostructured Li₄Ti₅O₁₂ (Chapter 3) are carried out in this thesis.

1.5 References

- (1) Goesmann, H.; Feldmann, C. *Angew. Chem.-Int. Edit.* **2010**, *49*, 1362.
- (2) Ball, P.; Garwin, L. *Nature* **1992**, *355*, 761.
- (3) Halperin, W. P. *Rev. Mod. Phys.* **1986**, *58*, 533.
- (4) Feldheim, D. L.; Keating, C. D. *Chem. Soc. Rev.* **1998**, *27*, 1.

- (5) Britto, P. J.; Santhanam, K. S. V.; Rubio, A.; Alonso, J. A.; Ajayan, P. M. *Adv. Mater.* **1999**, *11*, 154.
- (6) Rodriguez, N. M.; Kim, M. S.; Baker, R. T. K. *J. Phys. Chem.* **1994**, *98*, 13108.
- (7) Ansari, S. G.; Boroojerdian, P.; Sainkar, S. R.; Karekar, R. N.; Aiyer, R. C.; Kulkarni, S. K. *Thin Solid Films* **1997**, *295*, 271.
- (8) Paek, S. M.; Yoo, E.; Honma, I. *Nano Lett.* **2009**, *9*, 72.
- (9) Wan, Q.; Dattoli, E. N.; Lu, W. *Appl. Phys. Lett.* **2007**, *90*.
- (10) Wang, D. Z.; Wen, S. L.; Chen, J.; Zhang, S. Y.; Li, F. Q. *Phys. Rev. B* **1994**, *49*, 14282.
- (11) Prasad, K. R.; Miura, N. *Electrochem. Commun.* **2004**, *6*, 849.
- (12) San-Miguel, A. *Chem. Soc. Rev.* **2006**, *35*, 876.
- (13) Fujishima, A.; Honda, K. *Nature* **1972**, *238*, 37.
- (14) Joo, J. B.; Dahl, M.; Li, N.; Zaera, F.; Yin, Y. D. *Energy Environ. Sci.* **2013**, *6*, 2082.
- (15) Jing, L. Q.; Zhou, W.; Tian, G. H.; Fu, H. G. *Chem. Soc. Rev.* **2013**, *42*, 9509.
- (16) Wang, Y. J.; Wang, Q. S.; Zhan, X. Y.; Wang, F. M.; Safdar, M.; He, J. *Nanoscale* **2013**, *5*, 8326.
- (17) Liu, S. W.; Yu, J. G.; Jaroniec, M. *Chem. Mat.* **2011**, *23*, 4085.
- (18) Kim, G.; Jo, C.; Kim, W.; Chun, J.; Yoon, S.; Lee, J.; Choi, W. *Energy Environ. Sci.* **2013**, *6*, 2932.
- (19) Carp, O.; Huisman, C. L.; Reller, A. *Prog. Solid State Chem.* **2004**, *32*, 33.
- (20) Alivisatos, A. P. *J. Phys. Chem.* **1996**, *100*, 13226.
- (21) Chen, X. B.; Lou, Y. B.; Dayal, S.; Qiu, X. F.; Krolicki, R.; Burda, C.; Zhao, C. F.; Becker, J. J. *Nanosci. Nanotechnol.* **2005**, *5*, 1408.
- (22) Iijima, S. *Nature* **1991**, *354*, 56.
- (23) Xia, Y. N.; Yang, P. D.; Sun, Y. G.; Wu, Y. Y.; Mayers, B.; Gates, B.; Yin, Y. D.; Kim, F.; Yan, Y. Q. *Adv. Mater.* **2003**, *15*, 353.
- (24) Marin, F. I.; Hamstra, M. A.; Vanmaekelbergh, D. *J. Electrochem. Soc.* **1996**, *143*, 1137.
- (25) Pfaff, G.; Reynders, P. *Chem. Rev.* **1999**, *99*, 1963.

- (26) Gratzel, M. *Nature* **2001**, *414*, 338.
- (27) Chen, X.; Mao, S. S. *Chem. Rev.* **2007**, *107*, 2891.
- (28) Cahen, D.; Hodes, G.; Gratzel, M.; Guillemoles, J. F.; Riess, I. *J. Phys. Chem. B* **2000**, *104*, 2053.
- (29) Muradov, N. Z.; Veziroglu, T. N. *Int. J. Hydrog. Energy* **2008**, *33*, 6804.
- (30) Coughlin, R. W.; Farooque, M. *Nature* **1979**, *279*, 301.
- (31) Wang, D.; Czernik, S.; Montane, D.; Mann, M.; Chornet, E. *Ind. Eng. Chem. Res.* **1997**, *36*, 1507.
- (32) Sato, S.; Lin, S. Y.; Suzuki, Y.; Hatano, H. *Fuel* **2003**, *82*, 561.
- (33) Cortright, R. D.; Davda, R. R.; Dumesic, J. A. *Nature* **2002**, *418*, 964.
- (34) Cormos, C. C.; Starr, F.; Tzimas, E.; Peteves, S. *Int. J. Hydrog. Energy* **2008**, *33*, 1286.
- (35) Zhou, H. S.; Wang, Y. G.; Li, H. Q.; He, P. *ChemSusChem* **2010**, *3*, 1009.
- (36) Ni, M.; Leung, M. K. H.; Leung, D. Y. C.; Sumathy, K. *Renew. Sust. Energ. Rev.* **2007**, *11*, 401.
- (37) Kudo, A. *Catal. Surv. Asia* **2003**, *7*, 31.
- (38) Hameed, A.; Gondal, M. A. *J. Mol. Catal. A-Chem.* **2004**, *219*, 109.
- (39) Yang, D.; Qi, L. M.; Ma, J. M. *Adv. Mater.* **2002**, *14*, 1543.
- (40) Azizi, K. F.; Bagheri-Mohagheghi, M. M. *J. Sol-Gel Sci. Technol.* **2013**, *65*, 329.
- (41) Chadwick, N.; Sathasivam, S.; Kafizas, A.; Bawaked, S. M.; Obaid, A. Y.; Al-Thabaiti, S.; Basahel, S. N.; Parkin, I. P.; Carmalt, C. J. *J. Mater. Chem. A* **2014**, *2*, 5108.
- (42) Niu, F.; Li, S. Q.; Zong, Y. C.; Yao, Q. *J. Phys. Chem. C* **2014**, *118*, 19165.
- (43) Kasuga, T.; Hiramatsu, M.; Hoson, A.; Sekino, T.; Niihara, K. *Langmuir* **1998**, *14*, 3160.
- (44) Zhang, Q. H.; Gao, L. *Langmuir* **2003**, *19*, 967.
- (45) Zhang, Y. X.; Li, G. H.; Jin, Y. X.; Zhang, Y.; Zhang, J.; Zhang, L. D. *Chem. Phys. Lett.* **2002**, *365*, 300.
- (46) Armand, M.; Tarascon, J. M. *Nature* **2008**, *451*, 652.
- (47) Goodenough, J. B.; Kim, Y. *Chem. Mat.* **2010**, *22*, 587.

- (48) Yi, T. F.; Jiang, L. J.; Shu, J.; Yue, C. B.; Zhu, R. S.; Qiao, H. B. *J. Phys. Chem. Solids* **2010**, *71*, 1236.
- (49) Zaghbi, K.; Armand, M.; Gauthier, M. *J. Electrochem. Soc.* **1998**, *145*, 3135.
- (50) Yi, T. F.; Yang, S. Y.; Xie, Y. *J. Mater. Chem. A* **2015**, *3*, 5750.
- (51) Yang, Z. G.; Choi, D.; Kerisit, S.; Rosso, K. M.; Wang, D. H.; Zhang, J.; Graff, G.; Liu, J. *J. Power Sources* **2009**, *192*, 588.
- (52) Amine, K.; Belharouak, I.; Chen, Z. H.; Tran, T.; Yumoto, H.; Ota, N.; Myung, S. T.; Sun, Y. K. *Adv. Mater.* **2010**, *22*, 3052.
- (53) Alias, N. A.; Kufian, M. Z.; Teo, L. P.; Majid, S. R.; Arof, A. K. *J. Alloy. Compd.* **2009**, *486*, 645.
- (54) Yuan, T.; Cai, R.; Ran, R.; Zhou, Y. K.; Shao, Z. P. *J. Alloy. Compd.* **2010**, *505*, 367.
- (55) Lee, D. K.; Shim, H. W.; An, J. S.; Cho, C. M.; Cho, I. S.; Hong, K. S.; Kim, D. W. *Nanoscale Res. Lett.* **2010**, *5*, 1585.
- (56) Chen, J. Z.; Yang, L.; Fang, S. H.; Tang, Y. F. *Electrochim. Acta* **2010**, *55*, 6596.
- (57) Ju, S. H.; Kang, Y. C. *J. Power Sources* **2010**, *195*, 4327.
- (58) Kappe, C. O. *Angew. Chem.-Int. Edit.* **2004**, *43*, 6250.
- (59) Phuruangrat, A.; Ham, D. J.; Hong, S. J.; Thongtem, S.; Lee, J. S. *J. Mater. Chem.* **2010**, *20*, 1683.
- (60) Komarneni, S.; Rajha, R. K.; Katsuki, H. *Mater. Chem. Phys.* **1999**, *61*, 50.
- (61) Zhang, J. W.; Wang, Y. A.; Yang, J. J.; Chen, J. M.; Zhang, Z. J. *Mater. Lett.* **2006**, *60*, 3015.
- (62) Nyutu, E. K.; Chen, C. H.; Sithambaram, S.; Crisostomo, V. M. B.; Suib, S. L. *J. Phys. Chem. C* **2008**, *112*, 6786.
- (63) Murugan, A. V.; Muraliganth, T.; Manthiram, A. *J. Phys. Chem. C* **2008**, *112*, 14665.
- (64) Dong, Z. H., Ph.D. Thesis, University of Western Ontario, London. **2012**.
- (65) Hemley, R. J. *Annu. Rev. Phys. Chem.* **2000**, *51*, 763.
- (66) Citroni, M.; Ceppatelli, M.; Bini, R.; Schettino, V. *Science* **2002**, *295*, 2058.
- (67) Hanfland, M.; Hemley, R. J.; Mao, H. K. *Phys. Rev. B* **1991**, *43*, 8767.

(68) Grochala, W.; Hoffmann, R.; Feng, J.; Ashcroft, N. W. *Angew. Chem.-Int. Edit.* **2007**, *46*, 3620.

(69) Adapted from:

http://serc.carleton.edu/NAGTWorkshops/mineralogy/mineral_physics/diamond_anvil.html

(70) Hashim, A.; *Nanowires Fundamental Research*. INTECH: Croatia, **2011**.

(71) Mao, H. K.; Xu, J.; Bell, P. M. *Journal of Geophysical Research-Solid Earth and Planets* **1986**, *91*, 4673.

(72) Klotz, S.; Chervin, J. C.; Munsch, P.; Le Marchand, G. *J. Phys. D-Appl. Phys.* **2009**, *42*.

(73) Marshall, W. G.; Francis, D. J. *J. Appl. Crystallogr.* **2002**, *35*, 122.

(74) Angel, R. J.; Bujak, M.; Zhao, J.; Gatta, G. D.; Jacobsen, S. D. *J. Appl. Crystallogr.* **2007**, *40*, 26.

(75) Blank, V. D.; Denisov, V. N.; Kirichenko, A. N.; Lvova, N. A.; Martyushov, S. Y.; Mavrin, B. N.; Popova, D. M.; Popov, M. Y.; Tat'yanin, E. V.; Zakhidov, A. A. *Physica B* **2006**, *382*, 58.

(76) Dong, Z. H.; Zhuravlev, K. K.; Morin, S. A.; Li, L. S.; Jin, S.; Song, Y. *J. Phys. Chem. C* **2012**, *116*, 2102.

(77) Tolbert, S. H.; Alivisatos, A. P. *J. Chem. Phys.* **1995**, *102*, 4642.

(78) Wang, Z. W.; Daemen, L. L.; Zhao, Y. S.; Zha, C. S.; Downs, R. T.; Wang, X. D.; Wang, Z. L.; Hemley, R. J. *Nat. Mater.* **2005**, *4*, 922.

(79) John R. Ferraro, K. N., and Chris W. Brown *Introductory Raman Spectroscopy*. Academic press: California:, 2003.

(80) Ankang, Z., M.Sc. Thesis, University of Western Ontario, London. **2013**.

(81) Doniach, H. W. a. S., Ed., *Synchrotron Radiation Research*; Plenum Press: New York, **1980**.

(82) Winich, H., *Synchrotron Radiation Sources: a primer*. World Science: **1994**.

(83) Clegg, W. *J. Chem. Soc.-Dalton Trans.* **2000**, 3223.

(84) Adapted from:

<http://ast.coe.berkeley.edu/srms/2007/Intro2007.pdf>

(85) Y. Zavalij, V. K. P. a. P. *Fundamentals of Powder Diffraction and Structural Characterization of Materials*; Springer Science+Business Media, Inc.: New York, **2005**.

(86) W. H. Bragg, W. L. B. *Proc R. Soc. Lond. A* **1913**, 88, 428.

(87) Adapted from:

http://d32ogoqmya1dw8.cloudfront.net/images/NAGTWorkshops/mineralogy/mineral_physics/generalized_dac_figure.png.

(88) Adapted from:

<http://hpcat.carnegiescience.edu/beamlines/bm-d>.

(89) Adapted from:

<http://s20.xray.aps.anl.gov/id.html>.

(90) SSRF- BL15U1 User Manual.

Chapter 2 Pressure-induced Structural Transformations of 1D Nanostructured TiO₂ Studied by Raman Spectroscopy and Synchrotron X-ray Diffraction

2.1 Introduction

With the rapid development of the nanotechnologies, TiO₂ nanomaterials with different morphologies (e.g. nanoparticles, nanowires, nanobelts, nanotubes)¹⁻⁴ can be produced in high quality for subsequent applications such as photocatalysis, photovoltaics, batteries, photonic and UV blockers.⁵⁻⁹ Compared to other nanostructured materials, 1D TiO₂ nanomaterials have attracted considerable interest due to their superior properties in different applications, especially in photocatalysis and solar cells.¹⁰⁻¹²

The most commonly known stable phases of crystalline structured TiO₂, include anatase (space group *I4₁/amd*), rutile (space group *P4₂/mnm*), and brookite (space group *Pbcn*) in nature. Each crystalline form of TiO₂ is associated with a specific class of applications. For instance, rutile has a high refractive index, exceptional light scattering efficiency and UV absorptivity, which enables its utility as a filter in solar creams, pigments and optical communication devices (eg. isolators, modulators), while anatase is largely preferred in photocatalysis and photovoltaics.¹³ Therefore, searching structures with properties that can satisfy the applications is of particular interest.

In addition to composition and synthetic routes, pressure provides an additional effective driving force to tune the structures and thus properties of the nanostructured materials.¹⁴ So far, pressure-induced structural transformation have been observed in many nanomaterials, such as ZnS,¹⁵ SnO₂,¹⁶ BN,¹⁷ ZnO.¹⁸ In addition, nanosized TiO₂ of different phases also has been extensively investigated under high pressure both

experimentally and theoretically.¹⁹⁻²² Among the various structures of TiO₂, anatase and rutile are the most widely studied phases under high pressure due to their promising applications in advanced techniques and rich abundances in nature (structures are shown in Figure 1-1).

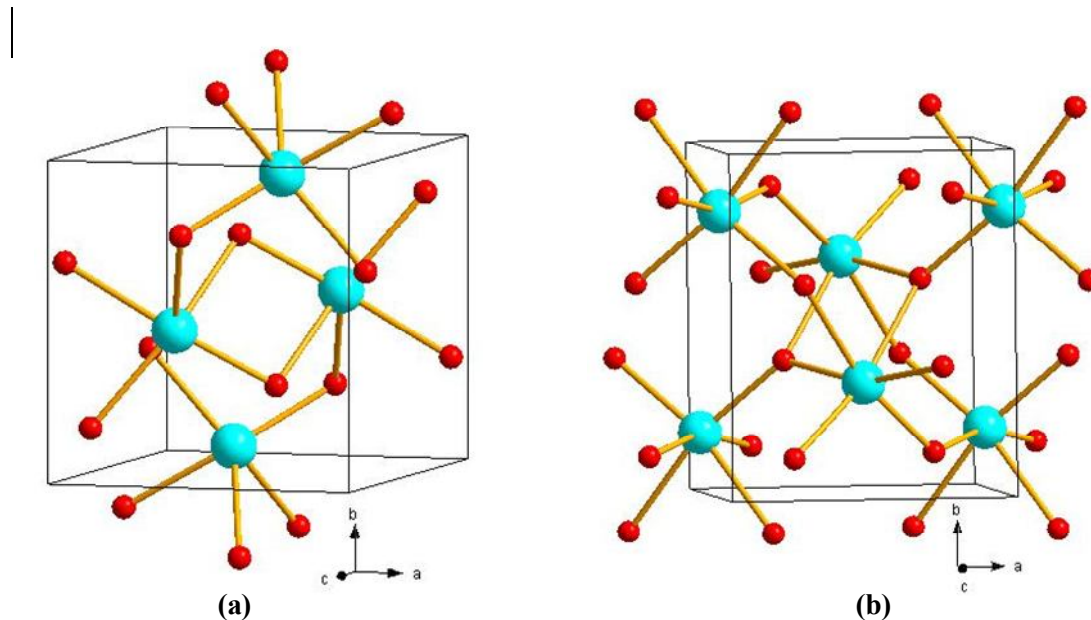


Figure 2-1 Crystal structures of TiO₂. a: baddeleyite phase (space group $P2_1/c$); b: α -PbO₂ phase (space group $Pbcn$). The red and blue balls stand for the O atoms and Ti atoms, respectively.

For high pressure study of anatase TiO₂ nanomaterials, pressure-induced amorphization, phase transition from anatase to baddeleyite phase (crystal structure shown in Figure 2-1 a) and phase transition from anatase to α -PbO₂ phase (crystal structure shown in Figure 2-1 b) are reported in different sizes of nanoparticles. The phase transition sequence varies as size of nanoparticles changes. In addition to phase transition sequence, other high-pressure behaviours such as transition pressures are also dependent upon different morphologies and size. For example, two anatase TiO₂ nanowire samples, with respective diameters of <100 nm and \sim 200 nm were observed to have the same phase transition sequence from anatase to baddeleyite phase but with different respective transition pressure, i.e., 13 GPa and 9 GPa.²³

Compared with anatase phase, the high-pressure behaviors of nanosized TiO₂ in rutile phase is still lack of understanding because no 1D rutile TiO₂ has been studied under high pressure yet. Many outstanding issues, such as phase transition sequence, phase transition pressure, high pressure phases, compressibility, systematic understanding of morphology and size effect, etc, still remain to be addressed. In this work, hydrothermally synthesized 1D rutile TiO₂ nanomaterials, i.e., nanowires, nanorods, flower-like nanorods and nanotubes were studied under high pressure for the first time, using *in situ* Raman spectroscopy and synchrotron X-ray diffraction. Unique high pressure phenomena were observed and comparison study of these 1D rutile TiO₂ nanomaterials shows strongly contrasting morphology-dependent compression behaviours.

2.2 Experimental

2.2.1 Materials synthesis

Nanorods and nanowires: Nanorods and nanowires TiO₂ were prepared by the hydrothermal method similar to that described by Liu²⁴ and Feng.²⁵ Briefly, 10-30 mL of deionized water was mixed with 10-30 mL of concentrated hydrochloric acid (36.5-38.0 % by weight) to reach a total volume of 30 mL in a Teflon-lined stainless steel autoclave (50 mL volume). The mixture was stirred at ambient conditions for 5 min before the addition of 0.5 to 1.0 mL of titanium butoxide (97 % Aldrich) / titanium isopropoxide (97 % Aldrich). After stirring for another 5 to 10 min, two pieces of fluorine doped tin oxide (FTO) coated glass slide substrates (10 Ω / sq) purchased from Aldrich, ultrasonically cleaned for 60 min in a mixed solution of deionized water, acetone, and 2-propanol with volume ratios of 1:1:1, were placed at an angle against the wall of the Teflon-liner. The hydrothermal synthesis was conducted at 80 °C to 180 °C for 6 to 24 h in an oven. Then, the autoclave was directly cooled/step by step to room temperature. The FTO substrate was taken out, rinsed extensively with deionized water and allowed to dry in ambient air. It is well known

that morphology and size of nanomaterials are largely depending on synthesis conditions. By choosing different precursors, changing the volume of precursor, acidity, growth time and temperature, three morphologies of 1D nanostructured TiO₂ were synthesized.

Nanotubes: The TiO₂ nanotubes were synthesized in two steps. First, the growth of flower-like nanorods TiO₂ arrays on FTO glass using a hydrothermal method as mentioned above. According to Huang *et al.*,²⁶ the as-grown TiO₂ nanorods can be converted into nanotubes by hydrothermal etching in HCl. Therefore, in the second step, the flower-like nanorods TiO₂ arrays were immersed in 15 ml 12.0 M HCl without any precursors and post treated at 150 °C for 6 h. Finally, the synthesized sample were rinsed with deionized water and allowed to dry in ambient air to obtain nanotubes TiO₂.

2.2.2 Sample preparation

A symmetrical DAC with two type-I diamonds of 400 µm culets was used for the high-pressure *in-situ* Raman measurements and synchrotron X-ray diffraction experiment. A hole with a diameter of 130 µm was drilled on the centre of the stainless steel gasket and used as a sample chamber. Neon gas was loaded as the PTM for X-ray diffraction measurements whereas no PTM was used for Raman measurements. A few ruby balls were inserted in the hole as pressure calibrant.

2.2.3 Characterization

The morphologies of all 1D nanostructured TiO₂ were examined using scanning electron microscopy (SEM, LEO 1540) at the Nanofabrication Laboratory, University of Western Ontario.

The powder X-ray diffraction facility in the Department of Earth Science was used to examine the crystallinity of the synthesized 1D nanomaterial. The X-ray diffraction

facility has a Rigaku X-ray diffractometer and uses the Co K-radiation as the X-ray source with the wavelength of 1.7889 Å.

In situ high-pressure structural characterization was performed using a customized Raman spectroscopy and synchrotron X-ray diffraction with detailed instrumental information described in Chapter 1. Specifically, A 532 nm wavelength laser was used as the excitation source for Raman spectra. The Raman system was calibrated by neon lines with an uncertainty of $\pm 1 \text{ cm}^{-1}$. Raman data for each pressure point were collected in the spectral region of 100-800 cm^{-1} , corresponding to the lattice vibrations with accumulation time of 180 s. *In situ* angle-dispersive X-ray diffraction measurements were carried out at room temperature at the beamline Sector-20ID of Advanced Photon Source (APS) in Argonne National Laboratory (ANL). The incident wavelength is 0.4769 Å with a beam size of 5 μm (H) x 5 μm (V) focused at the center of the sample. The diffraction data were recorded with an exposure time of 60 s, and the 2D Debye-Scherrer diffraction patterns were integrated by using Fit2D program for further analysis. A Rietveld analysis was performed using the GSAS+EXPGUI program. More details about Fit2D and Rietveld refinement programs are provided in Appendix I.

2.3 Results and discussion

2.3.1 Morphology

2.3.1.1 Nanowires

Figure 2-2 shows SEM images of vertically aligned rutile TiO_2 nanowires that were prepared by hydrothermal method using a solution of 1 mL titanium isopropoxide as precursor and 15 mL HCl, 15 mL deionized H_2O at 150 °C for 16 h. Figure 2-2 (a) is the top view and Figure 2-2 (b) is cross-sectional tilting views. It can be seen that densely aligned TiO_2 nanowires grew uniformly on the FTO substrate after 16 h

hydrothermal reaction. When measured at the tip, TiO₂ nanowires are of an average diameter of 10 nm to 30 nm.

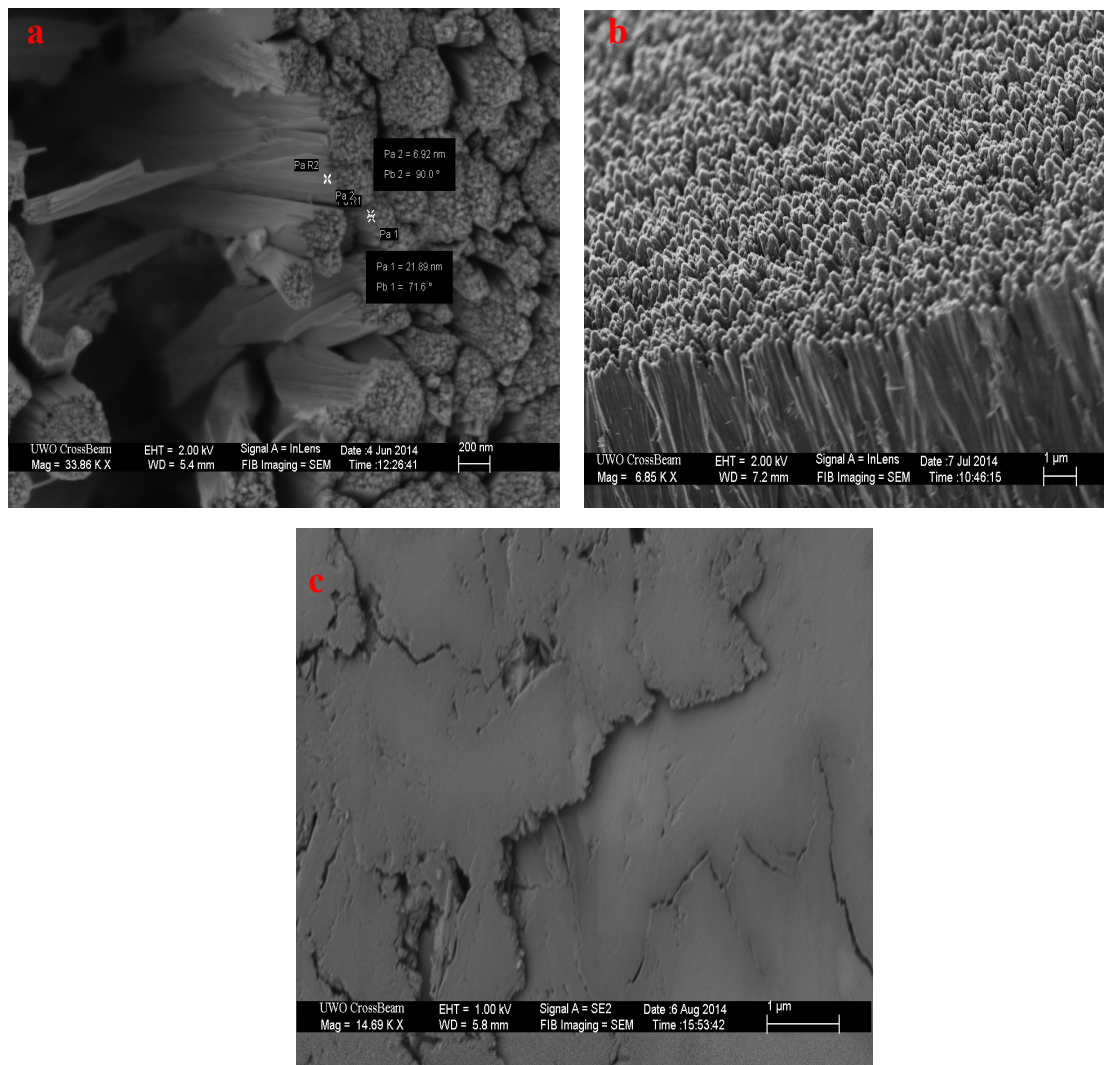


Figure 2-2 SEM images of rutile TiO₂ nanowires in (a) top view; (b) side view and (c) view after compression/decompression in DAC.

2.3.1.2 Nanorods

Figure 2-3 shows SEM images of the nanorod-films grown on FTO substrate at 120 °C for 20 h with 1 mL titanium butoxide as precursor and 15 mL HCl, 15 mL deionized H₂O. The SEM images were taken from top view at different magnifications. Figure 2-3 (b) shows that the top surface of the nanorod appears to contain many step edges, while the side surface is smooth. The nanorods are

tetragonal in shape with square top facets, consistent with the expected growth habit for the tetragonal crystal structure. By measurement, the diameter of the nanorods is mainly from 70 to 110 nm.

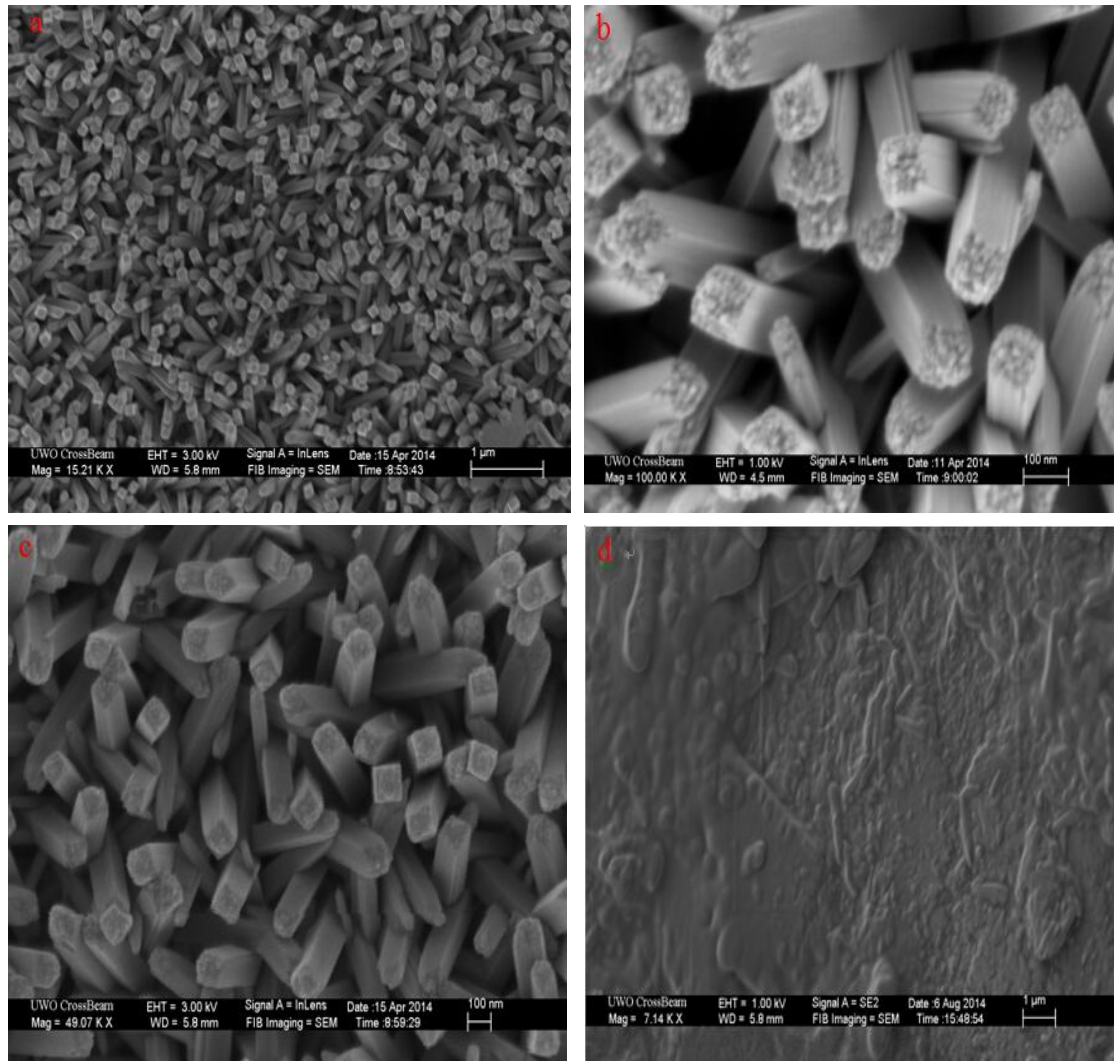


Figure 2-3 SEM images of rutile TiO₂ nanorods in (a) (b) (c) top view and (d) view after compression/decompression cycle in DAC.

2.3.1.3 Flower-like Nanorods

To modify the morphology, effect of acidity and substrates were studied. It is known that, adding HCl to the solution can inhibit fast hydrolysis of precursor and produce even granules.²⁷ In this case, the acidity was increased from 15 mL HCl, 15 mL deionized H₂O to 20 mL HCl, and 10 mL deionized H₂O to get homogeneous

nanorods. For the effect of substrates, experiments to grow TiO₂ nanorods on glass were unsuccessful, indicating that nucleation and growth may require on FTO crystals. In fact, the FTO substrate also has the tetragonal rutile structure, and the lattice mismatch between the tetragonal FTO ($a = b = 0.4687$ nm) and rutile TiO₂ ($a = b = 0.4594$ nm) is 2 %. This small lattice mismatch may promote the epitaxial nucleation and growth of rutile TiO₂ nanorods on FTO.²⁴ Careful adjustment of the volume of precursor, acidity and cooling time, eventually leads to a formation of interesting flower-like nanorods morphology.

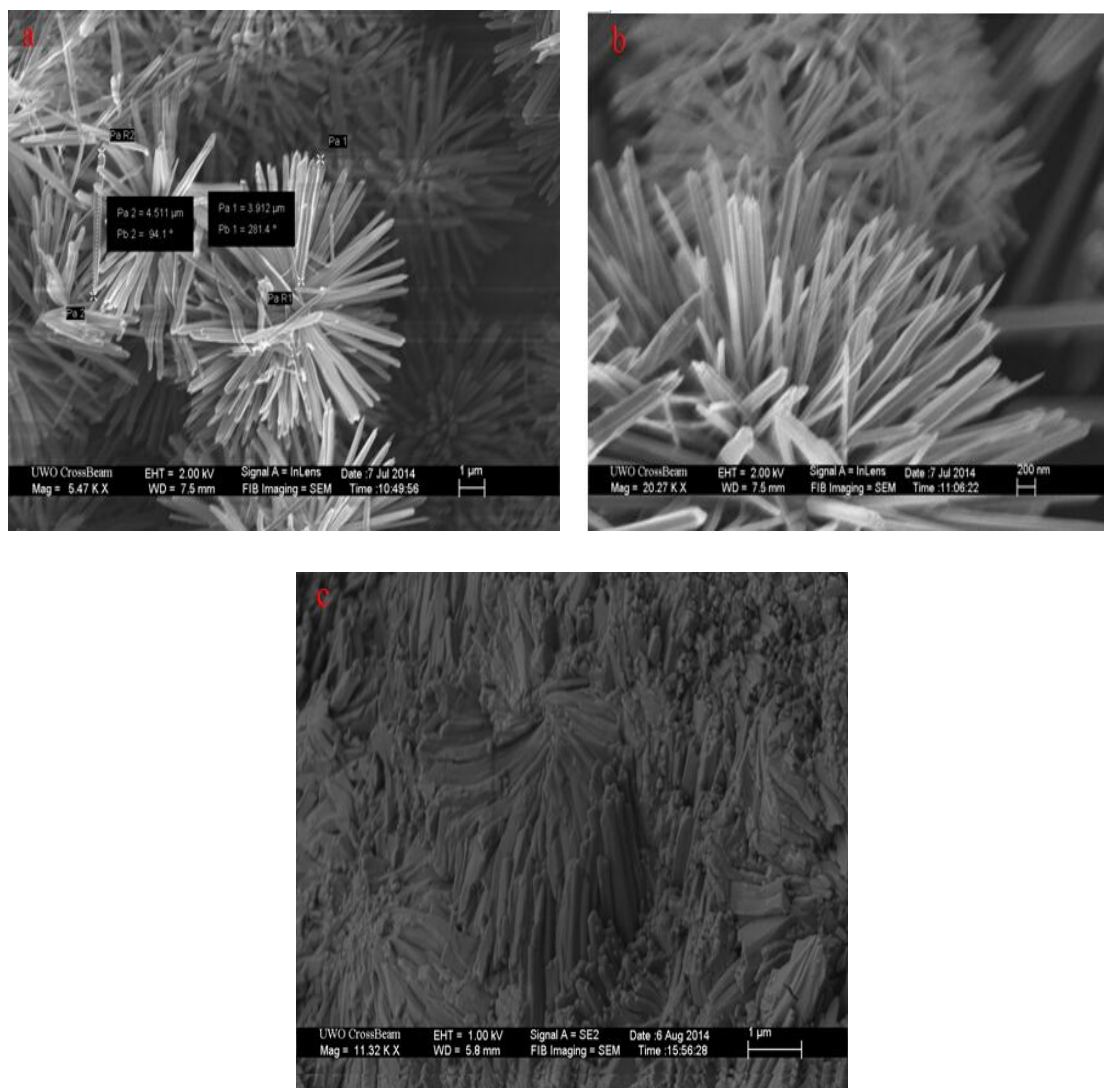


Figure 2-4 SEM images of rutile TiO₂ flower-like nanorods in (a) (b) top view (c) view after compression/decompression in DAC

Three SEM images of synthesized rutile TiO_2 flower-like nanorods are shown in Figure 2-4. Specifically, these flower-like nanorods were grown at $150\text{ }^\circ\text{C}$ for 16 h with 0.8 mL titanium isopropoxide as precursor and 20 mL HCl, 10 mL deionized H_2O , followed by with decreasing the temperature step by step ($50\text{ }^\circ\text{C} / 4\text{ h}$) after synthesis. Top view of SEM images of rutile TiO_2 nanorods at different magnifications are provided in Figure 2-4 (a) (b). Comparing with the first nanorods in Figure 2-3, this morphology seems not to grow perpendicular to the FTO surface and is more separate between each nanorod. To the best of our knowledge, this morphology was obtained for the first time using the FTO based hydrothermal method. The average length of these nanorods is $\sim 5\text{ }\mu\text{m}$ and the diameter is $\sim 100\text{ nm}$.

2.3.1.4 Nanotubes

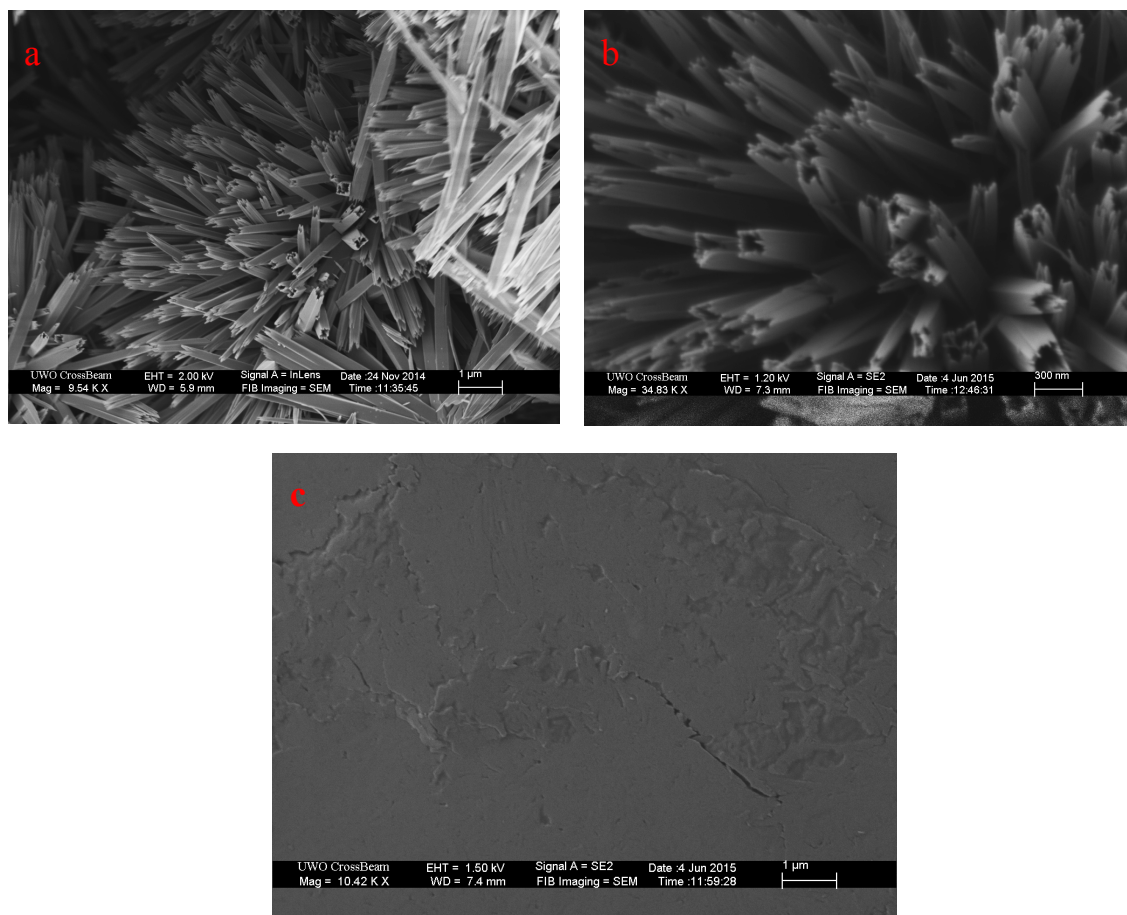


Figure 2-5 SEM images of rutile TiO_2 nanotubes in (a) (b) top view (c) view after compression/decompression in DAC

Rutile TiO₂ nanotubes with SEM images shown in Figure 2-5 are synthesized by etching as-grown TiO₂ flower-like nanorods in the HCl hydrothermal solution again without adding any Ti precursor. Top view of SEM images of rutile TiO₂ nanotubes at different magnifications are provided in Figure 2-5 (a) (b). After etching in 12.0 M HCl at 150 °C for 6 h, it was interesting to observe that the solid TiO₂ flower-like nanorods (Figure 2-4) were converted into hollow nanotubes which indicates a different etching rate of the growing front along the [0 0 1] direction and that of the side wall of (1 1 0) facets.²⁸ The hydrothermal routes employed in this study directly yield highly crystalline well-aligned TiO₂ nanotubes without post high temperature annealing. To better characterize this nanotubes morphology, TEM study is needed in the future.

2.3.2 XRD characterization

In Figure 2-6, XRD results of four morphologies show that these nanostructures deposited on FTO substrate are of high crystallinity with sharp Bragg reflections. All the diffraction peaks agree well with the tetragonal rutile phase (space group, $P4_2/mnm$; JCPDS No.21-1276, $a = b = 0.4593$ nm and $c = 0.2959$ nm). No other diffraction peaks of other phases such as anatase and brookite were observed. For both nanorods and nanowires, compared to the standard powder diffraction pattern, the (0 0 2) diffraction peak at 74.4° was significantly enhanced, which indicates that these two morphologies are highly oriented with respect to the substrate surface. More diffraction peaks were observed in flower-like nanorods XRD data than those obtained for nanorods and nanowires. This may be because of the programmed temperature reduction that enhanced the degree of crystalline. Comparing with nanowires and nanorods, the biggest difference is the intensity of (0 0 2) peak, which is much lower than the first two. Combined with SEM results in Figure 2-4, it is possible that, even though this morphology is growing on the FTO substrate, the directions are not mainly along the [0 0 1]. Instead, the nanorods can nucleate and grow at an angle to the substrate surface, likely because the FTO is polycrystalline

and its surface is rough.²⁴ After etching, the nanotubes show similar XRD pattern to flower-like nanorods. However, the intensity of (0 0 2) diffraction peak is stronger than flower-like nanorods, suggesting a preferred grow orientation of nanotubes.

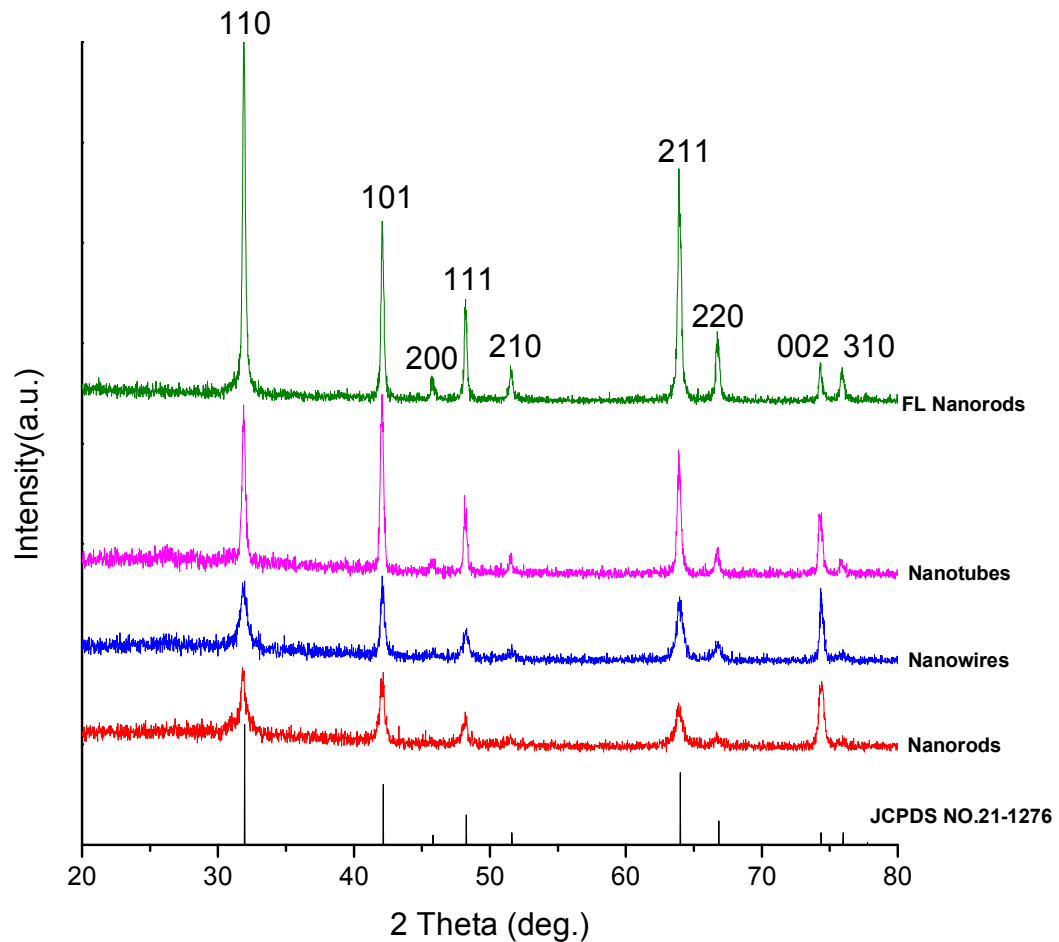


Figure 2-6 X-ray diffraction patterns from rutile TiO₂ nanorods, nanowires, flower-like nanorods and nanotubes. Vertical bars at the bottom denote the standard diffraction data of rutile TiO₂.

2.3.3 Raman results of 1D nanostructured TiO₂ upon compression and decompression

2.3.3.1 Nanowires

Selected Raman spectra of TiO₂ nanowires collected upon compression to the pressure of 35.5 GPa and its corresponding decompression were shown in Figure 2-7. It is well established that rutile phase of TiO₂ has five Raman active modes, which are at 143 cm⁻¹ (*B*_{1g}), 237 cm⁻¹ (two-phonon scattering), 447 cm⁻¹ (*E*_g), 612 cm⁻¹ (*A*_{1g}) and 826 (*B*_{2g}) cm⁻¹.²⁹ In our experiment, three Raman peaks are observed at 462 cm⁻¹, 620 cm⁻¹ and 246 cm⁻¹ at ambient condition as shown in Figure 2-7. These Raman bands at 246, 462 and 620 cm⁻¹ can be ascribed to the two-phonon scattering, *E*_g and *A*_{1g} modes of the rutile phase, respectively.²² The missing of *B*_{1g} and *B*_{2g} modes of the rutile phase in our case may be due to their weak intensity. Obviously, the two Raman bands of *E*_g (462 cm⁻¹) and *A*_{1g} (620 cm⁻¹) show a significant broadening and blue shift (shown Figure 2-11) upon compression which can be attributed to both size and residual stress effects. A new peak at 268.5 cm⁻¹ can be observed when the pressure reaches ~23.7 GPa, indicating the onset of phase transition to baddeleyite phase.³⁰ With increasing pressure, *E*_g and *A*_{1g} Raman bands become weaker and up to 35.5 GPa, the peak associated with baddeleyite phase also become substantially broadened. This indicates that the baddeleyite phase under a high pressure of 35.5 GPa is a low ordered structure.

The reversibility of pressure effect on crystal structures provides important information on transformation mechanism. Therefore, after compressed to 35.5 GPa, Raman measurements of nanowires were also conducted upon decompression. In general, the intensities of these Raman bands of the baddeleyite phase increased gradually as the pressure were released (Figure 2-7). When the pressure is released to ~5.2 GPa, new Raman bands (190 cm⁻¹, 303 cm⁻¹ and 378 cm⁻¹) of α-PbO₂ phase appears,²² indicating a phase transition from baddeleyite to α-PbO₂ phase occurs. The

intensities of α -PbO₂ phase Raman bands increased significantly when the pressure was released to ambient pressure. It is evident that the α -PbO₂ phase remains stable at ambient pressure.

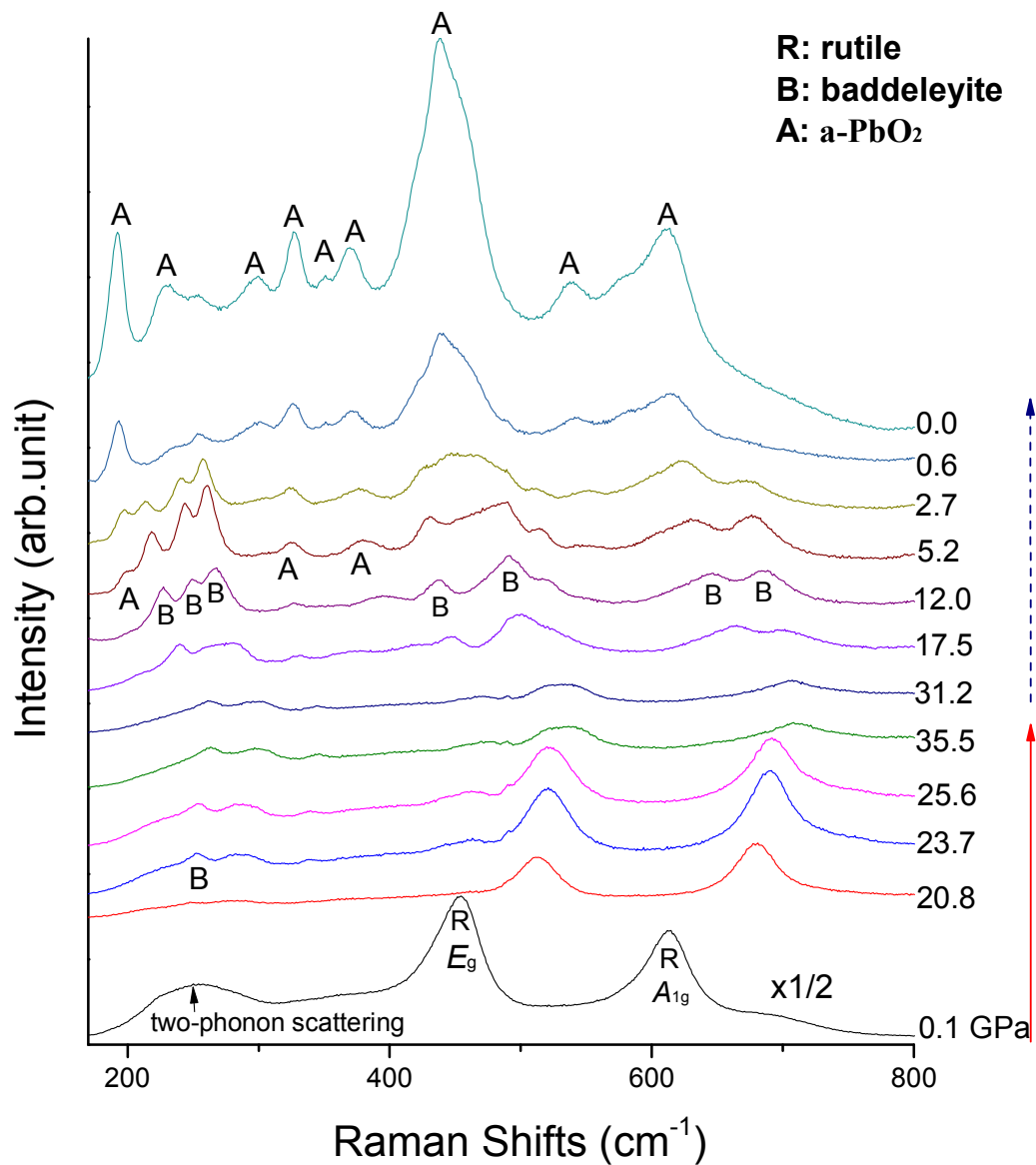


Figure 2-7 Selected Raman spectra of rutile TiO₂ nanowires collected upon compression and decompression. The red and blue arrows indicate the compression and decompression sequence, respectively.

2.3.3.2 Nanorods

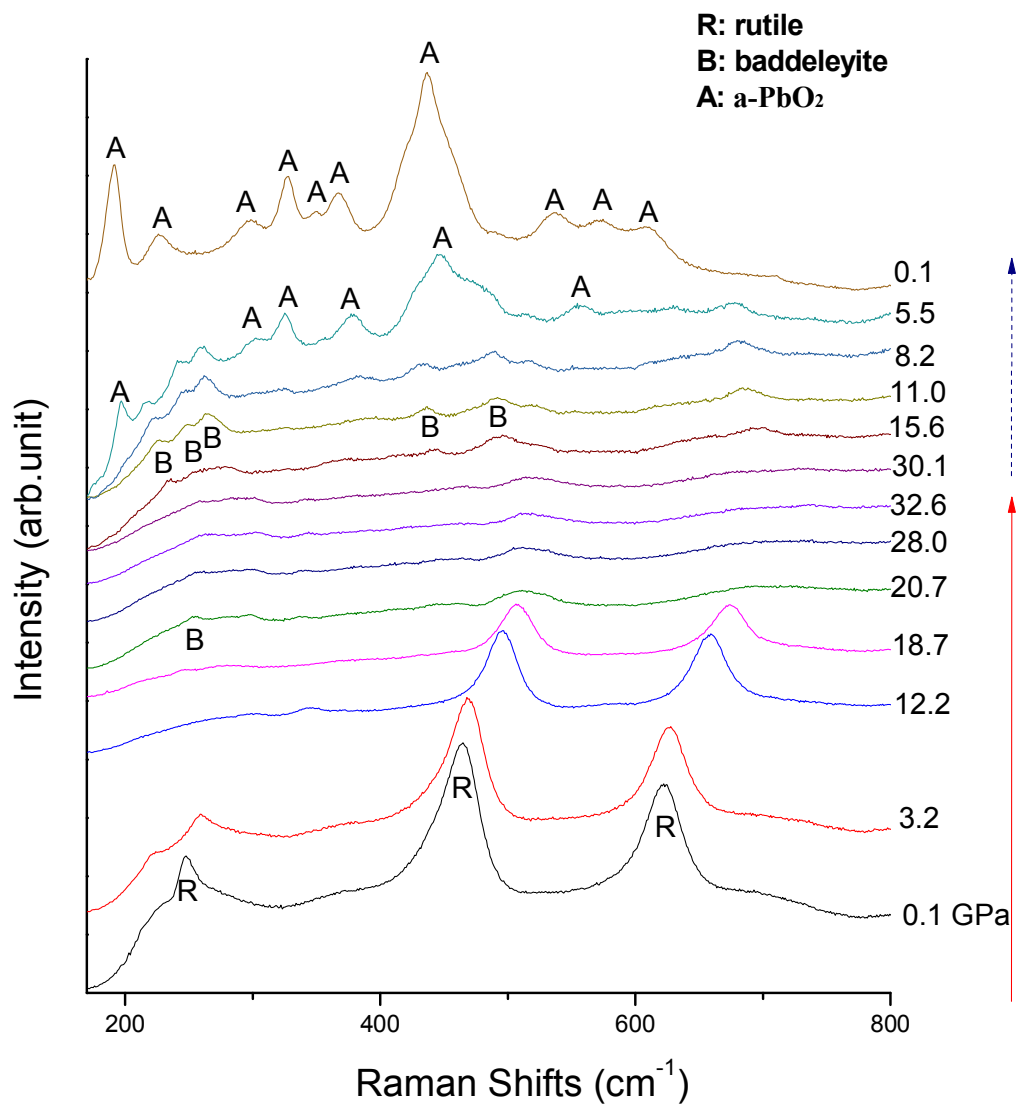


Figure 2-8 Selected Raman spectra of rutile TiO_2 nanorods collected upon compression and decompression. The red and blue arrows indicate the compression and decompression sequence, respectively.

Figure 2-8 shows the selected Raman spectra of the rutile TiO_2 nanorods measured during compression and decompression. All the Raman peaks show blue shift under high pressure (Figure 2-11). At ~ 20.7 GPa, the onset of a phase transition from rutile to baddeleyite structure were observed by the appearance of a new peak at 253.5 cm^{-1} which is associated with the baddeleyite phase. At 32.6 GPa, the low intensity

and broaden profile of the baddeleyite peaks indicating a low ordered structure of baddeleyite phase. Upon releasing pressure, the baddeleyite phase gradually transforms into the α -PbO₂ phase below 8 GPa, and retained to ambient condition, suggesting that the α -PbO₂ phase is stable at ambient conditions. The phase transition sequence of nanorods was found to be the same as nanowires: rutile to baddeleyite phase upon compression and baddeleyite to α -PbO₂ phase upon decompression, but the onset transition pressure of nanowires is higher than nanorods.

2.3.3.3 Flower-like nanorods

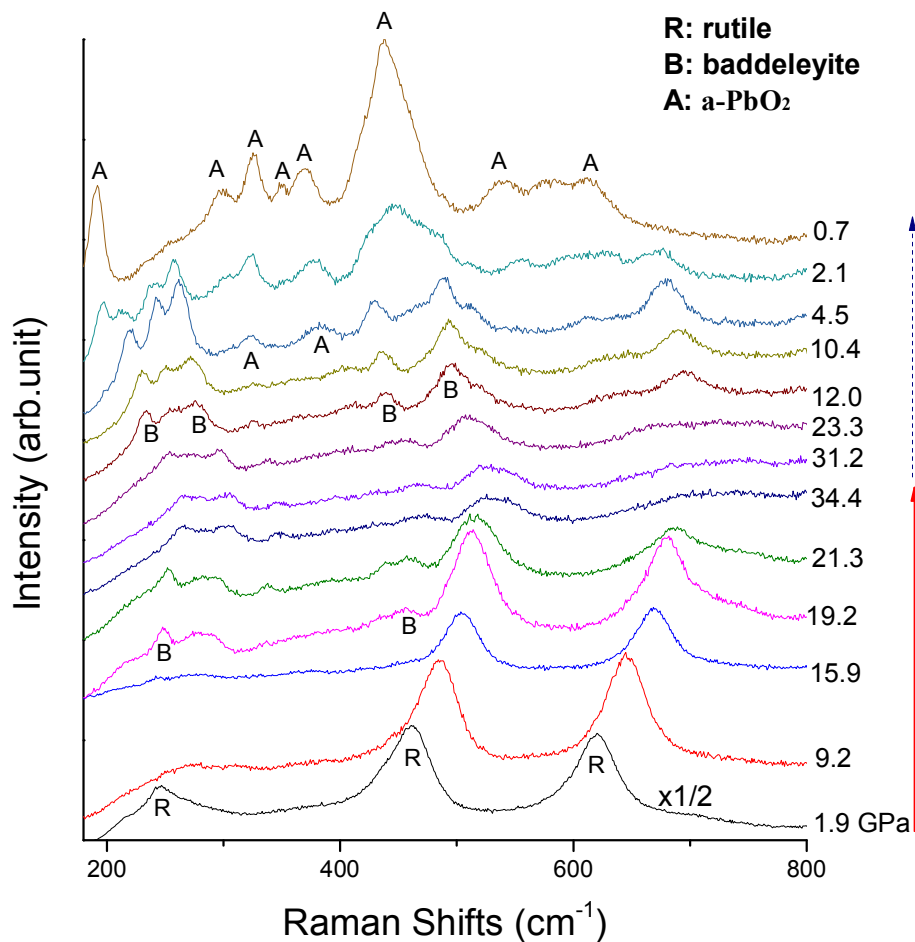


Figure 2-9 Selected Raman spectra of flower-like TiO₂ nanorods collected upon compression and decompression. The red and blue arrows indicate the compression and decompression sequence, respectively.

Selected Raman spectra of flower-like nanorods TiO_2 collected upon compression and decompression are depicted in Figure 2-9. Upon compression, all the Raman modes of rutile phase shifted to higher frequencies (figure 2-11). New peaks of baddeleyite were first observed at ~ 19.2 GPa (243 cm^{-1} and 461 cm^{-1}). Initially the intensities of these baddeleyite peaks increase with increasing pressure below 21.3 GPa, and then decrease with further compressing to the pressure of 34.4 GPa. During decompression, the phase transition from baddeleyite to $\alpha\text{-PbO}_2$ phase starts at ~ 4.5 GPa. The retrieved phase at ambient condition was found in $\alpha\text{-PbO}_2$ phase. Compared to the TiO_2 nanorods and nanowires mentioned above, the flower like nanorods have the same phase transition sequence but at lower transition pressure.

2.3.3.4 Nanotubes

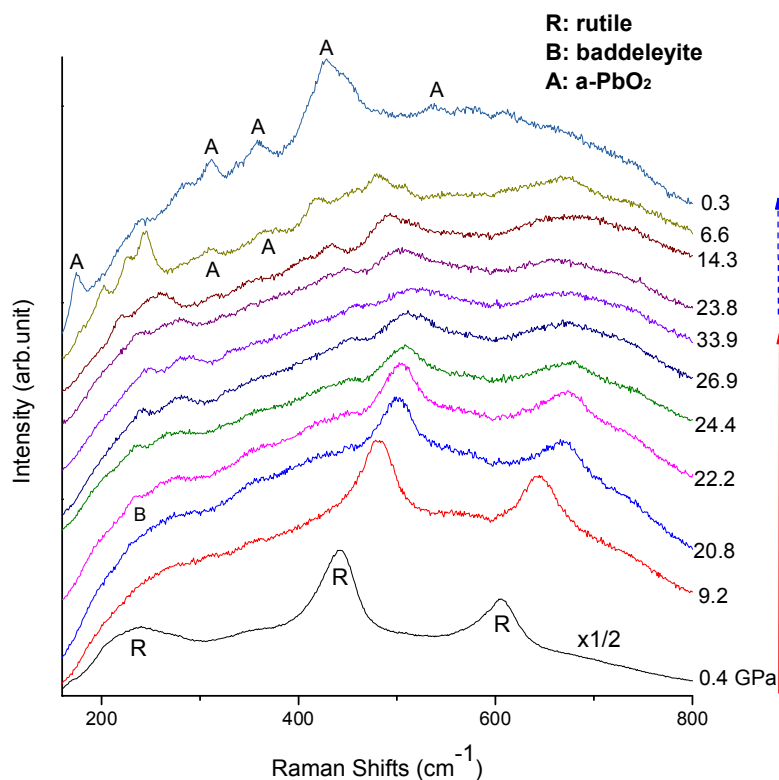


Figure 2-10 Selected Raman spectra of TiO_2 nanotubes collected upon compression and decompression. The red and blue arrows indicate the compression and decompression sequence, respectively.

Figure 2-10 shows the selected Raman spectra of nanotubes collected upon compression up to 33.9 GPa. Upon compression, all the Raman modes shifted to higher frequencies (see Figure 2-11). The rutile phase persisted to 20.8 GPa indicated by the consistent assignment of all the characteristic Raman modes of the rutile phase. At ~ 22.2 GPa, a new Raman peak at 239 cm^{-1} was observed, denoting the onset of a phase transition from rutile to baddeleyite structure. At 33.9 GPa, the Raman profile was significantly broadened but characteristic Raman peaks of baddeleyite phase can still be identified, which suggested pressure-induced disorder occurred instead of pressure-induced amorphization. When pressure was released to ~ 6.6 GPa, the appearance of new peaks at 310 and 380 cm^{-1} indicated a phase transition from baddeleyite to $\alpha\text{-PbO}_2$ phase occurred. This new phase was retained to ambient condition, suggesting that the $\alpha\text{-PbO}_2$ phase is stable at ambient condition.

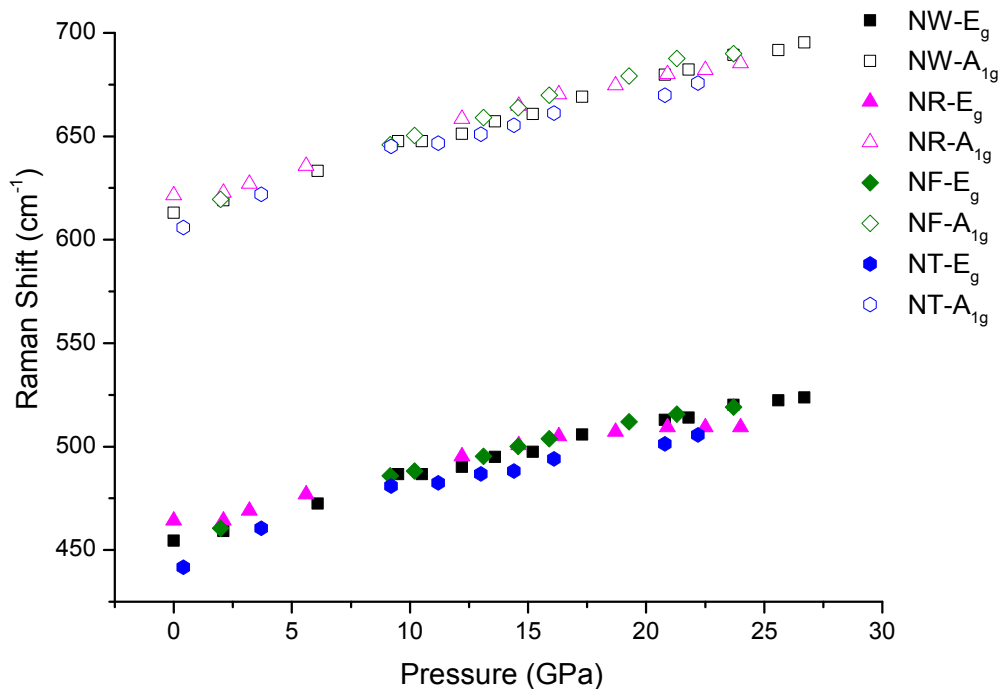


Figure 2-11 Pressure dependence of Raman active modes (E_g and A_{1g}) of nanowires (NW), nanorods (NR), flower-like nanorods (NF) and nanotubes (NT) TiO_2 upon compression.

2.3.4 Synchrotron XRD results of 1D nanostructured TiO₂ upon compression and decompression

2.3.4.1 Nanowires

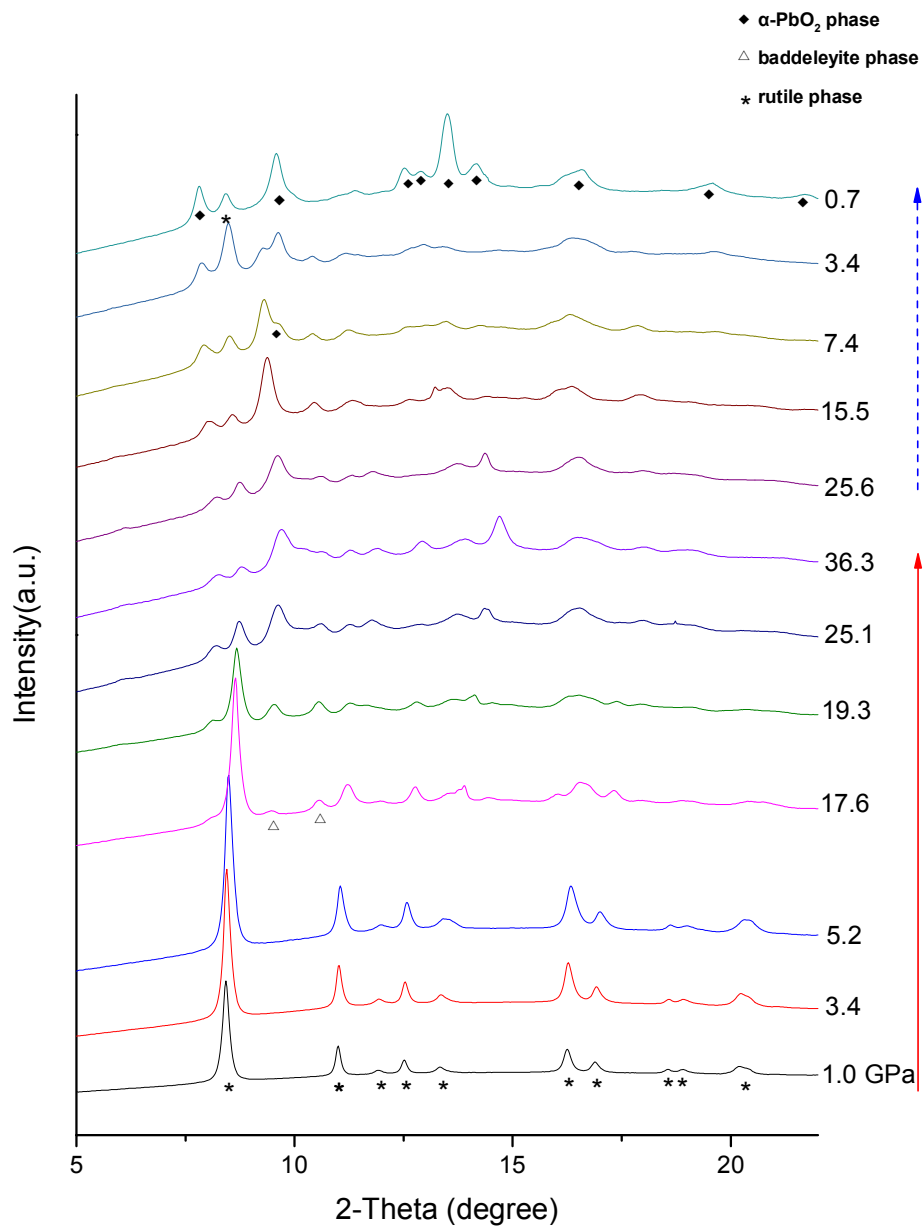
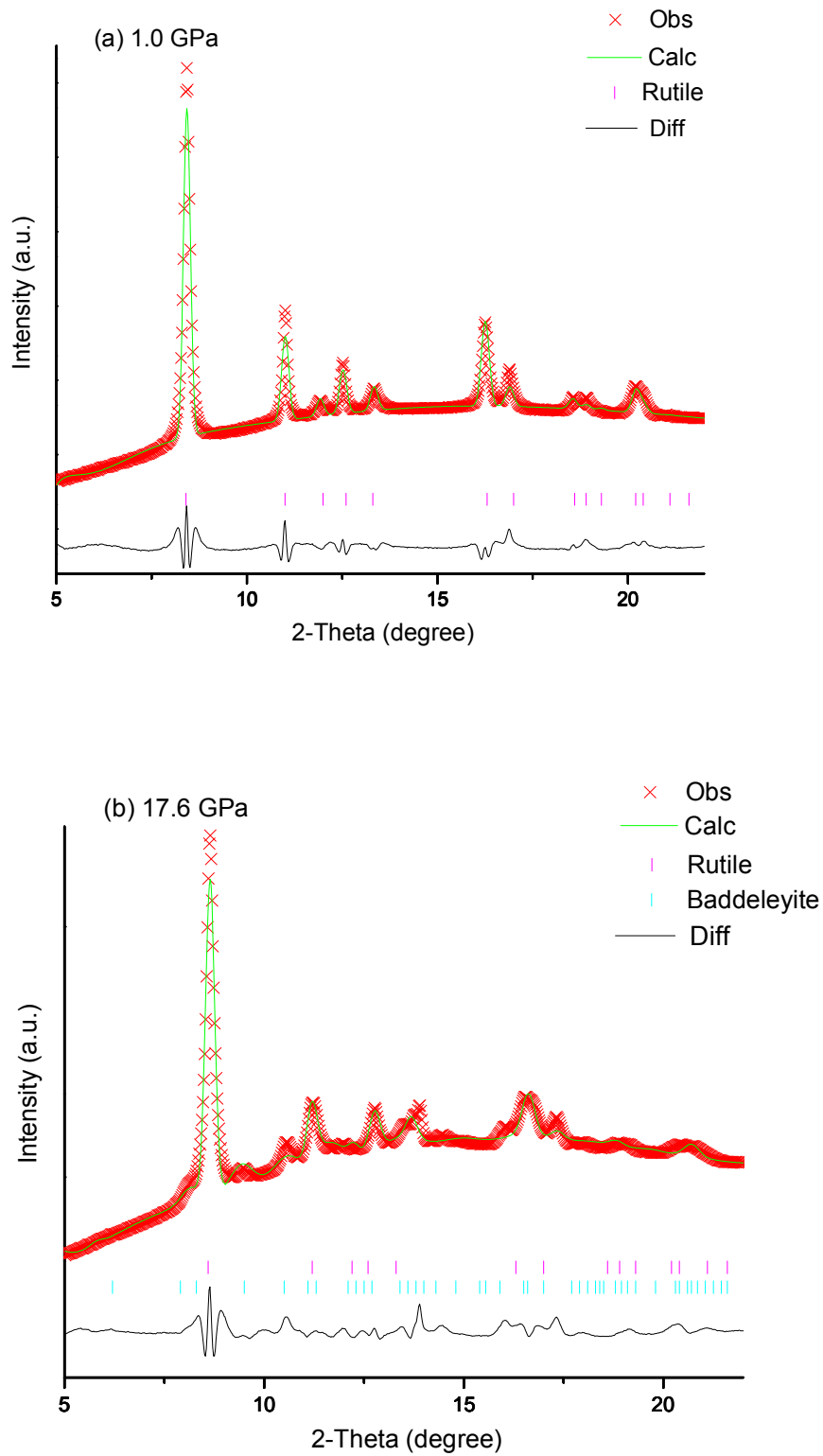


Figure 2-12 Selected X-ray diffraction patterns for TiO₂ nanowires upon compression and decompression. The red and blue arrows indicate the compression and decompression sequence, respectively.

The pressure evolution of the selected *in-situ* high-pressure XRD patterns for rutile TiO₂ nanowires up to 36.3 GPa is shown in Figure 2-12. All reflections at the near ambient pressure can be indexed to the pure rutile phase. By using Rietveld refinement (Figure 2-13 a), unit cell parameters of $a = b = 4.5894 \text{ \AA}$, $c = 2.9574 \text{ \AA}$ were obtained, close to the values observed for bulk rutile TiO₂ (JCPDS file 21-1276). As seen in Figure 2-12, all the reflections of rutile TiO₂ shifted to higher 2θ angle with increasing pressure, indicating a pressure-induced reduction of d -spacing or shrinkage of unit cells. When the pressure was increased to ~ 17.6 GPa, two reflections appeared at 9.41° and 10.59° which can be indexing with (1 1 -1) and (1 1 1) for the baddeleyite phase (Figure 2-13 b), indicating the onset of transition from rutile phase into baddeleyite phase. Such phase transition pressure is lower than that observed in the Raman result at 23.7 GPa. This difference may be due to the use of PTM that maintain the system in hydrostatic condition in XRD experiment. The intensity of these two peaks, especially the (1 1 -1) peak increased substantially upon compression, suggesting the progression of the phase transition. As the pressure exceeded 19.3 GPa, the reflections corresponding to rutile phase were weakened significantly. However, the first reflection of rutile phase was still observed at the highest pressure indicating a coexistence of rutile and baddeleyite phase at 36.3 GPa. Rietveld refinement result (Figure 2-13 c) shows the cell parameters of baddeleyite phase is $a = 4.7092 \text{ \AA}$, $b = 4.5961 \text{ \AA}$, $c = 4.8549 \text{ \AA}$, close to the value that reported before,³¹ and rutile phase at this pressure only has a low abundance of $\sim 17\%$. Upon decompression, all the reflections shifted to lower 2θ angle with decreasing pressure, indicating expanding of the unit cells. When the pressure was decreased from 36.3 GPa to ~ 7.4 GPa, a new reflection appeared at 9.63° , which suggests that baddeleyite phase began to transform into a new phase. By using Rietveld refinement (Figure 2-13 d), all reflections except the first one at near ambient condition can be indexed to the α -PbO₂ phase with the cell parameters of $a = 4.5267 \text{ \AA}$, $b = 5.5091 \text{ \AA}$, $c = 4.9726 \text{ \AA}$, which is consistent with previous work,³² suggesting a complete phase transition from baddeleyite to α -PbO₂ phase. Interestingly, the (1 1 0) reflection of rutile phase was observed in all patterns upon compression and decompression,

suggesting a unique phase transition phenomenon unprecedented in TiO_2 nanomaterials. Refinements of XRD patterns at other pressures are shown in Appendix II.



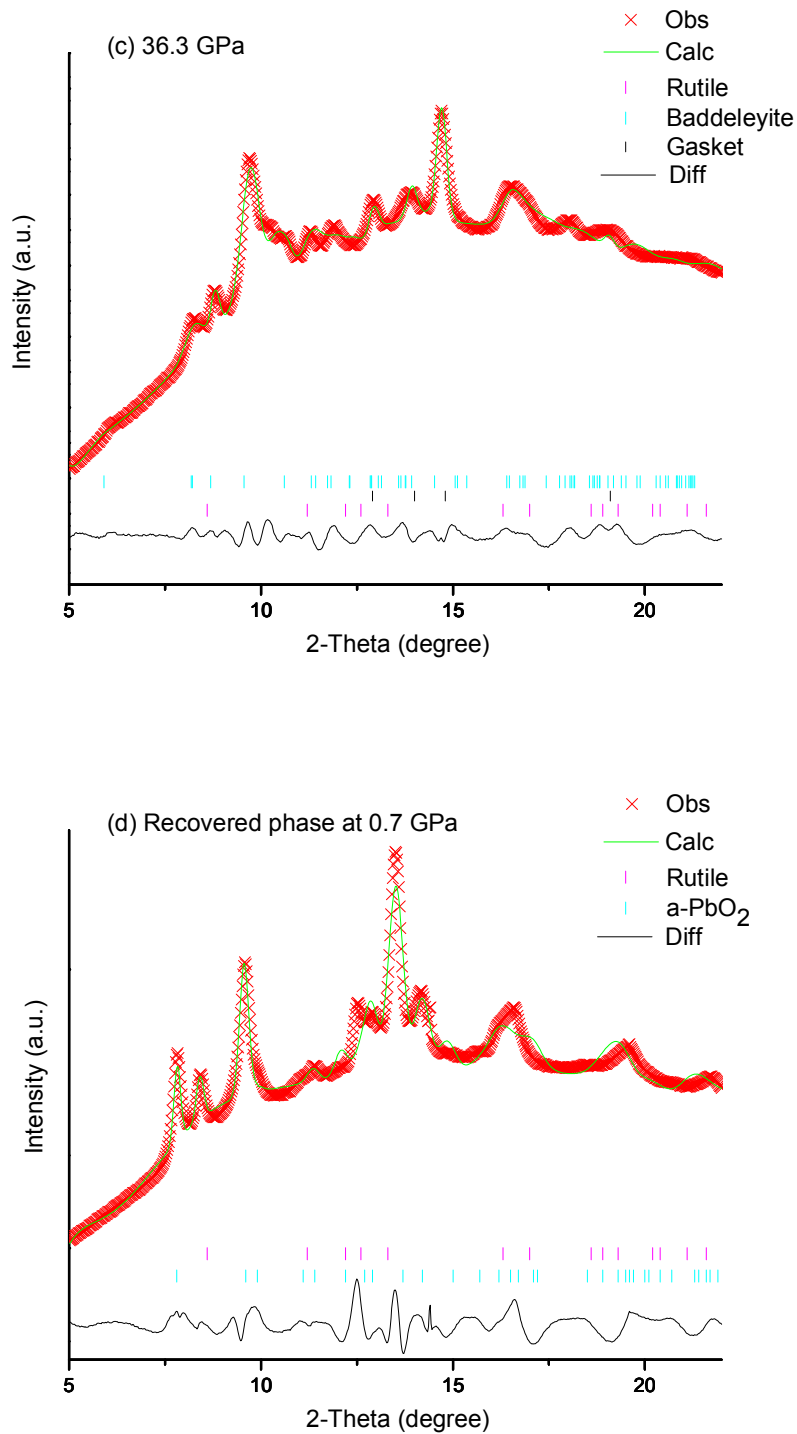


Figure 2-13 Rietveld refinement of XRD patterns of TiO₂ nanowires at 1.0 GPa (a), at 17.6 GPa (b), at 36.3 GPa (c) upon compression, and at 0.7 GPa (d) upon decompression. The red cross is experimental X-ray intensity, whereas the green solid line is the calculated diffraction pattern based on refinement with the black curve at the bottom showing the difference between the calculated and observed intensities. The vertical bars with different colors indicate the characteristic reflections of different phases.

2.3.4.2 Flower-like nanorods

In situ high-pressure X-ray diffraction measurements were performed on flower-like nanorods upon compression up to 34.9 GPa. Representative diffraction patterns were depicted in Figure 2-14. By using Rietveld refinement (Appendix II), the unit cell parameters for rutile phase were obtained as $a = b = 4.5909 \text{ \AA}$, $c = 2.9581 \text{ \AA}$, consistent with the previous diffraction measurement of bulk rutile TiO_2 (JCPDS file 21-1276). When the pressure was increased to $\sim 18.3 \text{ GPa}$ (Figure 2-15 a), two reflections, i.e. (1 1 -1) and (1 1 1), associated with the baddeleyite phase were observed, suggesting the onset of transition from rutile to baddeleyite phase which is well agree with our Raman results of $\sim 19.2 \text{ GPa}$. At the highest pressure of 34.9 GPa, the baddeleyite phase became the main phase as almost all the reflections were indexed with baddeleyite structure. By using Rietveld refinement (see Appendix II), reflections of the baddeleyite phase are discernible, suggesting the sample was still in a crystalline phase instead of an amorphous phase at 34.9 GPa. Upon decompression, when the pressure was released to $\sim 8.7 \text{ GPa}$, two new reflections of 7.85° and 9.64° appeared, indicating a phase transition from baddeleyite to $\alpha\text{-PbO}_2$ phase and this phase is stable at ambient condition with cell parameters of $a = 4.5246 \text{ \AA}$, $b = 5.5038 \text{ \AA}$, $c = 4.9261 \text{ \AA}$ obtained from Rietveld refinement (Figure 2-15 b). Refinements of diffraction patterns of flower-like TiO_2 nanorods at other pressures are also shown in Appendix II.

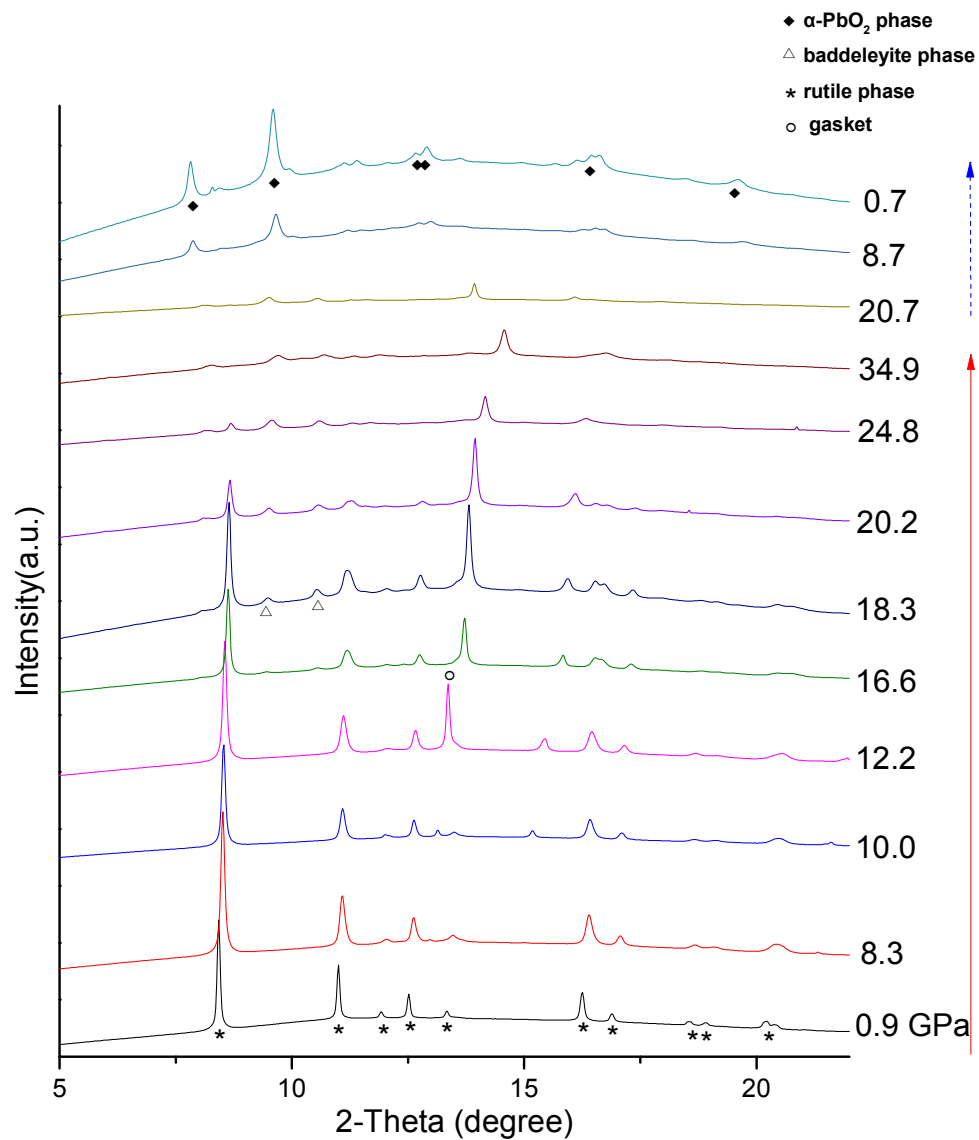


Figure 2-14 Selected X-ray diffraction patterns for TiO₂ flower-like nanorods upon compression and decompression. The red and blue arrows indicate the compression and decompression sequence, respectively.

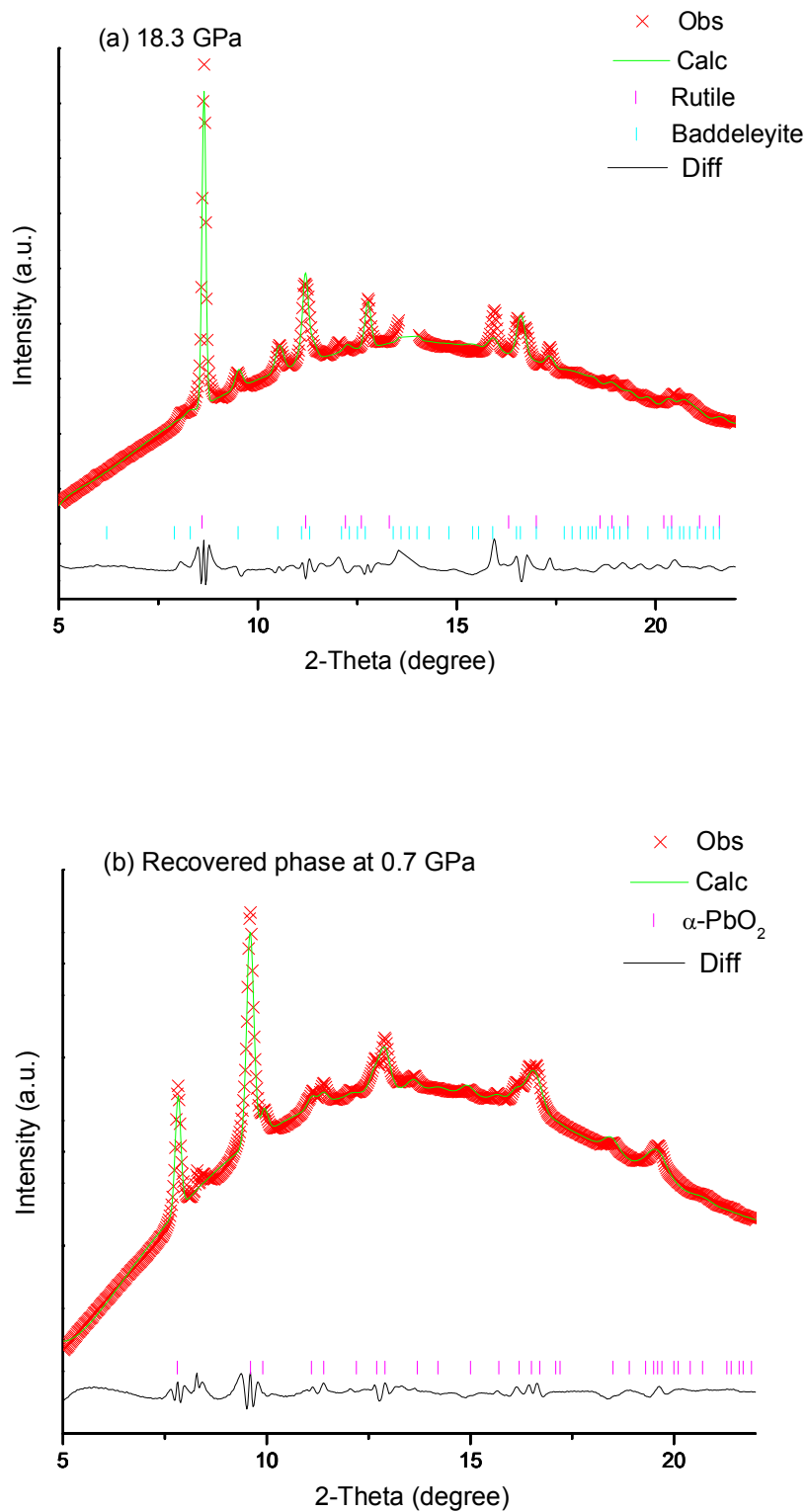


Figure 2-15 Rietveld refinement of XRD patterns of flower-like nanorods at 18.3 GPa (a) upon compression, at 0.7 GPa (b) upon decompression. The legends are the same as Figure 2-13.

2.3.4.3 Nanotubes

X-ray diffraction measurements were performed on rutile TiO₂ nanotubes on compression up to 35.0 GPa followed by decompression. The selected X-ray patterns are depicted in Figure 2-16. All diffraction reflections at near ambient pressure can be indexed to the pure rutile phase with lattice constants of $a = b = 4.5822 \text{ \AA}$ and $c = 2.9554 \text{ \AA}$ (Appendix II). Upon compression, the rutile phase was found to persist to 18.2 GPa, as indicated by the consistent indexing of all associated reflections. At ~ 20.8 GPa, two new reflections appeared at 9.51° and 10.52° , indicating the start phase transition from rutile to baddeleyite phase (Figure 2-17 a) which is consistent with Raman results of ~ 22.2 GPa. This onset phase transition pressure is higher than that of nanowires and flower-like nanorods (Table 2-1). Then the rutile and baddeleyite phase coexisted when compressed, even to 24.3 GPa. The Rietveld analysis (Appendix II) indicates that at this pressure, the initial rutile phase still has a significant abundance of $\sim 37\%$. Upon further compression, the rutile to baddeleyite phase transition was completed at 28.6 GPa, as suggested by the disappearance of all diffraction reflections associated with the rutile phase in the Rietveld analysis. This baddeleyite phase was found to maintain at the highest pressure of 35.0 GPa with cell parameters of $a = 4.5337 \text{ \AA}$, $b = 4.9351 \text{ \AA}$ and $c = 4.6586 \text{ \AA}$. Another phase transformation was observed during decompression. Upon releasing the pressure lower than 9.7 GPa, Rietveld analysis shows a phase transition from baddeleyite to α -PbO₂ and this phase is stable at ambient condition with cell parameters of $a = 4.5373 \text{ \AA}$, $b = 5.5043 \text{ \AA}$, $c = 4.9331 \text{ \AA}$ (Figure 2-17 b). Refinements of diffraction patterns of flower-like TiO₂ nanorods at other pressures are also shown in Appendix II.

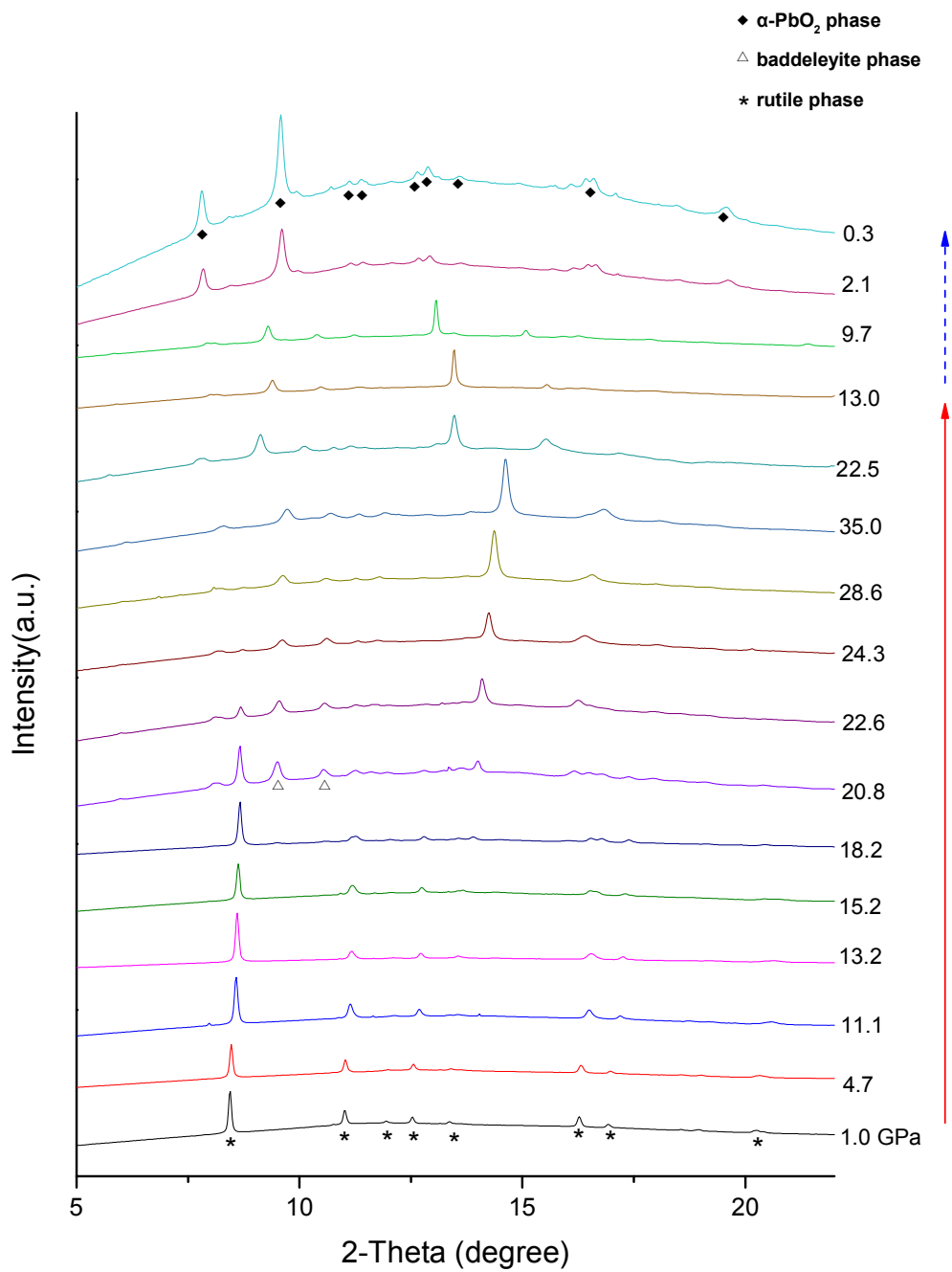


Figure 2-16 Selected X-ray diffraction patterns for TiO₂ nanotubes upon compression and decompression. The red and blue arrows indicate the compression and decompression sequence, respectively.

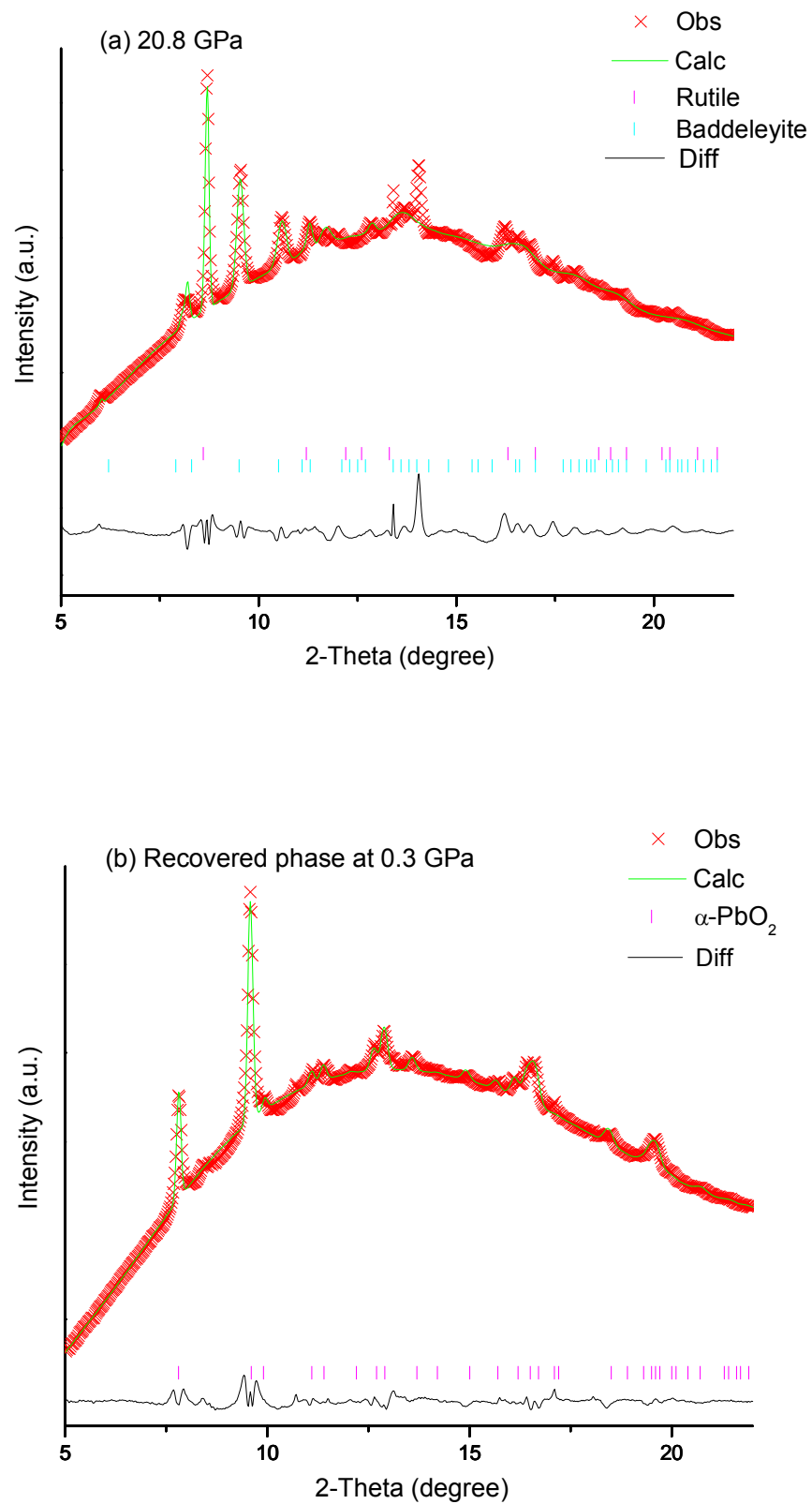


Figure 2-17 Rietveld refinement of XRD patterns at 20.8 GPa (a) upon compression, at 0.3 GPa (b) upon decompression. The legends are the same as Figure 2-13.

2.3.5 Discussion

Extensive high pressure studies on anatase TiO₂ have been reported before. In particular, three phase transition regimes were reported for anatase TiO₂ as a starting material: (1) pressure-induced amorphization at 24 GPa in <10 nm nanoparticles;^{19,31} (2) phase transition from anatase to baddeleyite phase at 16.4 GPa in 12–50 nm nanoparticles;³³ and (3) phase transition from anatase to α -PbO₂ and then to baddeleyite phase in >50 nm coarser crystallites.^{30,34} These results have indicated that the high surface energy of the TiO₂ nanoparticles not only enhanced their phase transition pressure but also can change their phase transition sequences. However, the high-pressure behaviors of 1D TiO₂ nanomaterials do not follow the size-effects model. For instance, in high-pressure study of anatase TiO₂ nanowires with two different diameters, 50-100 nm and 150-200 nm, anatase transformed directly into the baddeleyite phase without going through the α -PbO₂ phase.²³ The same phase transition results were also observed in the high-pressure study of anatase TiO₂ nanotubes by Zhao with the size larger than 50 nm.³⁵ These studies indicated that morphology and size play an important role in the high-pressure behaviours of the anatase TiO₂ nanomaterials.

Different phase transition sequences were reported for bulk rutile TiO₂. For example, the early high-pressure study of bulk rutile TiO₂ showed a rutile to α -PbO₂ phase transition at 10 GPa and then the α -PbO₂ phase transform to baddeleyite phase at 15 GPa using Raman spectroscopy.³⁶ Later, Gerward *et al.* reported a directly transition from rutile to baddeleyite phase at 12 GPa by X-ray diffraction measurement.³⁷ However, the phase transition sequences of rutile nanostructured TiO₂ have been reported to be similar to these of 1D anatase TiO₂ with various transition pressures. For instance, Olsen *et al.* reported the rutile to baddeleyite phase transition was observed at \sim 20 GPa in TiO₂ nanoparticles.³⁸ In addition, the nanoporous TiO₂ material was also found to exhibit a rutile to baddeleyite phase transition at the pressure \sim 10.8 GPa.²² The onset phase transition pressure is lower than that of rutile

nanoparticles (~ 20 GPa) and that of bulk rutile TiO_2 (~ 12 GPa).³⁷ The high pressure studies of rutile TiO_2 in different morphologies and sizes are summarized in Table 2-1. Compare to the bulk materials, nanosized rutile TiO_2 has a higher ratio of surface energy to volume.²¹ Therefore, the onset pressure for phase transition of rutile to baddeleyite for nanoparticles (~ 20 GPa) is higher than that for the bulk material (~ 12.0 GPa). However, a lower phase transition pressure from rutile to baddeleyite was observed in nanoporous materials with 10.8 GPa. This reduction of transition pressure in rutile nanomaterials was explained by a large volume collapse upon phase transition.²² In general, the variations of transition pressure were believed to be the result of the competition between the volume collapse and surface energy difference that contributed predominantly to the change of total free energy.¹⁸ In this work, the phase transition sequences of three 1D (nanowires, flower-like nanorods, nanotubes) rutile TiO_2 are consistent with previous study: from rutile to baddeleyite phase upon compression and baddeleyite to $\alpha\text{-PbO}_2$ phase upon decompression. Interestingly, a unique phase transition phenomenon was observed for nanowires that rutile phase coexist with baddeleyite phase at the highest pressure and with $\alpha\text{-PbO}_2$ at the recovered pressure. For phase transition pressures, the onset transition pressures (17.6 GPa, 18.3 GPa and 20.8 GPa for nanowires, flower-like nanorods and nanotubes, respectively) are found to be much higher than bulk and nanoporous materials which may due to the high surface energy of 1D nanostructures. From SEM images, flower-like nanorods and nanotubes have close nano-size of ~ 100 nm, but the transition pressure of nanotubes is higher than flower-like nanorods. This may be due to the high surface energy of nanotubes. High-pressure studies of these 1D rutile TiO_2 nanomaterials indicate that morphology plays a dominant role which affects the high-pressure behaviours of TiO_2 nanomaterials.

Morphology changes of four 1D rutile TiO_2 samples after compression and decompression were also characterized by SEM. As shown in Figure 2-2 c, 2-3 d, 2-5 c, after high-pressure experiments, the morphologies of nanowires, nanorods and nanotubes exhibited dramatically change and the previous forms are no longer

recognizable. However, the flower-like nanorods morphology (Figure 2-4 c) is still recognizable after decompression which indicates the stability of flower-like nanorods morphology is higher than other morphologies under high pressure.

Figure 2-18 shows the pressure-dependent variations of normalized unit cell lengths (a/a_0 , c/c_0) for rutile TiO_2 nanowires, flower-like nanorods and nanotubes as a comparison. The a/a_0 and c/c_0 values of all three samples are decreased with increasing pressure and a -axis is found to be more compressible than the c -axis, which is consistent with previous studies.³⁷ This behaviour has been attributed to chains of edge-sharing octahedral lying parallel to the c axis in the crystal structure of rutile TiO_2 phase.³⁹ Moreover, a -axis and c -axis of TiO_2 nanotubes show higher compressibility than nanowires and flower-like nanorods. Specifically, compressibility of materials can be characterized by bulk modulus. The pressure volume data of the rutile phase was fitted to the third-order Birch-Murnaghan equation of state (equation 2.1):

$$P/B_0 = 3/2(x^{7/3} - x^{5/3}) [1 + 3/4(B'_0 - 4)(x^{2/3} - 1)] \quad (2.1)$$

Where $x = V_0/V$, V being the volume at pressure P and V_0 is the zero-pressure volume. The constants B_0 and B'_0 are the isothermal bulk modulus and its pressure derivative, respectively. Both parameters are evaluated at zero pressure. They are calculated from the fit to the equation of state by a least-squares method.

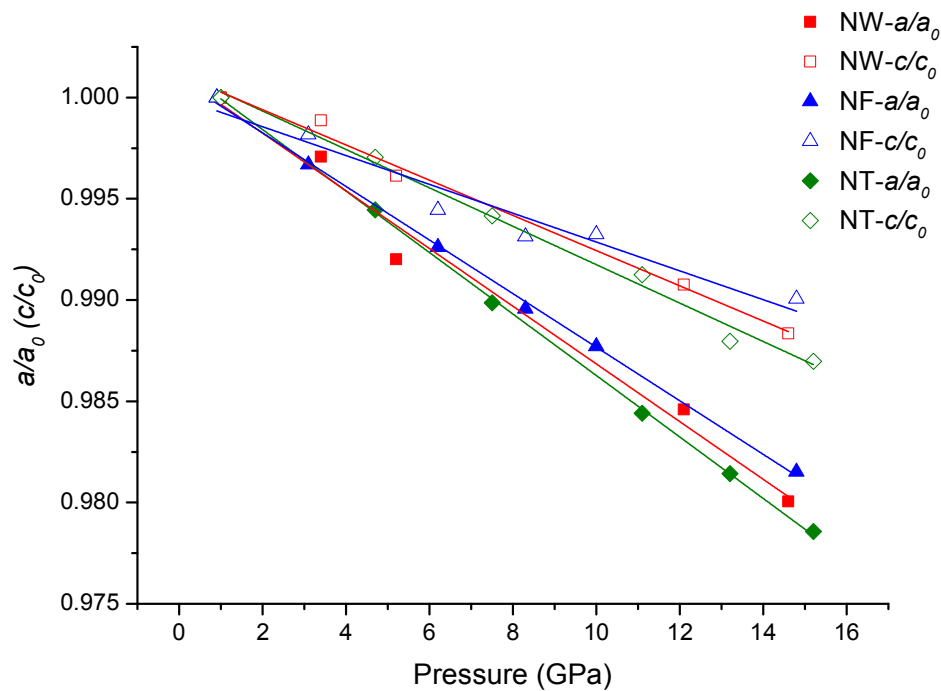


Figure 2-18 Relative lattice parameters (a/a_0 , c/c_0) of rutile TiO_2 nanowires (NW), flower-like nanorods (NF) and nanotubes (NT) as a function of compression. The straight lines are only for eye guidance.

The pressure-volume data of these three morphologies are shown in Figure 2-19. By fitting the third-order Birch-Murnaghan equation of state, with the first derivative (B'_0) fixed at 6.6, the bulk modulus (B_0) of flower-like nanorods, nanotubes and nanowires are determined to be 206 GPa, 193 GPa and 208 GPa, respectively. Bulk modulus of rutile TiO_2 bulk, nanocrystals and nanoporous materials are also shown in Figure 2-22 for comparisons. As can be seen, bulk modulus of TiO_2 nanotubes have the lowest value of 198 GPa and nanocrystals have the highest bulk modulus than other rutile TiO_2 nanomaterials. Size- and morphology-induced alteration of bulk modulus has been found in many nanomaterials. For instance, another phase of TiO_2 , i.e., anatase, its nanotubes morphology has the lowest bulk modulus (164 GPa) compared with nanowires (266 GPa for 50-100 nm) and nanoparticles (243 GPa for 30-34 nm).²⁶ Other nanomaterials, such as CeO_2 nanoparticles exhibited an enhancement of the bulk modulus compared with the bulk materials,⁴⁰ whereas no obvious difference in

compressibility was observed for ZnS nanocrystals.¹⁵ In this work, TiO₂ nanotubes and flower-like nanorods have similar diameters with different bulk modulus values, indicating a morphology-induced alteration of bulk modulus. Some of anatase TiO₂ 1D nanomaterials studies suggested that bulk modulus may be influenced by the crystal growth directions of TiO₂ nanomaterials. Park *et al.*,⁴¹ found anatase TiO₂ nanorods (grown along the *a*-axis) showed lower modulus (243 GPa), but the anatase TiO₂ nanorice (grown along the *c*-axis) showed a higher modulus (319 GPa). In addition, low bulk modulus might be due to the crystal-chemical defects, such as oxygen vacancies,⁴² and their dependence on the size and shape.

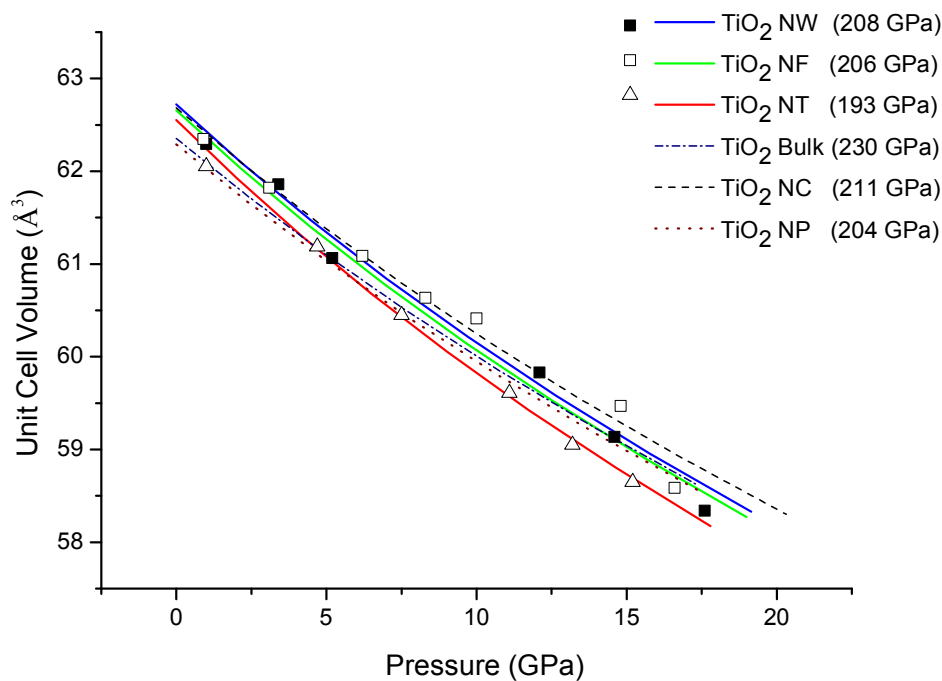


Figure 2-19 Equation of state for rutile TiO₂ in morphologies of nanowires (NW), flower-like nanorods (NF), and nanotubes (NT) upon compression. The blue dashed line is the equation of state for rutile phase in bulk TiO₂ accepted from Ref. 37, the black dashed line is the equation of state for TiO₂ nanocrystals adapted from Ref. 38 and the red dashed line is the equation of state for TiO₂ nanoporous materials adapted from Ref. 22.

2.4 Conclusions

In summary, four 1D rutile TiO₂ nanomaterials of different morphologies were synthesized by FTO based hydrothermal method. To the best of our knowledge, the flower-like nanorods was the first time obtained by this method. The XRD and Raman data of these four morphologies indicating they are all in pure rutile structures. *In situ* Raman Spectroscopy was applied to study the high pressure behavior of all four morphologies upon compression and decompression and synchrotron XRD was used to study three morphologies under high pressure for the first time. The phase transition sequences are consistent with previous study of other rutile TiO₂ nanomaterials: rutile to baddeleyite structure on compression and baddeleyite to α -PbO₂ structure on decompression. A unique phase transition phenomenon was observed for nanowires as rutile phase sustained in the whole compression and decompression processes. The transition pressures of these 1D nanomaterials were found to be significantly higher than bulk and 2D nanoporous material (Table 2-1). Two morphologies of flower-like nanorods and nanotubes have similar diameters show different phase transition onset pressure at ~ 18.3 GPa and ~ 20.8 GPa, respectively, suggesting that morphology difference plays a dominant role in influencing the phase transition pressure of 1D nanostructured rutile TiO₂. Moreover, the study of compressibility of unit cell along *a* axis and *c* axis shows that *a* axis has higher compressibility than *c* axis, which is consistent with previous work. Bulk moduli study for three 1D rutile TiO₂ are derived from the P-V data. Compared with other nanomaterials, nanotubes have the lowest value of 193 GPa. The morphology-induced alteration of compressibility might be due to the crystal growth direction or/and the crystallo-chemical defects, such as oxygen vacancies. For morphology characterization after compression and decompression, some parts of the flower-like nanorods were converted to small nanoparticles, which resulted in an increased surface area. Moreover, this flower-like morphology can be partially recovered after decompression which indicates the higher stability of this morphology under high pressure.

Table 2-1 Summary of high-pressure studies of rutile TiO₂

Starting TiO ₂		Phase transitions pressure (GPa)				Bulk modulus (GPa)	Technique
Morphology	Size (nm)	rutile to baddeleyite type	rutile to α-PbO ₂ type	α-PbO ₂ to baddeleyite type	baddeleyite to α-PbO ₂ type	Rutile phase	
Bulk	N/A	12.0-20.0 ³⁷			7.0	230 (20)	XRD
			10 ³⁶	15 ³⁶	ambient		Raman
Nanoparticles	10	20.0-30.0 ³⁸			4.0-2.0	204 (4)	XRD
Nanoporous material	N/A	10.8-26.1 ²²			4.0	211 (7)	Raman
Nanowires*	10-30	17.6			7.4	208 (2)	Raman
Nanorods*	70-110	20.7			5.5		Raman
Flower-like nanorods*	~100	18.3			8.7	206 (3)	Raman
Nanotubes*	~100	20.8			< 9.7	193 (3)	Raman

* This work

2.5 References

- (1) Miao, Z.; Xu, D. S.; Ouyang, J. H.; Guo, G. L.; Zhao, X. S.; Tang, Y. Q. *Nano Lett.* **2002**, *2*, 717.
- (2) Ning, Y. S.; Zhang, X. B.; Wang, Y. W.; Sun, Y. L.; Shen, L. H.; Yang, X. F.; Van Tendeloo, G. *Chem. Phys. Lett.* **2002**, *366*, 555.
- (3) Kasuga, T.; Hiramatsu, M.; Hoson, A.; Sekino, T.; Niihara, K. *Langmuir* **1998**, *14*, 3160.
- (4) Aruna, S. T.; Tirosh, S.; Zaban, A. *J. Mater. Chem.* **2000**, *10*, 2388.
- (5) Gratzel, M. *Nature* **2001**, *414*, 338.
- (6) Braun, J. H.; Baidins, A.; Marganski, R. E. *Prog. Org. Coat.* **1992**, *20*, 105.
- (7) Tryk, D. A.; Fujishima, A.; Honda, K. *Electrochim. Acta* **2000**, *45*, 2363.
- (8) Hagfeldt, A.; Gratzel, M. *Chem. Rev.* **1995**, *95*, 49.
- (9) Linsebigler, A. L.; Lu, G. Q.; Yates, J. T. *Chem. Rev.* **1995**, *95*, 735.
- (10) Li, Q. J.; Liu, B. B.; Wang, L.; Li, D. M.; Liu, R.; Zou, B.; Cui, T.; Zou, G. T.; Meng, Y.; Mao, H. K.; Liu, Z. X.; Liu, J.; Li, J. X. *J. Phys. Chem. Lett.* **2010**, *1*, 309.
- (11) Guo, Z. Y.; Dong, X. L.; Zhou, D. D.; Du, Y. J.; Wang, Y. G.; Xia, Y. Y. *RSC Adv.* **2013**, *3*, 3352.
- (12) Wu, H. B.; Hng, H. H.; Lou, X. W. *Adv. Mater.* **2012**, *24*, 2567.
- (13) Zhang, H. Z.; Banfield, J. F. *Chem. Rev.* **2014**, *114*, 9613.
- (14) San-Miguel, A. *Chem. Soc. Rev.* **2006**, *35*, 876.
- (15) Jiang, J. Z.; Gerward, L.; Frost, D.; Secco, R.; Peyronneau, J.; Olsen, J. S. *J. Appl. Phys.* **1999**, *86*, 6608.
- (16) Dong, Z. H.; Song, Y. *Chem. Phys. Lett.* **2009**, *480*, 90.
- (17) Dong, Z. H.; Song, Y. *Appl. Phys. Lett.* **2010**, *96*.
- (18) Dong, Z. H.; Zhuravlev, K. K.; Morin, S. A.; Li, L. S.; Jin, S.; Song, Y. *J. Phys. Chem. C* **2012**, *116*, 2102.
- (19) Hearne, G. R.; Zhao, J.; Dawe, A. M.; Pischedda, V.; Maaza, M.; Nieuwoudt, M. K.; Kibasomba, P.; Nemraoui, O.; Comins, J. D.; Witcomb, M. J. *Phys. Rev. B* **2004**, *70*.
- (20) Kurita, S.; Ohta, S.; Sekiya, T. *High Pressure Res.* **2002**, *22*, 319.
- (21) Kumar, S. G.; Rao, K. *Nanoscale* **2014**, *6*, 11574.
- (22) Li, Q. J.; Liu, R.; Liu, B. B.; Wang, L.; Wang, K.; Li, D. M.; Zou, B.; Cui, T.; Liu, J.; Chen, Z. Q.; Yang, K. *RSC Adv.* **2012**, *2*, 9052.

- (23) Dong, Z. H.; Song, Y. *Can. J. Chem.* **2015**, *93*, 165.
- (24) Liu, B.; Aydil, E. S. *J. Am. Chem. Soc.* **2009**, *131*, 3985.
- (25) Feng, X. J.; Zhu, K.; Frank, A. J.; Grimes, C. A.; Mallouk, T. E. *Angew. Chem.-Int. Edit.* **2012**, *51*, 2727.
- (26) Huang, H.; Pan, L.; Lim, C. K.; Gong, H.; Guo, J.; Tse, M. S.; Tan, O. K. *Small* **2013**, *9*, 3153.
- (27) Kumar, A.; Madaria, A. R.; Zhou, C. W. *J. Phys. Chem. C* **2010**, *114*, 7787.
- (28) Pan, L.; Huang, H.; Lim, C. K.; Hong, Q. Y.; Tse, M. S.; Tan, O. K. *RSC Adv.* **2013**, *3*, 3566.
- (29) Swamy, V.; Muddle, B. C.; Dai, Q. *Appl. Phys. Lett.* **2006**, *89*.
- (30) Lagarec, K.; Desgreniers, S. *Solid State Commun.* **1995**, *94*, 519.
- (31) Swamy, V.; Dubrovinsky, L. S.; Dubrovinskaia, N. A.; Langenhorst, F.; Simionovici, A. S.; Drakopoulos, M.; Dmitriev, V.; Weber, H. P. *Solid State Commun.* **2005**, *134*, 541.
- (32) Filatov, S. K.; Bendeliani, N. A.; Albert, B.; Kopf, J.; Dyuzheva, T. I.; Lityagina, L. M. *Dokl. Phys.* **2007**, *52*, 195.
- (33) Wang, Y. J.; Zhao, Y. S.; Zhang, J. Z.; Xu, H. W.; Wang, L. P.; Luo, S. N.; Daemen, L. L. *J. Phys.-Condes. Matter* **2008**, *20*.
- (34) Arlt, T.; Bermejo, M.; Blanco, M. A.; Gerward, L.; Jiang, J. Z.; Olsen, J. S.; Recio, J. M. *Phys. Rev. B* **2000**, *61*, 14414.
- (35) Ankang, Z. M.Sc. Thesis, University of Western Ontario, London, 2013.
- (36) Arashi, H. *J. Phys. Chem. Solids* **1992**, *53*, 355.
- (37) Gerward, L.; Olsen, J. S. *J. Appl. Crystallogr.* **1997**, *30*, 259.
- (38) Olsen, J. S.; Gerward, L.; Jiang, J. Z. *High Pressure Res.* **2002**, *22*, 385.
- (39) Smith, J. V. *Geometrical and Structural Crystallography*; John Wiley: New York:, **1982**.
- (40) Wang, Z. W.; Zhao, Y. S.; Schiferl, D.; Zha, C. S.; Downs, R. T. *Appl. Phys. Lett.* **2004**, *85*, 124.
- (41) Park, S. W.; Jang, J. T.; Cheon, J.; Lee, H. H.; Lee, D. R.; Lee, Y. *J. Phys. Chem. C* **2008**, *112*, 9627.
- (42) Schaub, R.; Wahlstrom, E.; Ronnau, A.; Laegsgaard, E.; Stensgaard, I.; Besenbacher, F. *Science* **2003**, *299*, 377.

Chapter 3 High-pressure Studies of Nanostructured $\text{Li}_4\text{Ti}_5\text{O}_{12}$ by Raman Spectroscopy and Synchrotron X-ray Diffraction

3.1 Introduction

Lithium-ion batteries (LIBs) have been widely used as power sources for electric vehicles because of their high energy density, high power density, and environmentally friendly features.¹⁻⁴ However, the technologies of LIBs are currently facing some challenges in safety, cost, and service-life.⁵ For instance, carbon materials as anode material suffer from capacity degradation incurred by irreversible side reactions which lead to the formation of solid-electrolyte interphase (SEI) during charge-discharge cycles.^{6,7} Thus, better alternative anode materials have been sought after in the past decades. Among all potential candidate materials, lithium titanium oxide ($\text{Li}_4\text{Ti}_5\text{O}_{12}$ or LTO) has attracted much attention due to its uniquely tunable properties as anode materials and thus outstanding performance in LIB operations.⁸⁻¹⁴ Compared with other anode materials, the main benefits of $\text{Li}_4\text{Ti}_5\text{O}_{12}$ include no SEI formation and zero lattice strain during lithium intercalation/deintercalation processes.¹¹ Moreover, $\text{Li}_4\text{Ti}_5\text{O}_{12}$ also has other advantages such as low toxicity, low raw material cost and long cycle life. Compared to the bulk LTO structures, the nanostructured LTO showed significantly improved reversible capacities and rate capability. The improvement was believed due to the reduction of Li ion diffusion pathway in the particles and better accessibility of the electrolyte to the nanoparticles.¹⁵ As a result, many methods have been developed to synthesize nanostructured LTO. For instance, microwave-assisted hydrothermal (MH) methods recently has been successfully applied due to the advantages such as extremely rapid kinetics of crystallization leading to shorter reaction time, as well as mild processing conditions such as lower temperatures required.^{16,17}

The crystal structure of $\text{Li}_4\text{Ti}_5\text{O}_{12}$ has been well established as a spinel-type cubic lattice with space group of $Fd\bar{3}m$ (Fig. 1). Specifically, the general formula of LTO using Wyckoff notation, can be denoted as $[\text{Li}_3]_{8a}[\text{LiTi}_5]_{16d}[\text{O}_{12}]_{32e}$. All the 8a sites are occupied by lithium and the 16d sites are shared by lithium and titanium with a ratio

of 1:5. In the charging process, three moles of Li atoms at 8a sites and three moles of new intercalated Li move to the empty 16c sites. Then, $\text{Li}_4\text{Ti}_5\text{O}_{12}$ converts to a rock salt structure of $\text{Li}_7\text{Ti}_5\text{O}_{12}$ ($[\text{Li}_6]_{16c}[\text{LiTi}_5]_{16d}[\text{O}_{12}]_{32e}$).¹⁸ The spinel to rock salt phase transition is essential in the understanding of lithiation/delithiation mechanism and battery performance, and thus has been extensively investigated. Other possible structural transitions of LTO, such as under high temperatures, has also been explored.¹⁹ For instance, Leonidov et al.²⁰ reported a phase transition from spinel structure to a defect structure of the NaCl type due to a redistribution of lithium ions. Overall, new polymorphs of electrode materials observed under non-ambient conditions have attracted recent attentions due to the new structural information with strong implications in battery performance.²¹⁻²³

In general, the structures and properties of nanomaterials are largely determined by the chemical synthetic routes. However, it has been demonstrated that the application of external pressure can provide an additional driving force to modify the structures as well as morphology of nanomaterials.²⁴⁻³⁰ A unique benefit of structural tuning by high pressure study is that pressure-induced phase transformations may provide a new synthetic route for the production of novel structures with improved performance. As a matter of fact, a number of electrode materials have been produced under high pressures with subsequently optimized performance in battery applications.³¹⁻³⁵ Moreover, for electrode materials, structural stability is an important factor which influences the applications of LIBs because structural stability is strongly associated with superior capacity retention and long cycle life. In particular, lattice strain as an important parameter of structural stability and compressibility can be probed and tuned under external compression conditions. In addition, other intrinsic structural characteristics such as lattice defects, interstitial vacancies, as well as interfacial states, which can be revealed and regulated by compression, may also play important contributing roles in battery performance. Currently, different morphologies of nanostructured LTO materials have been tested with contrasting performance.¹⁷ However, the determining factors associated with the different battery performance remain unclear. Therefore, studying the structure stability of nanostructured $\text{Li}_4\text{Ti}_5\text{O}_{12}$

and examining the possibility of formation of new structures under external stress, as well as the understanding of the correlation between structures and performance, is of fundamental interest.

Here, we report the first high-pressure study of two different morphologies of nanostructured $\text{Li}_4\text{Ti}_5\text{O}_{12}$ using *in situ* Raman and synchrotron X-ray diffraction techniques. The Raman spectra and X-ray diffraction patterns revealed interesting contrasting high-pressure behaviours between these two nanostructured $\text{Li}_4\text{Ti}_5\text{O}_{12}$ materials, which allows the detailed analysis of structural stability and reversibility. This new structural information at microscopic level provides deep insight into the understanding of battery performance and may provide useful guidance for the design of new anode materials for LIB applications.

3.2 Experimental

Two different nanostructured $\text{Li}_4\text{Ti}_5\text{O}_{12}$ (LTO) were synthesized by microwave-assisted hydrothermal method with a mixture of LiOH , H_2O_2 and titanium tetraisopropoxide (TTIP) following the procedures reported previously.¹⁷ The materials were characterized by X-ray diffraction (XRD, Rigaku RU-200BVH with the Co K -radiation source, wavelength = 1.7892 Å) and field emission scanning electron microscopy (SEM, Hitachi S4800) to check the crystal structures, purity and morphology. The SEM images (Figure 3-1) revealed that with different experiment condition,¹⁷ two morphologies of $\text{Li}_4\text{Ti}_5\text{O}_{12}$ samples were obtained, i.e., nanoflower-like spheres with thickness of ~10 nm and nanoparticles with size ranging from tens to hundreds of nm for which we label as LTO-1 and LTO-2, respectively. In a previous electrochemical study, both materials exhibit good discharge capacities but LTO-1 has a better performance in terms of reversibility and cycling lifetime than LTO-2.

A symmetrical diamond anvil cell (DAC) with two type-I diamonds of 400 μm culets was used for the high-pressure *in situ* Raman measurements and synchrotron X-ray

diffraction experiment. A hole with a diameter of 130 μm was drilled at the centre of the stainless steel gasket and used as a sample chamber. The samples were loaded without pressure transmitting medium (PTM) for Raman measurements, whereas silicon oil was used as the PTM for X-ray diffraction measurements. A few ruby chips were inserted into the sample chamber as the pressure calibrant before loading the LTO samples and pressure was determined by the well-established ruby fluorescence method.

In situ high-pressure Raman spectroscopy was performed using a customized Raman system in house. Briefly, A 782 nm solid state laser with an output power of 50 mW was used as the excitation source. The scattered light was then dispersed using an imaging spectrograph (SpectroPro-2500i, Acton Research Corporation) equipped with a 1200 lines/mm grating achieving a 0.1 cm^{-1} resolution. The Raman signal was recorded using an ultrasensitive, liquid nitrogen cooled, back-illuminated, charge-coupled device (CCD) detector from Acton. The Rayleigh scattering was removed by an edge filter. The system was calibrated by neon lines with an uncertainty of $\pm 1\text{ cm}^{-1}$. Raman data for each pressure point were collected in the spectral region of $100\text{-}800\text{ cm}^{-1}$, corresponding to the lattice vibrations with accumulation time of 200 s.

Angle-dispersive X-ray diffraction measurements on both LTO samples were carried out on compression and decompression at pressures up to 27 GPa and reproduced at two different synchrotron facilities, i.e., Shanghai Synchrotron Radiation Facility (SSRF), China and Advanced Photon Source (APS) in Argonne National Laboratory (ANL), USA. Specifically, a hard X-ray micro-focusing undulator beamline, BL15U1 at SSRF equipped with Si (111) double crystal monochromator producing $\lambda=0.6888\text{ \AA}$ X-ray beam was used for *in-situ* diffraction experiments. The beam size at the sample was estimated to be $10\text{ }\mu\text{m}$ in diameter. The diffraction data were recorded on a MAR-165 CCD detector with an exposure time of 60 s. Similar diffraction measurements were also carried out at beamline 16BM-D at APS. The radiation with $\lambda=0.4246\text{ \AA}$ and with a comparable beam size of $5 \times 12\text{ }\mu\text{m}^2$ was used and the diffraction data were recorded on a MAR345 imaging plate with an exposure time of

60 s. CeO_2 was used as calibration material at both beamlines. The 2D Debye-Scherrer diffraction patterns were integrated by using Fit2D program for further analysis. The structural refinement was performed using GSAS software package.

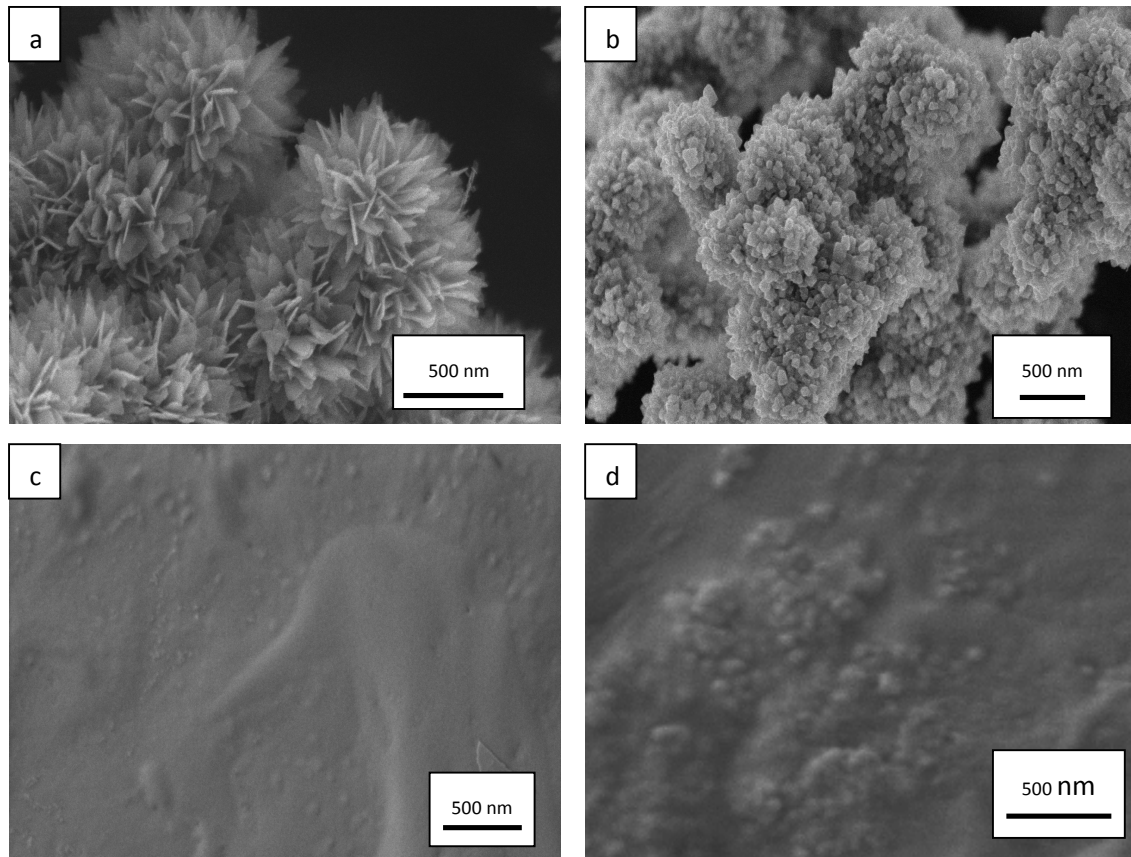


Figure 3-1 SEM images of (a) nanoflower-like spheres $\text{Li}_4\text{Ti}_5\text{O}_{12}$ (LTO-1); (b) nanoparticles $\text{Li}_4\text{Ti}_5\text{O}_{12}$ (LTO-2);¹⁷ (c) (d) view after compression/decompression in DAC for these two morphologies respectively.

3.3 Results and discussion

3.3.1 Raman results of nanostructured $\text{Li}_4\text{Ti}_5\text{O}_{12}$ upon compression and decompression

3.3.1.1 Nanoflower-like spheres $\text{Li}_4\text{Ti}_5\text{O}_{12}$ (LTO-1)

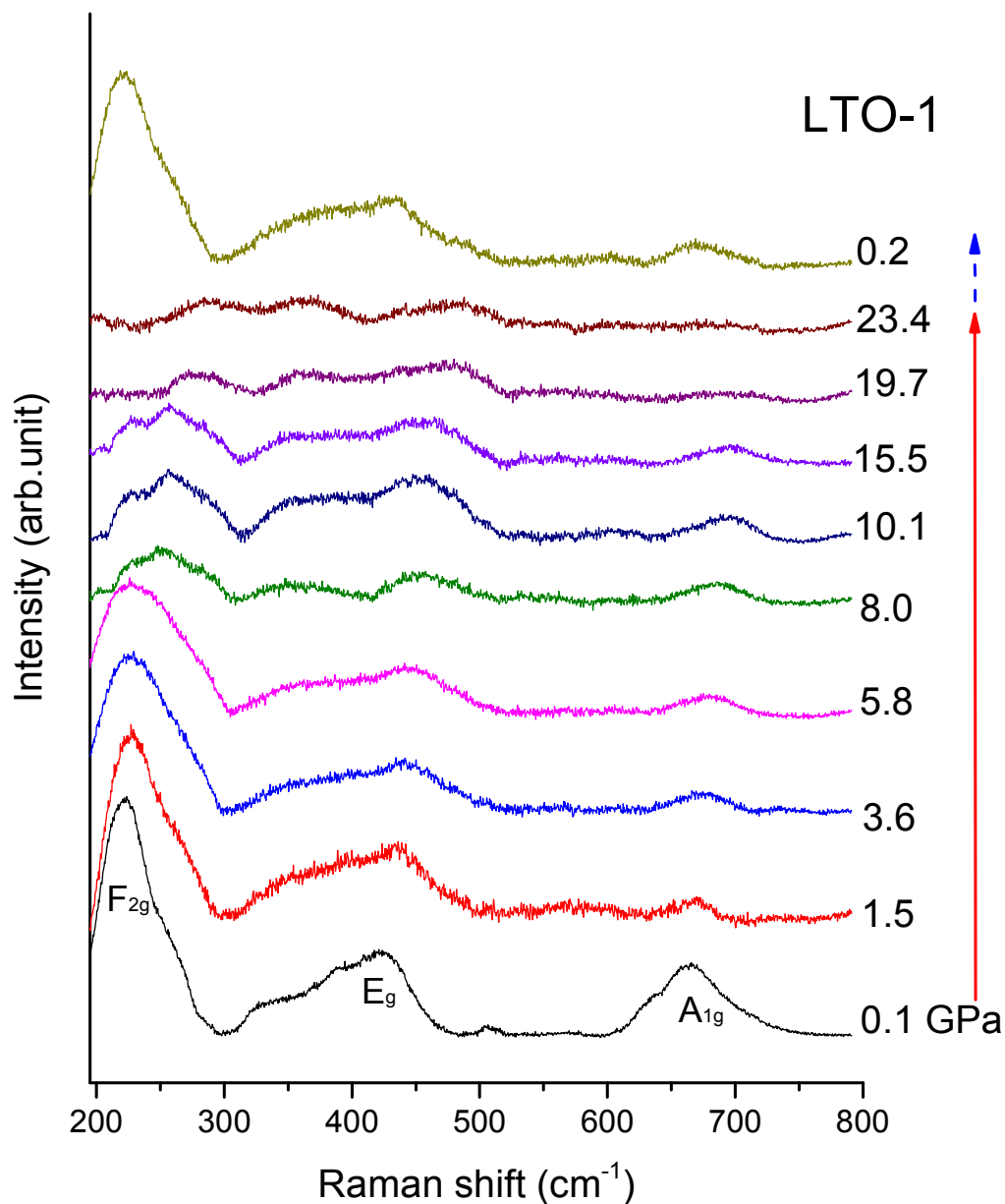


Figure 3-2 Selected Raman spectra of LTO-1 upon compression and decompression. The red and blue arrows indicate the compression and decompression sequence, respectively.

Selected Raman spectra of LTO-1 collected upon compression to a pressure of 23.4 GPa and its corresponding decompression were shown in Figure 3-2. Five active

Raman modes are predicted for cubic $\text{Li}_4\text{Ti}_5\text{O}_{12}$: $A_{1g} + E_g + 3F_{2g}$.²⁰ Three modes (F_{2g} , E_g and A_{1g}) are observed at ambient condition in our LTO-1 sample as assigned in Figure 3-2. One of the peaks of F_{2g} modes at 222 cm^{-1} is predominantly related to oxygen atom displacement and involves also lithium ion motions, especially in the low frequency region of the spectra.¹⁹ The second peak at 425 cm^{-1} is assigned to the stretching vibrational mode of Li-O ionic bonds located in LiO_4 tetrahedral (E_g).³⁶ The third peak of A_{1g} at 665 cm^{-1} originates from the stretching vibrational mode of Ti-O covalent bonding in TiO_6 octahedra.³⁷

Upon compression to 15.5 GPa stepwise, all Raman peaks are obviously broadening and blue shifting (Figure 3-4). At the highest pressure of ~ 23.4 GPa, all Raman bands mostly vanished. These observations suggest gradual pressure-induced disordering and possibly to an amorphous state without well-defined crystalline-to-crystalline transitions. The reversibility of pressure effect on crystal structures also provides important information on transformation mechanism. Therefore, after compressed to 23.4 GPa, Raman measurement of LTO-1 upon decompression were also conducted. In general, the intensity of these three peaks increased gradually as pressure decreased and all Raman modes shifted to lower frequencies. Gradual back transformation from disordered to crystalline structures was observed as indicated by the recovery of major Raman bands. After pressure was released to 0.1 GPa, all three peaks of $\text{Li}_4\text{Ti}_5\text{O}_{12}$ are mostly recovered with modifications in intensity which indicates this structural change mostly reversible.

3.3.1.2 Nanoparticles $\text{Li}_4\text{Ti}_5\text{O}_{12}$ (LTO-2)

Selected Raman spectra of nanoparticles $\text{Li}_4\text{Ti}_5\text{O}_{12}$ collected upon compression to a pressure of 23.9 GPa and its corresponding decompression are shown in Figure 3-3. Four of the predicted Raman modes ($F_{2g(1)}$, $F_{2g(2)}$, E_g , A_{1g}) are observed in LTO-2 sample. Moreover, additional minor peaks for LTO-2 (e.g., 310, 326, and 392 cm^{-1}) were also observed. These peaks most likely associated with morphology effect and detailed local lattice structures of LTO-2.

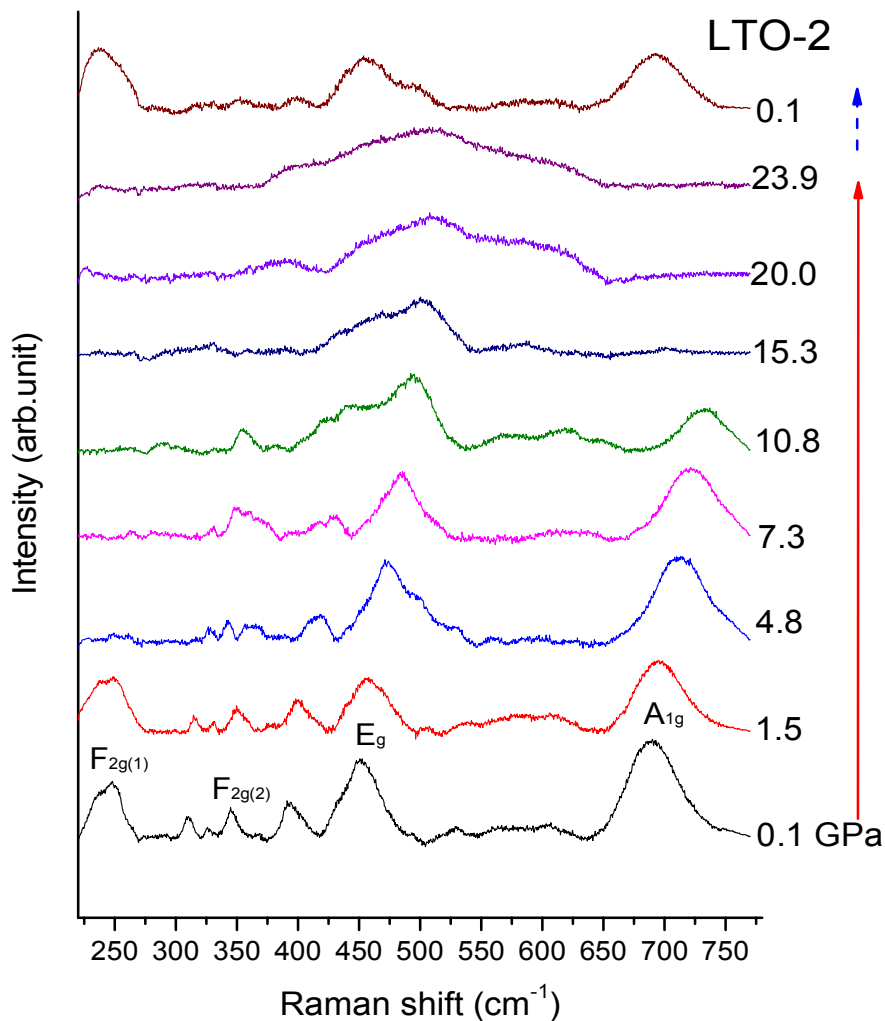


Figure 3-3 Selected Raman spectra of LTO-2 upon compression and decompression. The red and blue arrows indicate the compression and decompression sequence, respectively.

Upon compression, similar to LTO-1, all Raman bands of LTO-2 shift to higher frequencies with decreasing intensity and band broadening (Figure 3-3). The observed Raman modes of LTO-1 and LTO-2 and their pressure dependence are listed in Table 3-1 as well. At 4.8 GPa, the F_{2g} mode at 248 cm^{-1} was substantially depleted and up to 10.8 GPa, the minor Raman bands in the region of $300\text{--}425\text{ cm}^{-1}$ are also significantly weakened, leaving only the major characteristic lattice modes (i.e., F_{2g} , E_g and A_{1g})

observed. The pressure behavior of all these modes, which are associated with Li-O stretching vibrations, suggest instability of Li-O lattice possibly due to the lattice defect in LTO-2. LTO-2 was also found to go to a disordered or an amorphous state at similar pressure above 20 GPa as indicated by broadened featureless Raman profile. Upon decompression, when the pressure was released to 0.1 GPa, three peaks ($F_{2g(1)}$, E_g , A_{1g}) of LTO-2 were mostly recovered with modifications in intensity whereas the minor bands in the region of 300-425 cm^{-1} for LTO-2 were not recovered. Since all non-recovered bands in LTO-2 are believed to be associated with vibrations of disordered Li-O tetrahedrons, clearly these defect sites do not sustain external stress at this level and thus have been substantially modified by compression.

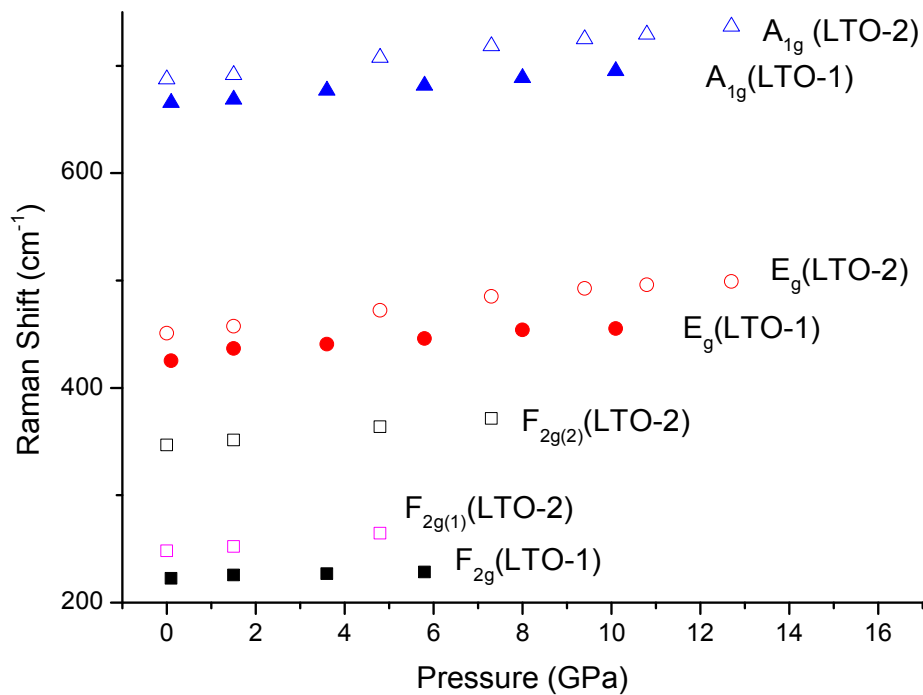


Figure 3-4 Pressure dependence of Raman active mode frequencies of LTO-1 (F_{2g} , E_g , A_{1g}) and LTO-2 ($F_{2g(1)}$, $F_{2g(2)}$, E_g , A_{1g}) upon compression.

Table 3-1 Observed Raman active modes of $\text{Li}_4\text{Ti}_5\text{O}_{12}$ nanostructures and their pressure dependence

LTO-1				LTO-2				
Pressure (GPa)	Raman shifts (cm^{-1})			Pressure (GPa)	Raman shifts (cm^{-1})			
	F_{2g}	E_g	A_{1g}		$F_{2g(1)}$	$F_{2g(2)}$	E_g	A_{1g}
0.1	222.5	425.3	665.7	0.1	248.1	346.8	450.9	687.4
1.5	225.8	436.7	668.6	1.5	252.3	351.2	457.3	691.6
3.6	226.9	440.6	677.1	4.8	264.5	363.8	472.3	707.7
5.8	228.4	446.1	681.6	7.3		371.4	485.2	718.5
8.0		453.9	688.8	9.4			492.7	724.8
10.1		455.2	695.3	10.8			495.8	729.1
				12.7			499.1	736.6

3.3.2 Synchrotron XRD results of nanostructured $\text{Li}_4\text{Ti}_5\text{O}_{12}$ upon compression and decompression

3.3.2.1 Nanoflower-like spheres $\text{Li}_4\text{Ti}_5\text{O}_{12}$ (LTO-1)

Selected XRD patterns for LTO-1 are depicted in Figure 3-5. *In situ* high-pressure XRD measurements were performed up to 27.1 GPa. All four reflections at the near ambient pressure can be indexed to spinel-type $\text{Li}_4\text{Ti}_5\text{O}_{12}$. At the starting pressure of near ambient, by using Rietveld refinement (Figure 3-6 a), unit cell parameter $a = 8.2666 \text{ \AA}$ was obtained, consistent with the value of $\text{Li}_4\text{Ti}_5\text{O}_{12}$ reference materials (JCPDS No. 49-0207).³⁸ As seen in Figure 3-5, all the reflections of LTO-1 shifted to higher 2θ angle with increasing pressure, indicating a pressure-induced reduction

of d -spacing or shrinkage of unit cells. Upon compression, the reflections become generally broadened and weakened, such that only the primary reflection of (111) can be observed at highest pressure of 27.1 GPa (see Figure 3-6 b). These observations suggest that LTO-1 maintains its crystal structure but with reduced crystallinity. Upon decompression, this (1 1 1) reflection obviously shifted to lower 2θ angle, indicating expanding of the unit cells. When the pressure was released to 0.2 GPa (as seen in Figure 3-6 c), all three diffraction peaks of cubic $\text{Li}_4\text{Ti}_5\text{O}_{12}$ are observed again which suggests this structural change is mostly reversible. By using Rietveld refinement, the unit cell parameter of recovered LTO-1 was found to be $a = 8.2711 \text{ \AA}$, close to the value of LTO-1 before compression ($a = 8.2666 \text{ \AA}$).

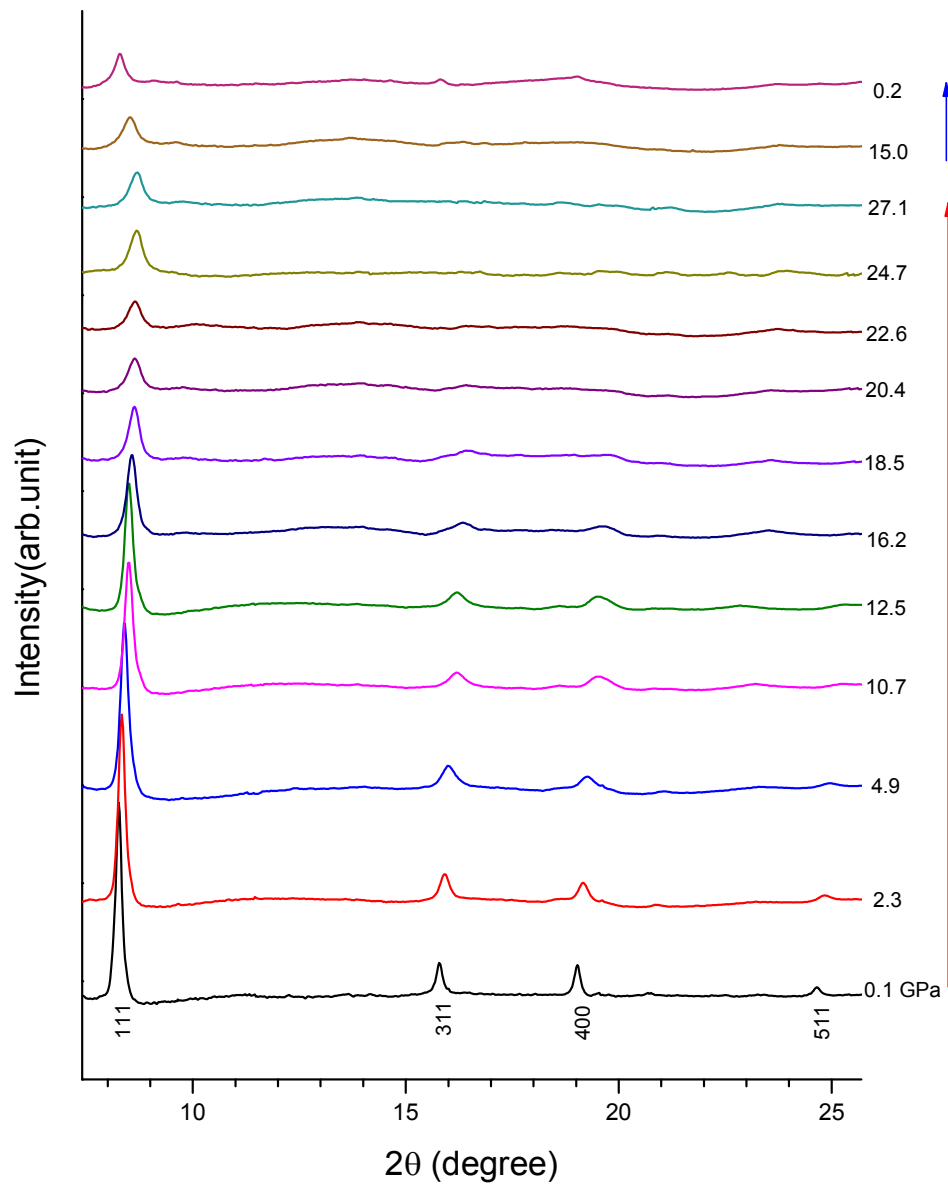
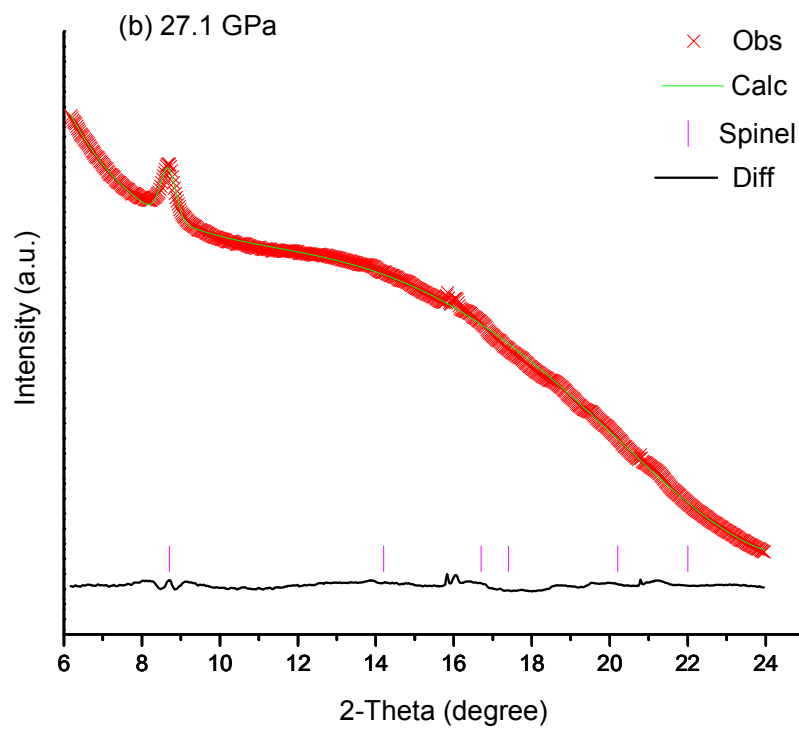
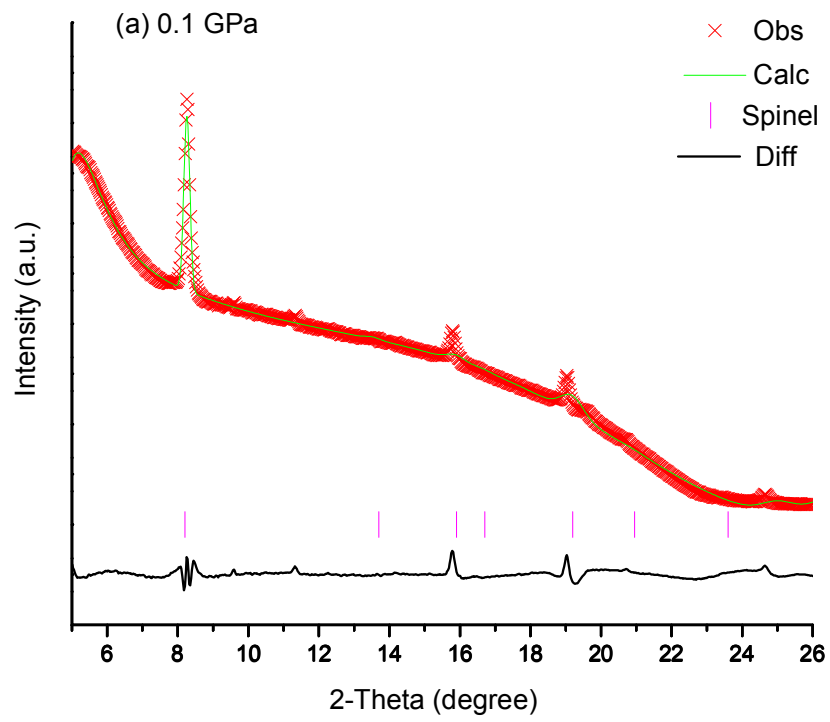


Figure 3-5 Selected X-ray diffraction patterns for LTO-1 upon compression and decompression. The red and blue arrows indicate the compression and decompression sequence, respectively.



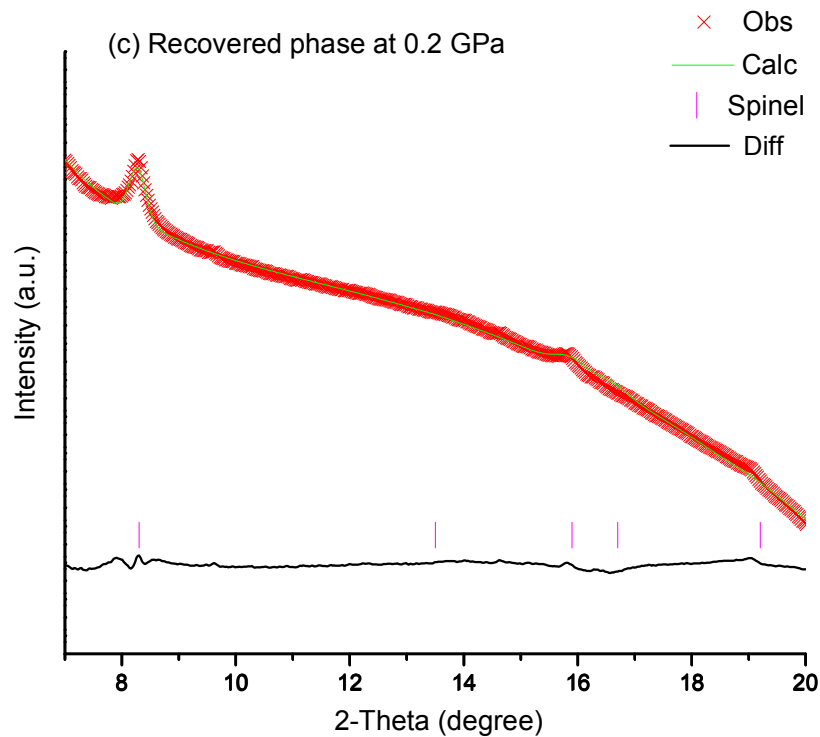


Figure 3-6 Rietveld refinement of LTO-1 XRD patterns at (a) 0.1 GPa, (b) 27.1 GPa upon compression and (c) 0.2 GPa upon decompression. The red cross is experimental X-ray intensity, whereas the green solid line is the calculated diffraction pattern based on refinement with the black curve at the bottom showing the difference between the calculated and observed intensities. The vertical bars with different color indicate the characteristic reflections of spinel-type phase.

3.3.2.2 Nanoparticles $\text{Li}_4\text{Ti}_5\text{O}_{12}$ (LTO-2)

The pressure evolution of the XRD patterns for LTO-2 is shown in Figure 3-7. Reflections that are not associated with $\text{Li}_4\text{Ti}_5\text{O}_{12}$ structure may be from impurities. At the starting pressure of near ambient, by using Rietveld refinement (Appendix II), unit cell parameter $a = 8.3071 \text{ \AA}$ was obtained, consistent with the value of spinel-type $\text{Li}_4\text{Ti}_5\text{O}_{12}$ materials (JCPDS No. 49-0207). Similar to LTO-1, all diffraction peaks are shifted to higher 2θ angle with increasing pressure. Reflections of (5 1 1) and (4 4 0) disappeared at 18.6 GPa. However, another reflections of (1 1

1), (3 1 1) and (4 0 0) are still observable up to 26.3 GPa with significantly broadened profile and weak intensity, which indicates LTO-2 is in disordered phase up to this pressure. Upon decompression, the first reflection of (1 1 1) can be gradually observed with increasing intensity and this reflection is stable after release the pressure to 0.5 GPa. However, other reflections of spinel structure LTO-2 are difficult to observe, indicating this structure is partially recovered. Unit cell parameters and volumes of LTO-1 and LTO-2 upon compression at different pressures are reported in Table 3-2.

Table 3-2 Unit cell parameters and volumes of nanostructured $\text{Li}_4\text{Ti}_5\text{O}_{12}$.

LTO-1			LTO-2		
Pressure (GPa)	Cell parameter (Å)	Cell volume (Å ³)	Pressure (GPa)	Cell parameter (Å)	Cell volume (Å ³)
0.1	8.34	581.98	1.3	8.33	579.03
2.3	8.29	570.64	2.7	8.33	578.13
4.9	8.25	563.41	6.4	8.25	563.07
8.1	8.20	551.75	9.3	8.21	554.61
10.7	8.15	543.07	11.1	8.17	547.25
12.5	8.14	540.88	13.9	8.15	541.74
14.3	8.06	524.89	16.2	8.14	539.55
16.2	8.06	523.72	18.7	8.11	534.76

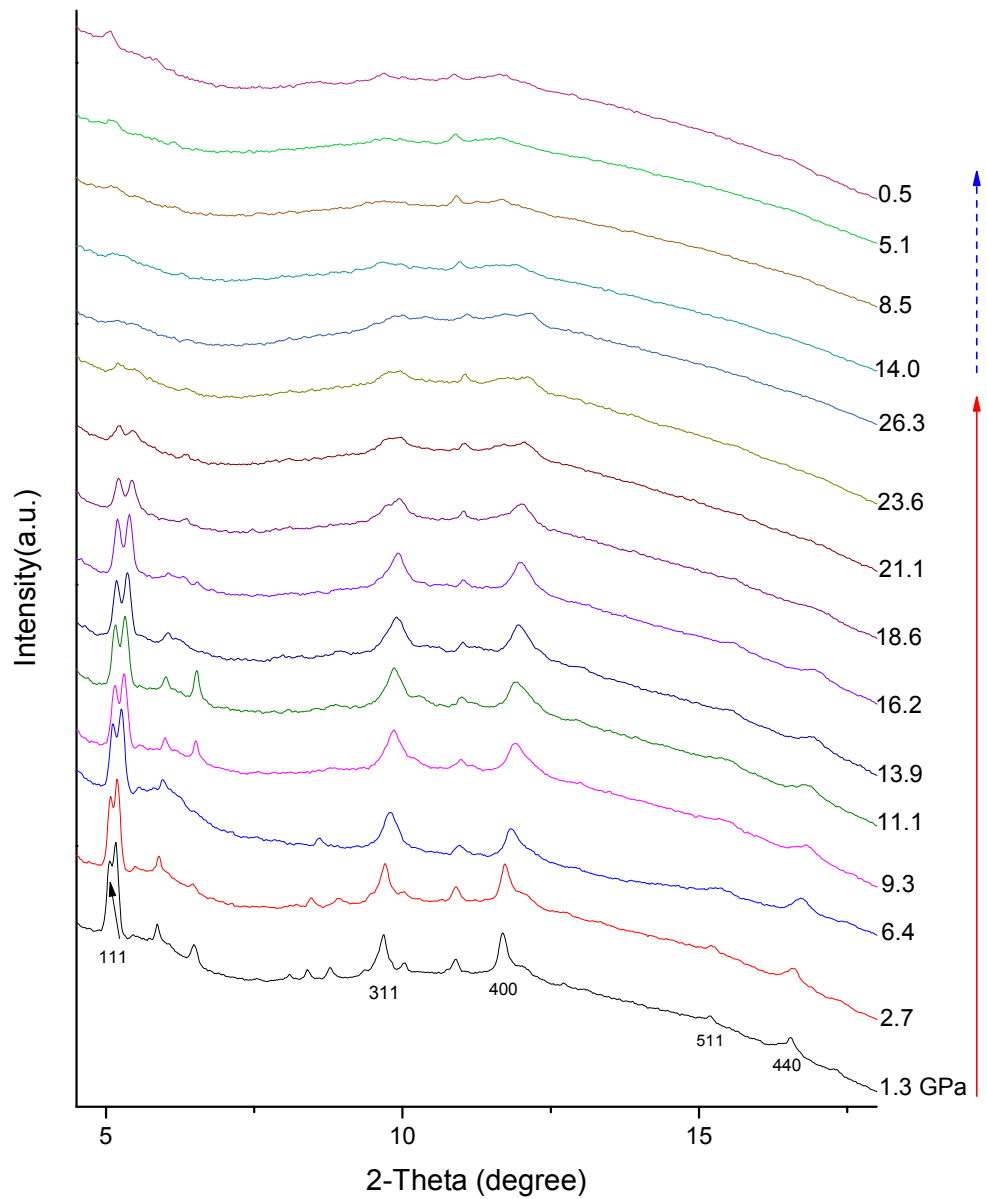


Figure 3-7 Selected X-ray diffraction patterns for LTO-2 upon compression and decompression. The red and blue arrows indicate the compression and decompression sequence, respectively.

3.3.3 Discussion

The reversibility of pressure effect on crystal structures provides important information on transformation mechanism.²⁷ Here, both Raman and XRD results suggesting that the structures change of LTO-1 and LTO-2 upon compression are reversible but with different reversibility. Three obvious reflections can be observed at the recovered XRD pattern of LTO-1 while reflections of LTO-2 at the recovered XRD pattern are significantly broaden, indicating that pressure-induced structural modification of LTO-1 is more reversible than LTO-2. From XRD data, we can also observe that recovered LTO-1 has higher crystallinity than that of LTO-2. Interestingly, the electrochemical studies of these two LTO samples show that LTO-1 also has better reversibility and cycling performance than LTO-2 possibly due to a larger contact area between electrode and electrolyte in LTO-1, which is beneficial for the Li⁺ exchange.¹⁷

Morphology changes of LTO-1 and LTO-2 after the compression and decompression were also characterized by SEM (Figure 3-1 c and d). After high-pressure experiments, the morphology of nanoflower-like sphere (Figure 3-1c) exhibited dramatically change and the previous flower-like form was no longer observable. However, the nanoparticles morphology is still recognizable after decompression (Figure 3-1 d). Such preserved particle morphology together with the larger bulk modulus (discuss below) implies the higher toughness of the nanoparticles Li₄Ti₅O₁₂ (i.e., LTO-2).

The evolution of the lattice parameter and unit cell volume of both LTO-1 and LTO-2 samples with pressure were obtained from the structural refinement of the diffraction patterns. Figure 3-8 shows the pressure-dependent variations of relative lattice parameters for LTO-1 and LTO-2 as a comparison. As shown in Figure 3-8, the normalized unit cell parameter in the form of a/a_0 ratio for both LTO-1 and LTO-2 decreased with increasing pressure.

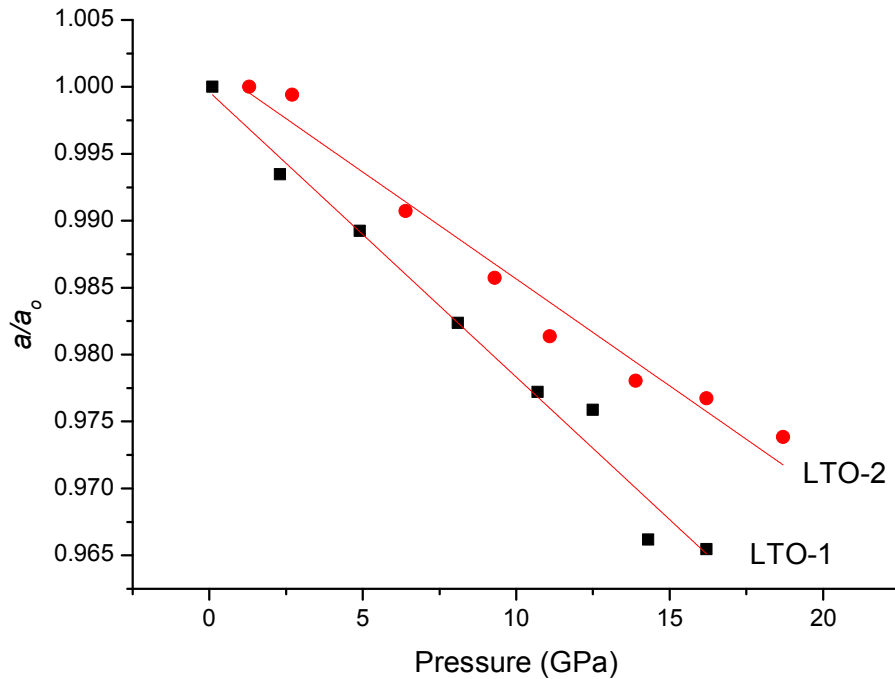


Figure 3-8 Cell parameter ratio (a/a_0) as a function of pressure for LTO-1 and LTO-2.

Solid lines are only for eye guidance.

In addition, the pressure volume data of the various phases have been fitted to Birch equation of state (EOS):³⁹

$$P/B_0 = 3/2(x^{7/3} - x^{5/3}) [1 + 3/4(B'_0 - 4)(x^{2/3} - 1)] \quad (3.1)$$

Where $x = V_0/V$, V being the volume at pressure P and V_0 is the zero-pressure volume. The constants B_0 and B'_0 are the isothermal bulk modulus and its pressure derivative, respectively. Both parameters are evaluated at zero pressure. They are calculated from the fit to the equation of state by a least-squares method. The equations of state for LTO-1 and LTO-2 upon compression are shown in Figure 3-9. By fitting the third order Birch-Murnaghan equation of state, the bulk moduli (B_0) of these two LTO samples were determined to be 123 GPa (LTO-1) and 167 GPa (LTO-2) with the first derivative (B'_0) being fixed at 4. Evidently, both the unit cell parameters and EOS suggest that nanoflower-like $\text{Li}_4\text{Ti}_5\text{O}_{12}$ spheres is more compressible than $\text{Li}_4\text{Ti}_5\text{O}_{12}$ nanoparticles. The morphology dependent variation of bulk modulus has been

reported in other high-pressure studies of nanomaterials before. It is the general understanding that the surface energy associated with different nanostructures may play a major role in influencing the compressibility of the materials. In particular, reduced dimensions and enhanced surface areas may result in the elevation of bulk modulus, such as observed in TiO_2 ,²⁴ ZnO ,³⁰ SnO_2 ,²⁶ etc., which all exhibit larger bulk modulus (i.e., lower compressibility) than the corresponding bulk materials. Therefore, we can speculate that the bulk modulus of bulk LTO materials will be lower compared to nanostructured LTO materials in the current study.

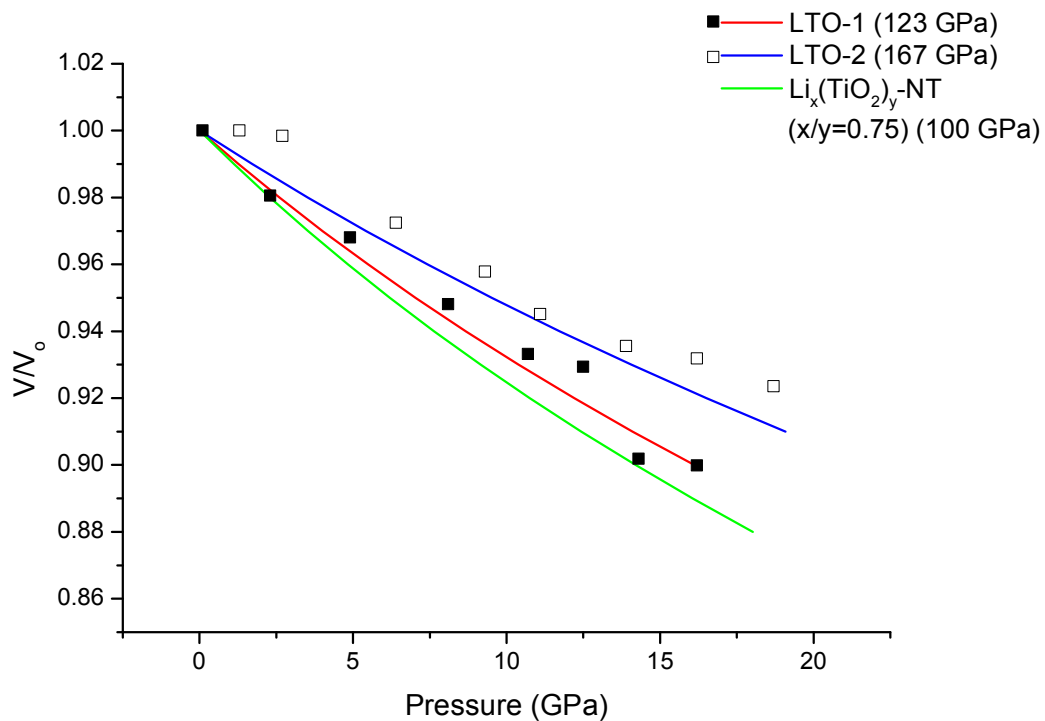


Figure 3-9 Normalized unit cell volume (V/V_0) as a function of pressure derived from structural refinement of X-ray diffraction patterns for LTO-1 (open square) and LTO-2 (solid square), and the corresponding equation of state (red and blue solid lines, respectively). The green solid line denotes the equation of state for $\text{Li}_{0.75}(\text{TiO}_2)$ nanotubes derived from Ref. 21.

Prior to the current high-pressure study, it has been reported nanostructured LTO has an improved performance than bulk materials in the LIB applications.¹¹ Moreover,

LTO-1 exhibited a substantially higher discharge capacity than LTO-2.¹⁷ Thus it is of fundamental interest to understand the origin of the difference and correlation between the performance in LIB operations and their high-pressure behaviors of the two morphologies of LTO materials. As mentioned before, the lattice strain plays an important role during lithium intercalation/deintercalation processes.⁵ The lattice strain, however, may vary substantially as a function of grain size and morphology. Ouyang *et al.*⁴⁰ recently established atomistic origin of the lattice strain in nanostructured materials. In particular, it was found that the lattice strain has a positive correlation with bulk modulus, i.e., larger lattice strain with increasing bulk modulus. Based on this relationship, we can infer that LTO-2 as nanoparticles has a larger intrinsic lattice strain than that of LTO-1, nanoflowers, consistent with the observation of the better performance of LTO-1 in LIB operations. We note that reduced dimension such as from bulk to nanostructures often includes larger lattice strain, which is unfavorable for the lithium intercalation/deintercalation. However, the enhanced surface area of the nanostructures outweighs the negative impact of lattice strain in LTO-1, whereas in LTO-2, lattice strain is the dominant factor for the performance in the LIB operations.

In addition, Xiong *et al.*²¹ established that the lattice stability may have strong implications in the long-term operation of Li-ion batteries. In their recent high-pressure study of lithiated cubic titania (c-TiO₂) nanotube Li_x(TiO₂) with compositional variations where x ranges from 0 and 1, a vacancy filling mechanism was invoked to interpret the structural stability by means of application of applied pressure that drives the interstitial Li⁺ to the cation vacancy of oxide polyhedrons. Specially, it was found that pure cubic TiO₂ (with the same spinel structure as Li₄Ti₅O₁₂) undergoes a pressure induced amorphization at only 17.5 GPa, whereas lithiated TiO₂ structures with lithiation ratio of 0.5, 0.75 and 1.0 all sustained high compression and remained crystalline at pressures even over 50 GPa. The molecular dynamic simulations further reveals that the 75% lithiated cubic TiO₂ (a unique lithium concentration) exists in a two-phase mixture of crystalline and amorphous

phase at high pressures > 35 GPa. Our results of LTO-1 are in excellent agreement with that of Xiong's in that 1) $\text{Li}_4\text{Ti}_5\text{O}_{12}$ can be considered a lithiation ratio of 4/5 or 80%, closer to 75% lithiated cubic TiO_2 ; and that 2) LTO-1 also remains crystalline at the highest pressure, but with pressure-induced disordering and partial reversibility upon decompression. Moreover, the slightly lower bulk modulus for 75% lithiated cubic TiO_2 (i.e., ~ 100 GPa) in excellent alignment with those for LTO-1 and LTO-2 obtained in this study. The relative order of the compressibility, i.e., ($\text{Li}_{0.75}\text{TiO}_2 > \text{LTO-1} > \text{LTO-2}$) as shown in Fig. 3-9) also suggests the same order of available lattice vacancy that allows additional Li ion intake and occupation of the interstitial sites by diffusion, an essential process for LIB operation. Although having the same Li/Ti ratio as LTO-1, the lattice defect and intrinsic local disorder of LTO-2, on the other hand, shows a poor structural stability and reversibility. These analyses not only interpreted the better performance and durability of LTO-1 than LTO-2, but extrapolated that lithiated c- TiO_2 could be made a slightly improved anode material with performance even better than LTO-1. Overall, this study established an important guideline that the combination of multiple factors including the surface area, lattice strain, local defect and disorderness, available vacancies, and ultimately the lattice stability must be considered comprehensively together in the design of new nanostructured electrode materials in the future.

3.4 Conclusions

In summary, two different morphologies of nanostructured $\text{Li}_4\text{Ti}_5\text{O}_{12}$ materials, i.e., nanoflower-like sphere (LTO-1) and nanoparticles (LTO-2) were investigated under high pressure using *in situ* Raman spectroscopy and synchrotron X-ray diffraction. No phase transformations other than pressure-induced structural disordering were observed in both samples. Both the Raman and diffraction measurements suggest that reversibility of the structural changes of LTO-1 is substantially higher than LTO-2. Structural refinement of the diffraction patterns allows the analysis of equation of states of both materials by yielding the respective bulk modulus of 123 GPa and 167

GPa, indicating morphology dependent compressibilities of nanostructured $\text{Li}_4\text{Ti}_5\text{O}_{12}$. Moreover, the higher compressibility of LTO-1 than LTO-2 was examined in comparison with other nanostructured lithium titanium dioxide. The difference in compressibility and reversibility suggest different lattice vacancies and structural stabilities between the two different LTO nanostructures. Based on the positive correlation between lattice strains with bulk modulus, it can be inferred that LTO-2 has a larger intrinsic lattice strain than that of LTO-1. All these analysis consistently interpret the observation of the better performance of LTO-1 than LTO-2 in LIB operations reported previously. Our study thus contributes to the design of new nanostructured anode materials by providing a practical guideline by considering multiple combined factors that may influence that their performance in the LIB operations.

3.5 References

- (1) Armand, M.; Tarascon, J. M. *Nature* **2008**, *451*, 652.
- (2) Tarascon, J. M.; Armand, M. *Nature* **2001**, *414*, 359.
- (3) Kang, K. S.; Meng, Y. S.; Breger, J.; Grey, C. P.; Ceder, G. *Science* **2006**, *311*, 977.
- (4) Winter, M.; Besenhard, J. O.; Spahr, M. E.; Novak, P. *Adv. Mater.* **1998**, *10*, 725.
- (5) Etacheri, V.; Marom, R.; Elazari, R.; Salitra, G.; Aurbach, D. *Energy Environ. Sci.* **2011**, *4*, 3243.
- (6) Kaskhedikar, N. A.; Maier, J. *Adv. Mater.* **2009**, *21*, 2664.
- (7) Arora, P.; White, R. E.; Doyle, M. *J. Electrochem. Soc.* **1998**, *145*, 3647.
- (8) Ferg, E.; Gummow, R. J.; Dekock, A.; Thackeray, M. M. *J. Electrochem. Soc.* **1994**, *141*, L147.
- (9) Zaghbi, K.; Armand, M.; Gauthier, M. *J. Electrochem. Soc.* **1998**, *145*, 3135.
- (10) Liu, P.; Sherman, E.; Verbrugge, M. *J. Solid State Electrochem.* **2010**, *14*, 585.
- (11) Yi, T. F.; Yang, S. Y.; Xie, Y. *J. Mater. Chem. A* **2015**, *3*, 5750.

- (12) Wu, N.; Yang, Z. Z.; Yao, H. R.; Yin, Y. X.; Gu, L.; Guo, Y. G. *Angew. Chem.-Int. Edit.* **2015**, *54*, 5757.
- (13) Haridas, A. K.; Sharma, C. S.; Rao, T. N. *Small* **2015**, *11*, 290.
- (14) Lu, X.; Gu, L.; Hu, Y. S.; Chiu, H. C.; Li, H.; Demopoulos, G. P.; Chen, L. Q. *J. Am. Chem. Soc.* **2015**, *137*, 1581.
- (15) Amine, K.; Belharouak, I.; Chen, Z. H.; Tran, T.; Yumoto, H.; Ota, N.; Myung, S. T.; Sun, Y. K. *Adv. Mater.* **2010**, *22*, 3052.
- (16) Komarneni, S.; Rajha, R. K.; Katsuki, H. *Mater. Chem. Phys.* **1999**, *61*, 50.
- (17) Liu, J.; Li, X. F.; Yang, J. L.; Geng, D. S.; Li, Y. L.; Wang, D. N.; Li, R. Y.; Sun, X. L.; Cai, M.; Verbrugge, M. W. *Electrochim. Acta* **2012**, *63*, 100.
- (18) Schmidt, W.; Bottke, P.; Sternad, M.; Gollob, P.; Hennige, V.; Wilkening, M. *Chem. Mat.* **2015**, *27*, 1740.
- (19) Knyazev, A. V.; Smirnova, N. N.; Maczka, M.; Knyazeva, S. S.; Letyanina, I. A. *Thermochim. Acta* **2013**, *559*, 40.
- (20) Leonidov, I. A.; Leonidova, O. N.; Perelyaeva, L. A.; Samigullina, R. F.; Kovyazina, S. A.; Patrakeev, M. V. *Phys. Solid State* **2003**, *45*, 2183.
- (21) Xiong, H.; Yildirim, H.; Podsiadlo, P.; Zhang, J.; Prakapenka, V. B.; Greeley, J. P.; Shevchenko, E. V.; Zhuravlev, K. K.; Tkachev, S.; Sankaranarayanan, S.; Rajh, T. *Phys. Rev. Lett.* **2013**, *110*.
- (22) Wang, Y. H.; Lu, X. J.; Yang, W. G.; Wen, T.; Yang, L. X.; Ren, X. T.; Wang, L.; Lin, Z. S.; Zhao, Y. S. *J. Am. Chem. Soc.* **2015**, *137*, 11144.
- (23) Lin, Y.; Yang, Y.; Ma, H. W.; Cui, Y.; Mao, W. L. *J. Phys. Chem. C* **2011**, *115*, 9844.
- (24) Dong, Z. H.; Song, Y. *Can. J. Chem.* **2015**, *93*, 165.
- (25) Dong, Z. H.; Song, Y. *Appl. Phys. Lett.* **2010**, *96*.
- (26) Dong, Z. H.; Song, Y. *Chem. Phys. Lett.* **2009**, *480*, 90.
- (27) San-Miguel, A. *Chem. Soc. Rev.* **2006**, *35*, 876.
- (28) Lu, X. J.; Yang, W. G.; Quan, Z. W.; Lin, T. Q.; Bai, L. G.; Wang, L.; Huang, F. Q.; Zhao, Y. S. *J. Am. Chem. Soc.* **2014**, *136*, 419.
- (29) Dong, Z. H.; Song, Y. *J. Phys. Chem. C* **2010**, *114*, 1782.

- (30) Dong, Z. H.; Zhuravlev, K. K.; Morin, S. A.; Li, L. S.; Jin, S.; Song, Y. *J. Phys. Chem. C* **2012**, *116*, 2102.
- (31) Fell, C. R.; Lee, D. H.; Meng, Y. S.; Gallardo-Amores, J. M.; Moran, E.; Arroyo-de Dompablo, M. E. *Energy Environ. Sci.* **2012**, *5*, 6214.
- (32) Yoncheva, M.; Stoyanova, R.; Zhecheva, E.; Alcantara, R.; Ortiz, G.; Tirado, J. L. *J. Solid State Chem.* **2007**, *180*, 1816.
- (33) Gallardo-Amores, J. M.; Biskup, N.; Amador, U.; Persson, K.; Ceder, G.; Moran, E.; Arroyo, M. E.; de Dompablo, M. *Chem. Mat.* **2007**, *19*, 5262.
- (34) Garcia-Moreno, O.; Alvarez-Vega, M.; Garcia-Alvarado, F.; Garcia-Jaca, J.; Gallardo-Amores, J. M.; Sanjuan, M. L.; Amador, U. *Chem. Mat.* **2001**, *13*, 1570.
- (35) Voss, B.; Nordmann, J.; Kockmann, A.; Piezonka, J.; Haase, M.; Taffa, D. H.; Walder, L. *Chem. Mat.* **2012**, *24*, 633.
- (36) Aldon, L.; Kubiak, P.; Womes, M.; Jumas, J. C.; Olivier-Fourcade, J.; Tirado, J. L.; Corredor, J. I.; Vicente, C. P. *Chem. Mat.* **2004**, *16*, 5721.
- (37) Kellerman, D. G.; Gorshkov, V. S.; Shalaeva, E. V.; Tsaryev, B. A.; Vovkotrub, E. G. *Solid State Sci.* **2012**, *14*, 72.
- (38) Fang, W.; Ma, Y. L.; Zuo, P. J.; Cheng, X. Q.; Yin, G. P. *Int. J. Electrochem. Sci.* **2013**, *8*, 1949.
- (39) Jung, J. H.; Kobayashi, H.; van Bommel, K. J. C.; Shinkai, S.; Shimizu, T. *Chem. Mat.* **2002**, *14*, 1445.
- (40) Ouyang, G.; Zhu, W. G.; Sun, C. Q.; Zhu, Z. M.; Liao, S. Z. *Phys. Chem. Chem. Phys.* **2010**, *12*, 1543.

Chapter 4 Summary and Future work

4.1 Summary

In recent year, high-pressure study of nanomaterials has attracted increasing attentions. Many outstanding issues, such as phase transition sequence, phase transition pressure, high pressure phases, compressibility, systematic understanding of morphology and size effect have been reported for various nanomaterials. Among all nanomaterials, TiO_2 is the most studied one due to its wide applications. The chemical and physical properties of TiO_2 nanomaterials have been extensively studied. However, the basic properties of nanostructured TiO_2 in different crystal phases and morphologies using different synthesis methods, which are closely related to its applications, are not yet fully understood. Another titania based nanomaterial, $\text{Li}_4\text{Ti}_5\text{O}_{12}$, as a potential anode material for lithium-ion batteries also attracting research attention in recent year because it shows a number of improved characteristics compared with carbon-based anode materials. Therefore, in this thesis, TiO_2 and $\text{Li}_4\text{Ti}_5\text{O}_{12}$ nanomaterials were studied under high pressure using *in situ* Raman spectroscopy and synchrotron X-ray diffraction.

In Chapter 2, four 1D rutile TiO_2 nanomaterials (i.e. nanowires, nanorods, flower-like nanorods and nanotubes) were synthesized by FTO based hydrothermal method were studied under high pressure for the first time. A new morphology of flower-like nanorods was the first time obtained by this method. The phase transition sequence of these four 1D rutile TiO_2 nanomaterials is consistent with previous study: underwent a transition from rutile to baddeleyite phase upon compression and baddeleyite to $\alpha\text{-PbO}_2$ phase upon decompression. However, nanotubes show the highest phase transition pressure of 20.8 GPa which may be due to its high specific surface area. Interestingly, a unique phase transition phenomenon was observed for nanowires as rutile phase maintained in the whole compression and decompression processes which has never been reported on TiO_2 nanomaterials before. Moreover, the study of compressibility of unite cell along a axis and c axis shows that a axis has higher

compressibility than c axis. In addition, a relatively low bulk modulus of TiO_2 nanotubes was found indicating that among these 1D rutile TiO_2 nanomaterials, nanotubes has the highest compressibility. All observed behaviours mentioned above may be attributed to the special 1D morphologies which lead to morphology-tuned high-pressure behaviours.

In Chapter 3, nanoflower-like spheres $\text{Li}_4\text{Ti}_5\text{O}_{12}$ (LTO-1) and nanoparticles $\text{Li}_4\text{Ti}_5\text{O}_{12}$ (LTO-2) synthesized by microwave-assisted hydrothermal methods were investigated under high pressure for the first time. In this study, two LTO samples show some special high-pressure behaviours: (1) no phase transformations were observed up to 27.1 GPa for LTO-1 and 26.3 GPa for LTO-2, indicating high structure stability of these two nanomaterials; (2) LTO-1 shows higher reversibility and crystallinity than LTO-2; (3) LTO-2 (167 GPa) has a much higher bulk modulus than LTO-1 (123 GPa) which indicates a morphology-induced alteration of bulk modulus; (4) Based on previous study of lattice strain has a positive correlation with bulk modulus, we can infer that LTO-2 has a larger intrinsic lattice strain than that of LTO-1, consistent with the observation of the better performance of LTO-1 in LIB operations; (5) Higher compressibility of LTO-1 than LTO-2 was examined in comparison with other nanostructured lithium titanium dioxide suggest higher lattice vacancies and structural stabilities of LTO-1, also consistent with the observation of higher capacity of LTO-1 than LTO-2 in LIB operations. This study shows that multiple factors including the lattice strain, lattice vacancy and surface area must be considered together in the design of new nanostructured electrode materials in the future.

4.2 Future work

By finishing this thesis, we have obtained many structure information of nanostructured TiO_2 and $\text{Li}_4\text{Ti}_5\text{O}_{12}$ under high pressure. However, there are still some work needs to be done in the future.

For Chapter 2, the high-pressure behaviours of anatase nanostructured TiO₂ is well studied under high pressure. Compared with anatase TiO₂, lots work still needs to be done for rutile phase TiO₂. For example, in most cases, the size and morphology effects on high-pressure coexist; which one plays the dominant roles in phase transition is not clear yet. To solve these problems, further studies can focus on the high-pressure studies of 1D TiO₂ nanomaterials with different size and different crystal growth orientation. In addition to pure TiO₂ nanomaterials, investigating some other composite such as doped- TiO₂ nanomaterials are also be of great interest as ion doping is an effective way to improve its applications in energy conversion and storage. The comparison study of the designed TiO₂ and its corresponding pure phase under high pressure is of great interest.¹⁻³ For example, Lu *et al.*⁴ recently reported the Nb-doped anatase TiO₂ nanoparticles under high pressure show a significant enhancement in electron transport properties of the pressure-treated TiO₂ in comparison to the pristine anatase phase.

For Chapter 3, Li₄Ti₅O₁₂ nanomaterials are the first time studied under high pressure. In order to further study the size- and morphology- effect on the high pressure behaviors of Li₄Ti₅O₁₂ nanomaterials, more samples with different morphologies are needed to investigate under high pressure.

4.3 References

- (1) Liu, G.; Yang, H. G.; Wang, X. W.; Cheng, L. N.; Pan, J.; Lu, G. Q.; Cheng, H. *M. J. Am. Chem. Soc.* **2009**, *131*, 12868.
- (2) Lu, X. J.; Mou, X. L.; Wu, J. J.; Zhang, D. W.; Zhang, L. L.; Huang, F. Q.; Xu, F. F.; Huang, S. M. *Adv. Funct. Mater.* **2010**, *20*, 509.
- (3) Das, C.; Roy, P.; Yang, M.; Jha, H.; Schmuki, P. *Nanoscale* **2011**, *3*, 3094.
- (4) Lu, X. J.; Yang, W. G.; Quan, Z. W.; Lin, T. Q.; Bai, L. G.; Wang, L.; Huang, F. Q.; Zhao, Y. S. *J. Am. Chem. Soc.* **2014**, *136*, 419.

Appendix I Data analysis methods

A 1.1 FIT2D*

FIT2D is a one and two dimensional data analysis program which is mostly be used on European Synchrotron Research Facility beam lines and lots of crystallography groups all over the world. FIT2D is widely used for both interactive and “batch” data processing, and is used for various purposes by many user communities. In this thesis, FIT2D is used to process the X-ray diffraction (XRD) data collected by MAR detector.

By using FIT2D, two dimensional XRD data which collected as Debye-Scherrer rings can be integrated into one dimensional profile with 2θ or radial direction. This provides a number of different output configurations. For instance, a number of different 2θ scans, for different azimuth ranges, a one dimensional profile of intensity of a ring as a function of azimuth, or a polar transform of the data can be obtained. Moreover, there are also different options of the output formats, which include GSAS formats, Cerius formats, as well as ASCII format. In the following, the GSAS format will be used in the Rietveld refinement analysis.

* Website: <http://www.esrf.eu/computing/scientific/FIT2D/>

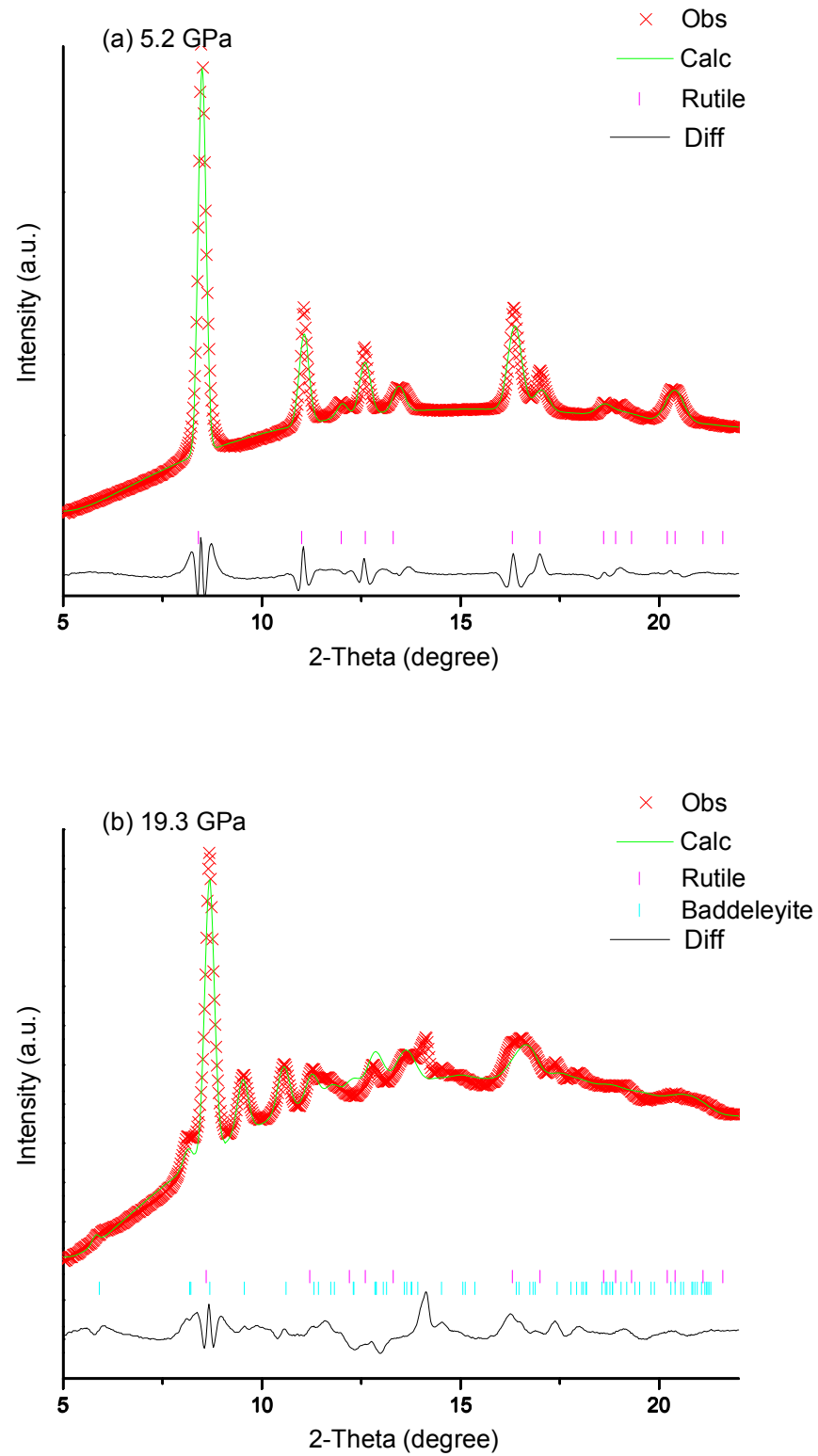
A 1.2 Rietveld refinement method*

Rietveld refinement method is developed by Hugo Rietveld for use in the characterization of crystalline materials. The principle of Rietveld refinement is to refine a calculated line profile by a least squares method and make the calculated line fits the observed profiles. The height, width and position of peaks in neutron or X-ray diffraction can provide us lots of information of the materials' structures, such as the unit cell parameters, positions of atoms, etc.

Many programs can be used to process Rietveld refinement, such as GSAS + EXPGUI, Fullprof and PowderCel, which can be freely downloaded from internet. There are also many commercial programs are available, such as MDI Jade and Bruker TOPAS. In this thesis, the GSAS + EXPGUI program is used to process all the refinements.

* Website: <http://www.ccp14.ac.uk/ccp/web-mirrors/lutterotti/~luttero/laboratoriomateriali/Rietveld.pdf>

Appendix II Selected Rietveld refinements for 1D rutile TiO_2 nanomaterials



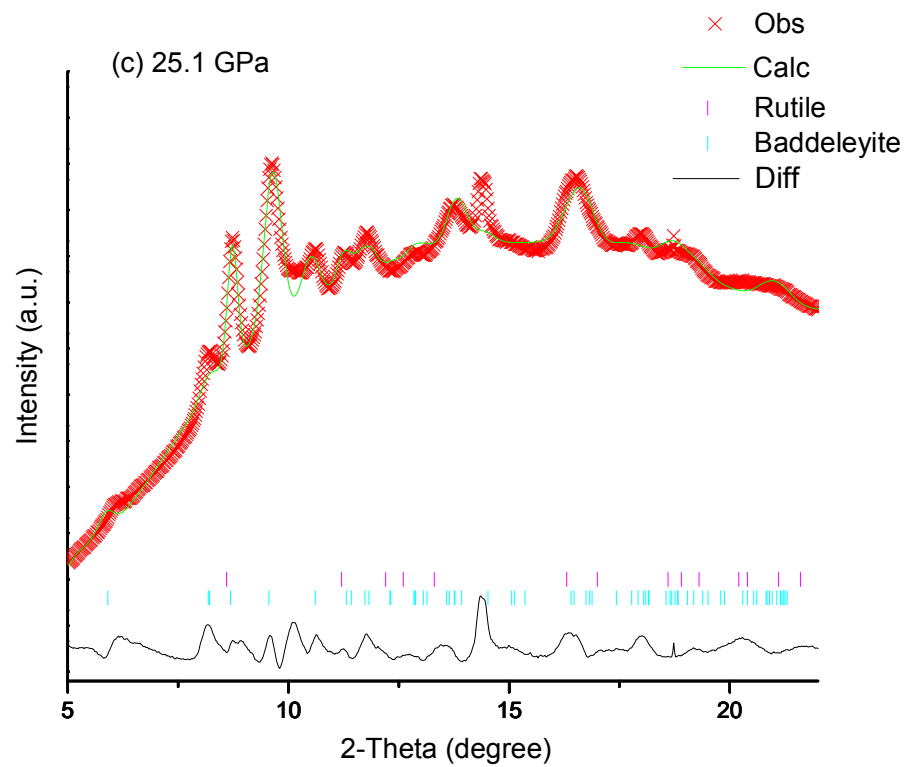
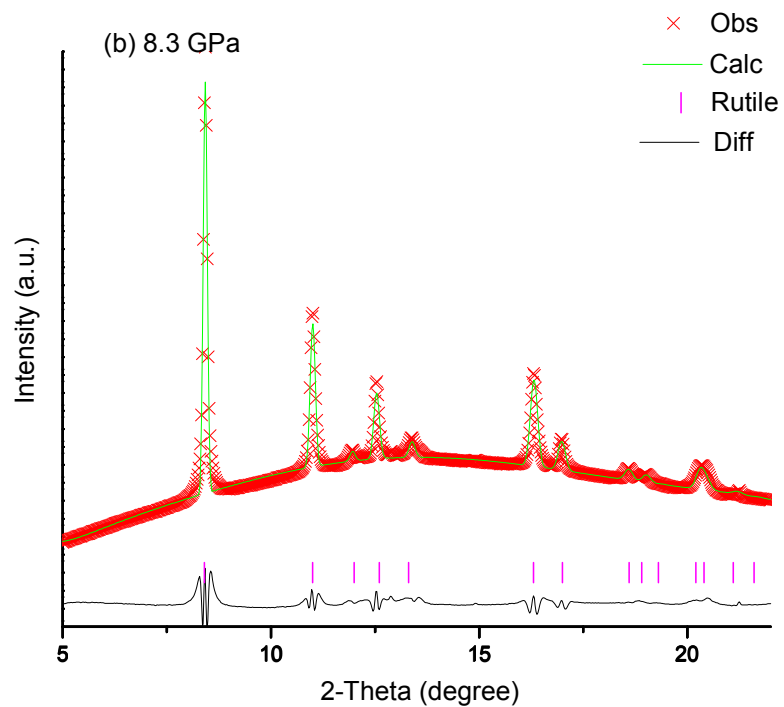
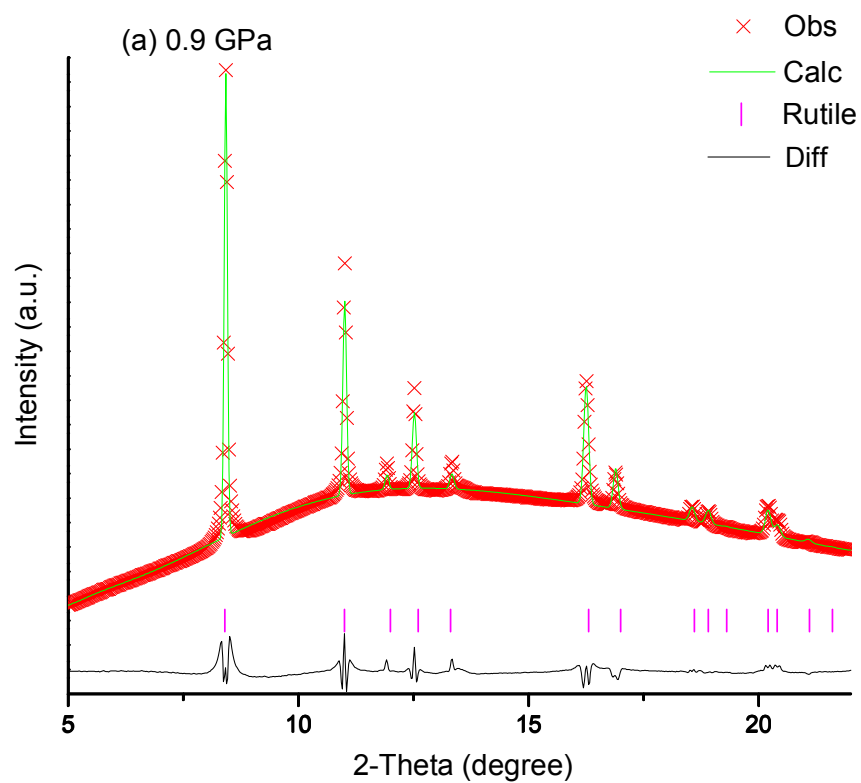
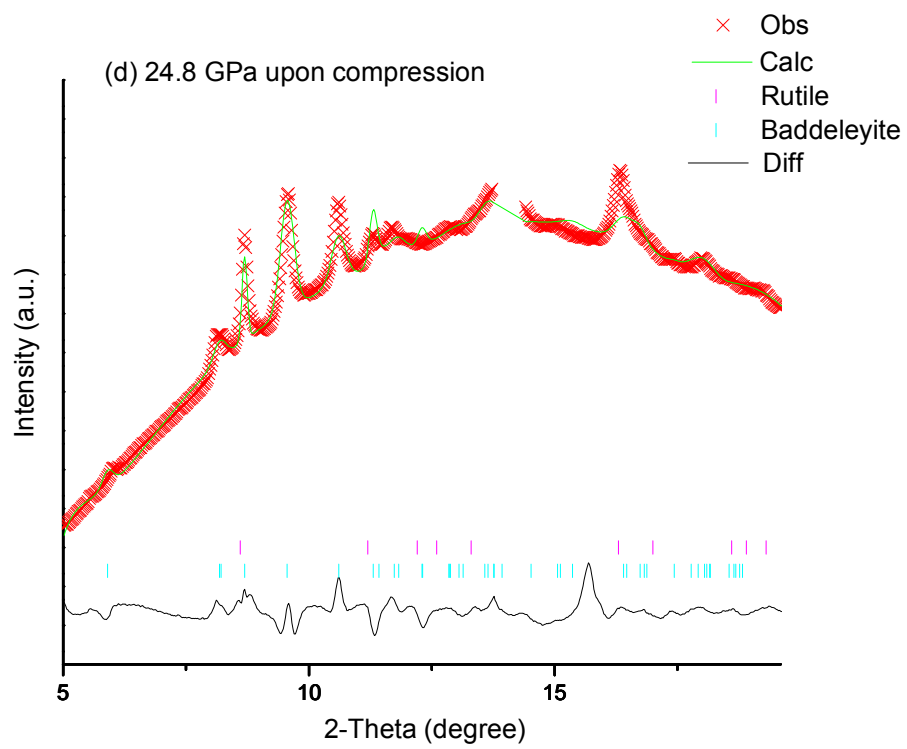
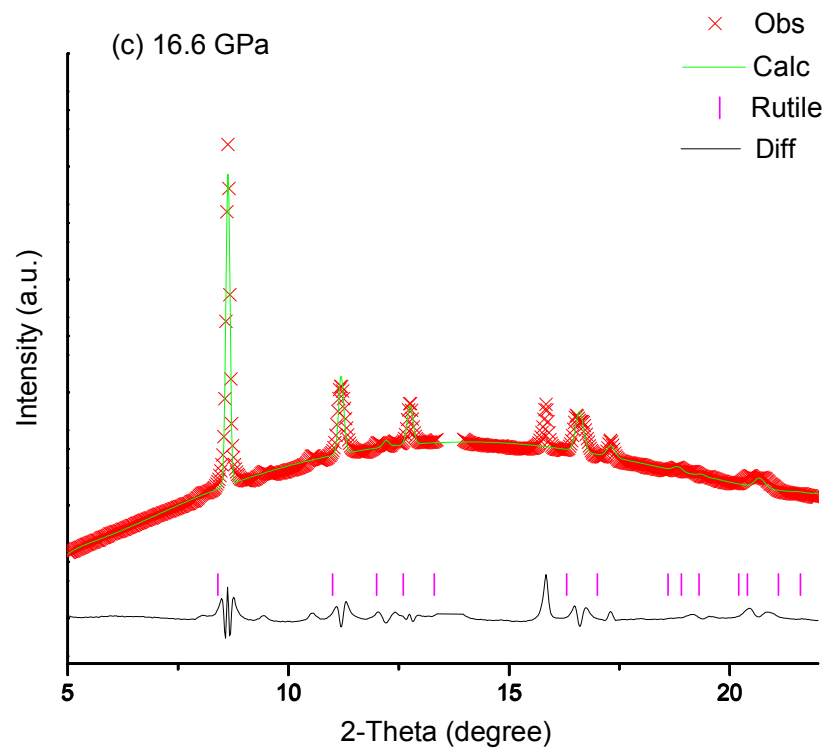


Figure A1 Rietveld refinement of XRD pattern for rutile TiO_2 nanowires at (a) 5.2 GPa, (b) 19.3 GPa and (c) 25.1 GPa upon compression. The red cross is experimental X-ray intensity, whereas the green solid line is the calculated diffraction pattern based on refinement with the black curve at the bottom showing the difference between the calculated and observed intensities. The vertical bars with different colors indicate the characteristic reflections of different phases.

Table A1 Unit cell parameters of three phases for rutile TiO₂ nanowires.

Rutile phase			Baddeleyite phase				α -PbO ₂ phase				
P (GPa)	a = b (Å)	c (Å)	P (GPa)	a (Å)	b (Å)	c (Å)	β (°)	P (GPa)	a (Å)	b (Å)	c (Å)
1.0	4.5894	2.9574	25.1	4.6970	4.8050	4.6721	97.1637	0.7	4.5267	5.5090	4.9726
3.4	4.5760	2.9541	30.6	4.8527	4.5893	4.7142	96.4629				
5.2	4.5527	2.9461	36.3	4.7092	4.5960	4.8549	96.1235				
12.1	4.5187	2.9301									
14.6	4.4978	2.9230									
17.6	4.4731	2.9156									
19.6	4.4551	2.9014									
25.1	4.4299	2.9214									
30.6	4.4149	2.9167									
36.3	4.3820	3.1213									





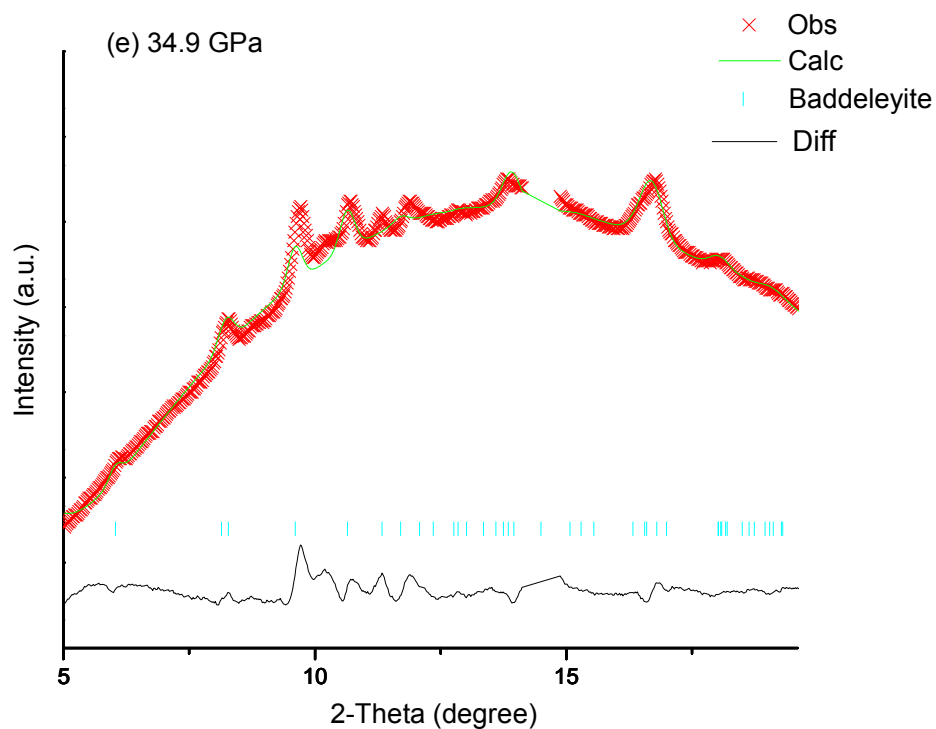
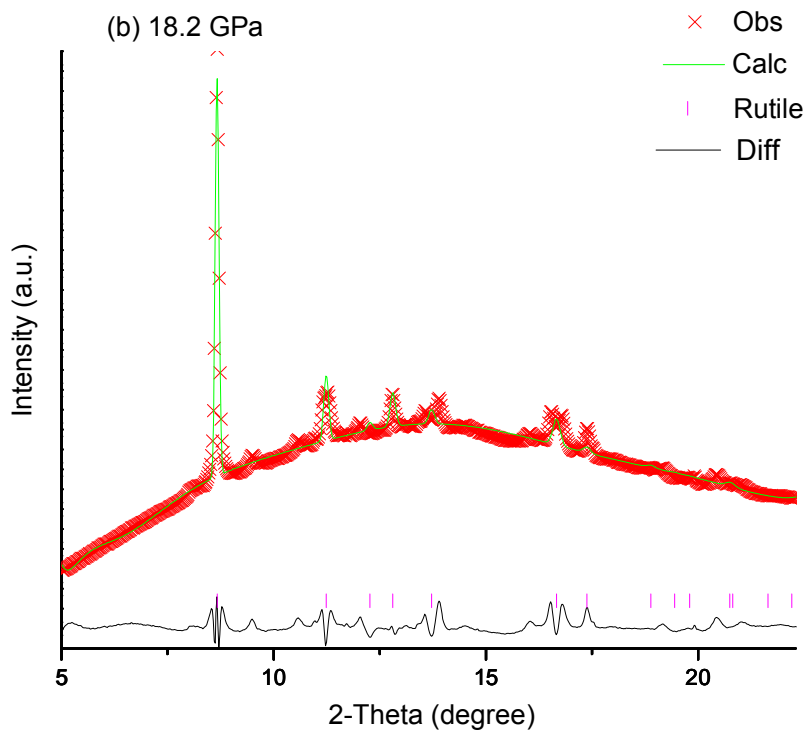
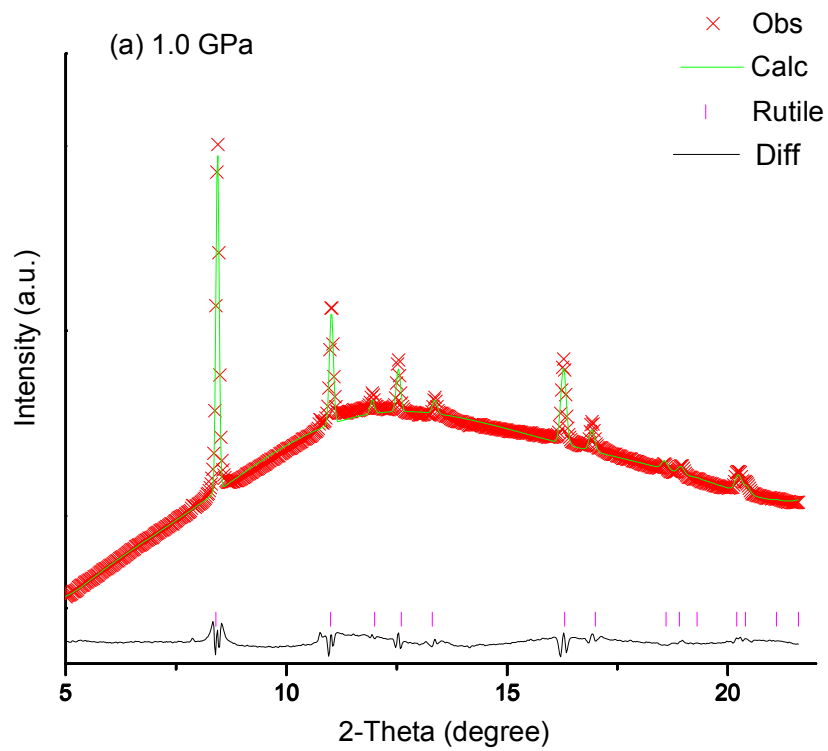
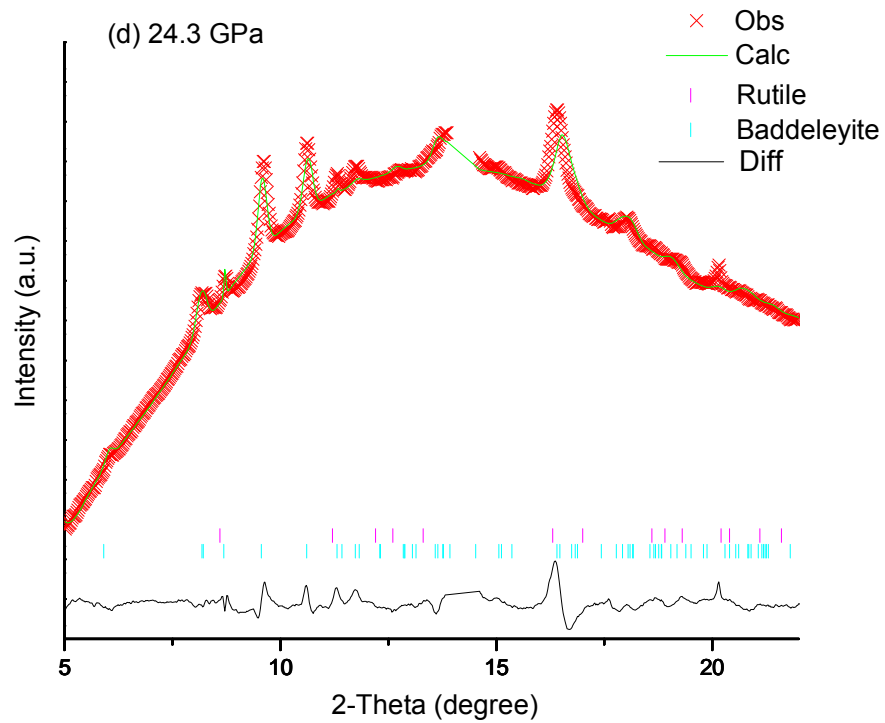
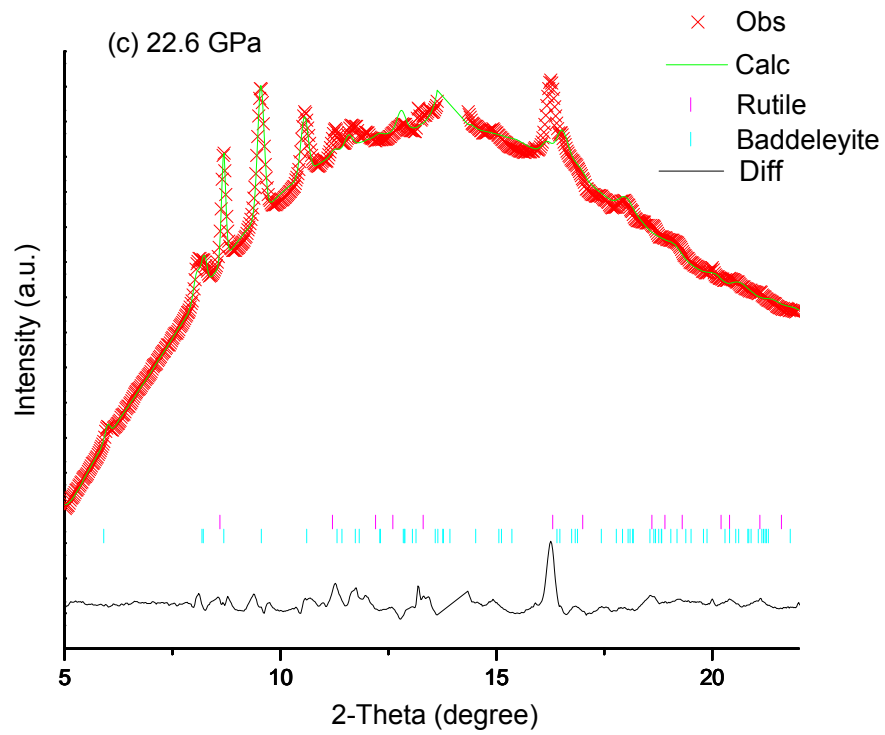


Figure A2 Rietveld refinement of XRD pattern for rutile TiO₂ flower-like nanorods at (a) 0.9 GPa, (b) 8.3 GPa, (c) 16.6 GPa, (d) 24.8 GPa and (e) 34.9 GPa upon compression. See Figure A14 for figure caption.

Table A2 Unit cell parameters of three phases for rutile TiO₂ flower-like nanorods.

Rutile phase			Baddeleyite phase					α -PbO ₂ phase			
P (GPa)	a = b (Å)	c (Å)	P (GPa)	a (Å)	b (Å)	c (Å)	β (°)	P (GPa)	a (Å)	b (Å)	c (Å)
0.9	4.5909	2.9581	18.3	4.4978	4.9274	4.8663	98.4336	0.7	4.5246	5.5038	4.9261
3.1	4.5757	2.9514	20.2	4.5303	4.8841	4.7316	98.6446				
6.2	4.557	2.9417	22.7	4.5304	4.8841	4.7316	98.6446				
8.3	4.54305	2.9378	27.8	4.6651	4.7815	4.6991	98.4874				
10.0	4.5345	2.9381	29.6	4.6109	4.7489	4.7142	98.5169				
14.8	4.5061	2.9287	31.6	4.6109	4.7489	4.7142	98.5169				
16.6	4.4824	2.9158	34.9	4.5817	4.8290	4.7278	98.5295				
18.3	4.4738	2.9153									
20.2	4.4624	2.8997									
22.7	4.4549	2.8583									
27.8	4.4414	2.9792									
29.6	4.4317	2.9844									
31.6	4.4311	2.9805									





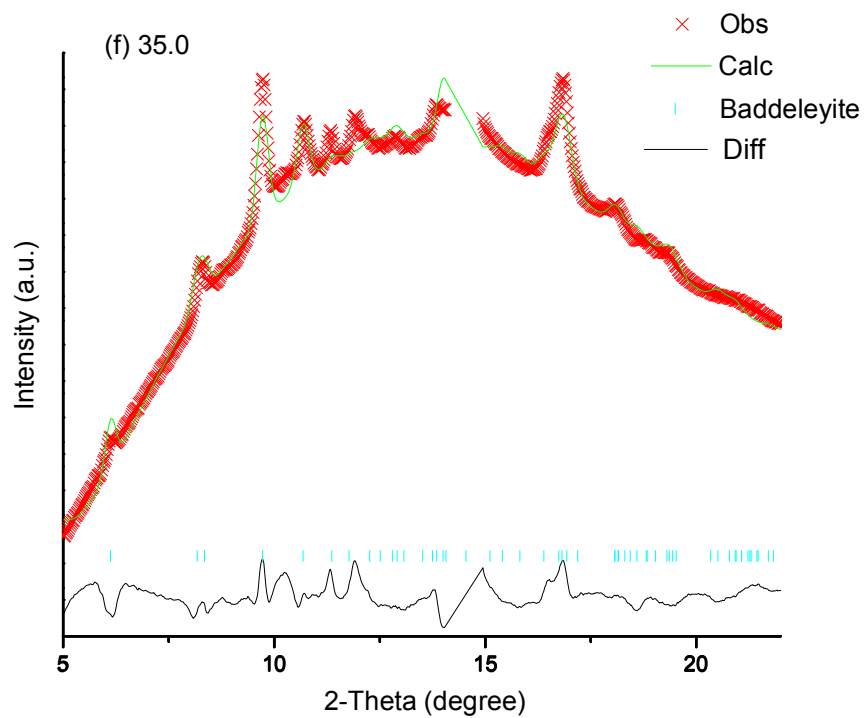
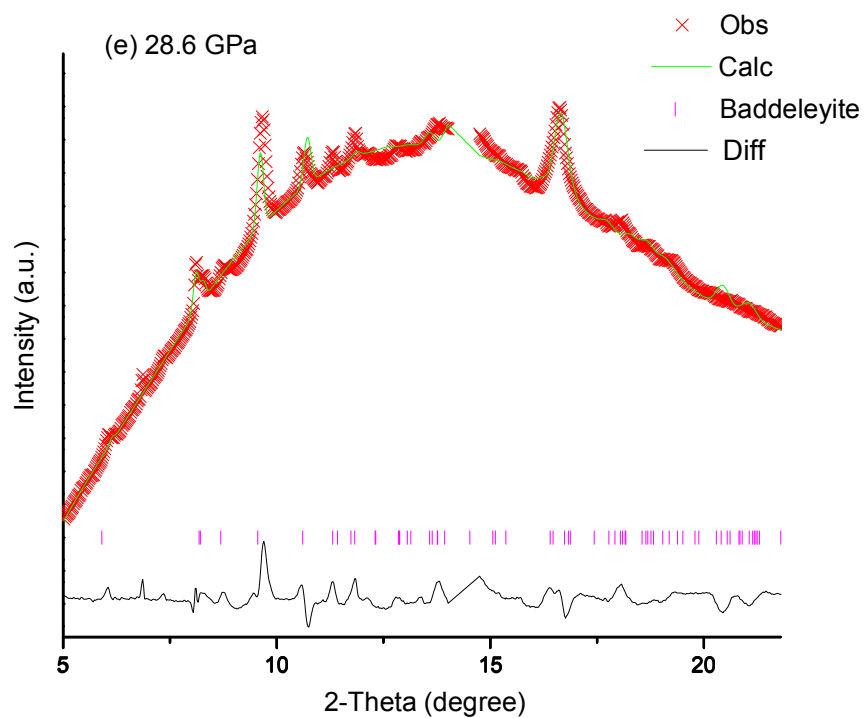


Figure A3 Rietveld refinement of XRD pattern for rutile TiO_2 nanotubes at (a) 1.0 GPa, (b) 18.2 GPa, (c) 22.6 GPa, (d) 24.3 GPa, (e) 28.6 GPa and (f) 35.0 GPa upon compression. See Figure A14 for figure caption.

Table A3 Unit cell parameters of three phases for rutile TiO₂ nanotubes.

Rutile phase			Baddeleyite phase					α -PbO ₂ phase			
P (GPa)	a = b (Å)	c (Å)	P (GPa)	a (Å)	b (Å)	c (Å)	β (°)	P (GPa)	a (Å)	b (Å)	c (Å)
1.0	4.5822	2.9554	20.8	4.5779	4.9099	4.7286	98.6093	0.3	4.5373	5.5043	4.9331
4.7	4.5568	2.9467	22.6	4.5892	4.8566	4.7718	98.3511				
7.5	4.5357	2.9382	24.3	4.5773	4.8931	4.6989	98.5945				
11.1	4.5108	2.9296	28.6	4.5016	4.9437	4.6662	98.7810				
13.2	4.4971	2.9198	35.0	4.5074	4.8175	4.6946	97.7956				
15.2	4.4840	2.9169									
18.2	4.4629	2.9056									
20.8	4.4395	2.8864									
22.6	4.4540	2.9043									
24.3	4.4371	2.8779									

Appendix III Selected Rietveld refinements for nanoparticles

$\text{Li}_4\text{Ti}_5\text{O}_{12}$ (LTO-2)

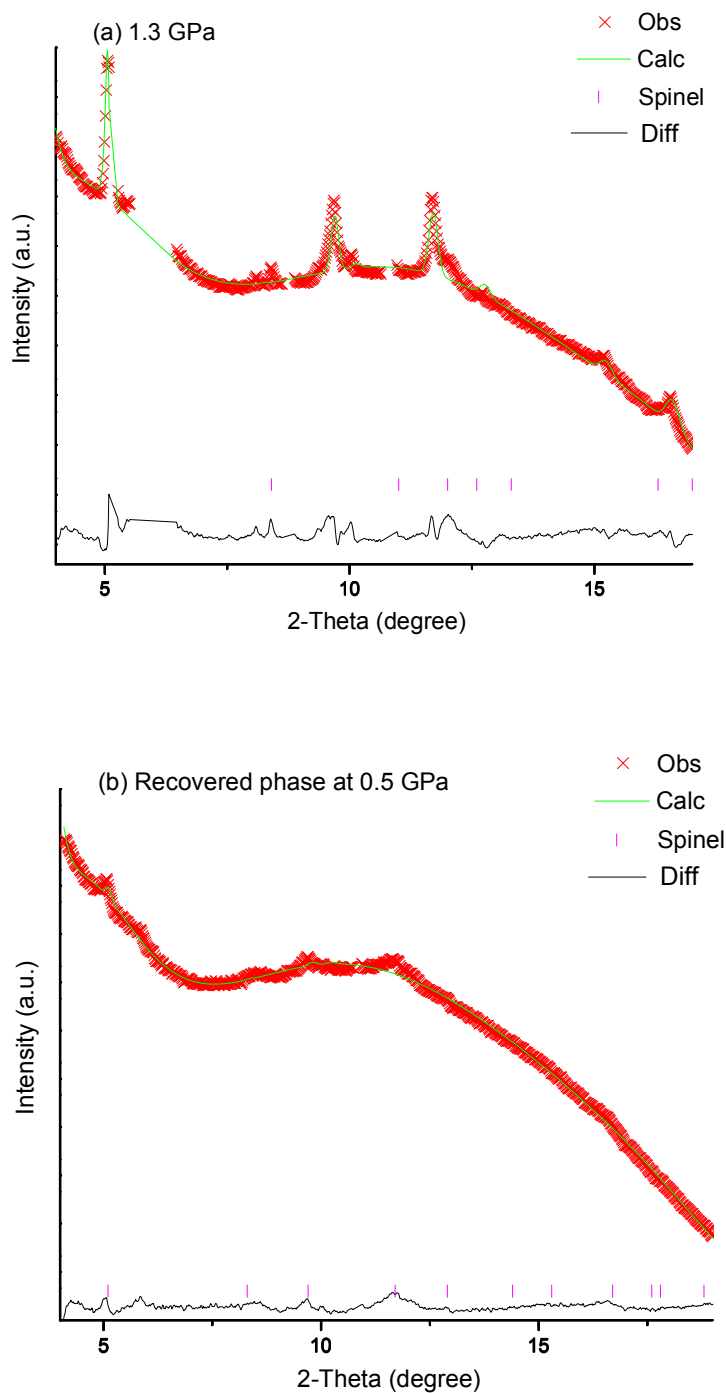


Figure A4 Rietveld refinement of XRD pattern for $\text{Li}_4\text{Ti}_5\text{O}_{12}$ nanoparticles at (a) 1.3 GPa upon compression and (b) recovered phase at 0.5 GPa. See Figure A14 for figure caption.

Curriculum Vitae

Name:	<u>Fengping Xiao</u>
Post-secondary	University of Western Ontario
Education and	London, Ontario, Canada
Degrees:	2013 – 2015 M.Sc.
	East China Institute of Technology
	Nanchang, Jiangxi, P. R. China
	2005 – 2009 B.Sc.
Honors and	National Excellent Student Scholarship
Awards:	Chinese Ministry of Education
	2008– 2009
	Excellent Student Scholarship of Grade 1
	East China Institute of Technology
	2007 – 2008
Conference	Oral presentation
	“High-Pressure Study of 1D Nanostructured Titanium Dioxide by Raman Spectroscopy and Synchrotron X-ray Diffraction.” The 98 th CSC, Ottawa, Ontario, Canada. (06/2015)
Related Work Experience:	Centre Assistant
	Soochow University – Western University Centre for Synchrotron Radiation Research
	2014 – 2015
	Teaching Assistant/Research Assistant
	University of Western Ontario
	2013 – 2015
	Assistant Engineer
	Tianjin North China Geological Exploration Bureau
	Tianjin, China
	2009 – 2012